Turbulent plumes in confined spaces

by

Nitheesh George

Submitted in total fulfilment of the requirements
of the degree of Doctor of Philosophy

December 2020

Department of Mechanical Engineering

THE UNIVERSITY OF MELBOURNE

Declaration of Authorship

This is to certify that:

- the thesis comprises only my original work towards the PhD at the University of Melbourne,
- due acknowledgement has been made in the text to all other material used,
- the thesis is fewer than 100 000 words in length, exclusive of tables, maps, bibliographies and appendices.

Signed: _____

Date: _____

Abstract

Studies pertaining to turbulent plumes in confined spaces are of utmost interest due to its relevance in practical flows that are associated with, but not restricted to, the propagation of smoke and hot gases generated by fires in buildings, road and railway tunnels etc. In this dissertation, direct numerical simulations (DNS) of the governing equations are carried out to analyze such flows with the focus on (i) free turbulent line plumes, and (ii) wall attached turbulent line plumes, in confined spaces. In all cases, the computation domain is rectangular with no-slip and adiabatic boundary conditions at the top, bottom and lateral side walls.

In free turbulent line plume simulations, the plume originates from a line heat source of length, L, located at the centre of the bottom wall and rises until it impinges on the top wall and eventually spreading out laterally there by producing a buoyant fluid layer at the top wall. Since the region is confined, the continuous heat source forces the top layer to move downwards, until it reaches the bottom wall, when the flow is said to be at the asymptotic state (Baines and Turner 1969). DNS data at three Reynolds numbers (Re_H), 1800, 3600 and 7200, based on box height H and the buoyant velocity scale, $F_0^{1/3}$, where F_0 is buoyancy flux per unit length, are presented for plume lengths, $L/H = 1$, 2 and 4 and box aspect ratio, $R/H = 1$. Here, R is the box half-width. Following the initial transient dynamics, a flapping motion of the plume is observed, where the plume oscillates around the centre plane of the box. The DNS results reveal that the long-term behaviour of the flow consists of a meandering, flapping plume with a counter-rotating vortex pair on either sides of the plume. Additionally, the plume volume, momentum, and buoyancy fluxes obtained from the simulations are compared to the theoretical models proposed by Baines and Turner (1969) and Barnett (1991). Further, simulations of turbulent line plumes are carried out at increased box aspect ratios $R/H = 1, 2, 4, 8$ and 16, to study the horizontal outflow of the buoyant fluid layer after the plume impinges on to the top wall. Following the axisymmetric plume model of Kaye and Hunt (2007), a theoretical model to compute the horizontal outflow properties is developed for turbulent line plumes.

In the case of wall attached thermal plumes, the plume originates from a local line heat source placed at the bottom left corner of the box. The plume develops along the vertical side wall while remaining attached to it before spreading across the top

wall forming a buoyant fluid layer and eventually moving downwards and filling the whole box. The simulations are carried out at $Re_H = 14530$ and $L/H = 0.5$, and a parametric study is conducted for boxes of aspect ratios $R/H = 1$ and 2. Furthermore, the original filling box model of Baines and Turner Baines and Turner (1969) is modified to incorporate the wall shear stress and are compared against the results obtained from the DNS. A reasonable agreement is observed for the volume and momentum fluxes in the quiescent uniform environment and for the time-dependent buoyancy profiles calculated further away from the plume.

Finally, the entrainment processes in both free and wall attached line plumes are assessed, using the DNS data. Both cases show similar contributions to entrainment due to net buoyancy. However, a deficit in the entrainment coefficient is observed for wall plumes due to the effect of the wall, which in turn suppressed the turbulent kinetic energy production.

Acknowledgements

I would like to extend my sincere gratitude to my supervisors, Prof. Andrew Ooi, Dr. Jimmy Philip and A/Prof. Daniel Chung, whose support and guidance have been invaluable. I am very fortunate to have had the opportunity to work both for and with them. I would also like to thank my committee chair Prof. Ivan Marusic for his valuable remarks and suggestions during my progress review meetings.

I would also like to thank my friends and colleagues in the fluid mechanics group. Special thanks to Dr. Chong Shen, Dr. Dileep Chandran, and Vijay Gudla for the countless informative discussions and their willingness to share their expertise.

Finally, I would like to thank my family for their support, encouragement, and understanding.

Contents

List of Figures

List of Tables

Chapter 1

Introduction

The buoyant turbulent plumes in a confined region are common industrial and geophysical flows, for example, smoke from a fire in a building or a tunnel, disposal of waste and toxic matters into lakes and oceans. This research presents the study of three types of confined turbulent plumes originating from a localised line heat source shown in figure 1.1. The first problem dealt with in this thesis is the

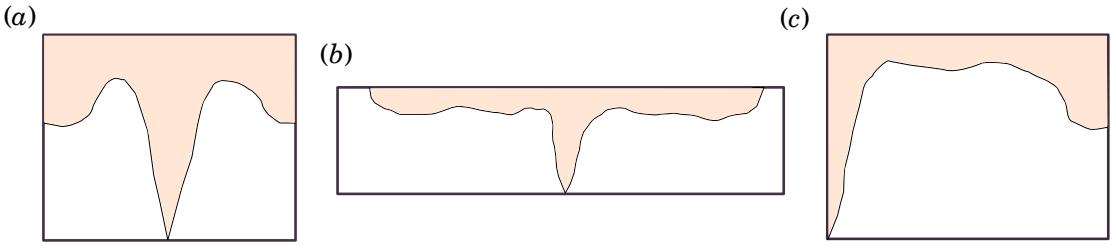

FIGURE 1.1: Schematic diagram of the three different types of confined plumes investigated in this thesis: (a) confined free plumes (the filling-box problem), (b) outflow from a turbulent plume impinging on a horizontal ceiling, and (c) wall attached plumes.

confined free line plumes (commonly known as filling-box problem, figure 1.1 a), within which the transient and asymptotic behaviours of plumes are studied, and the relevant parameters are compared with mathematical models. Then, attention is focused on outflow from a line plume impinging on a horizontal adiabatic and impermeable surfaces (figure 1.1 b). Different aspect ratio (box half-width/height) boxes are considered to analyse buoyant currents from impinging plume. Finally, the buoyant line plumes are placed near the side wall of the box (figure 1.1 c) and the effect of wall on confined wall attached plumes are studied.

1.1 Motivation

Fire safety engineers are interested in the phenomena of the propagation of smoke and hot gases generated by fires in buildings, road and railway tunnels. Understanding these situations would allow them to identify the time required to evacuate a building or a tunnel before concentrations of either the smoke from a fire or the released chemical become hazardous. These types of fire situations in confined spaces are studied in this thesis using direct numerical simulations (DNS) of the governing equations.

Baines and Turner (1969)'s filling-box model serves as the starting point in the study of confined plumes. The filling-box model represents an idealised model of fire in enclosed rooms and can help fire-fighters to take decisions faster and more accurately. This thesis starts with the aim of testing the validity of the filling-box (and related) model for *confined line plumes*, which have received less attention in the literature. Also, the behaviours of confined fires in the early and later stages are investigated, which will eventually support the evacuation planning and the control of fire spreading.

Another type of confined buoyant flow considered here is the outflow from a line plume impinging on the top wall, which also has applications related to tunnel fires. The physics behind the horizontal outflow propagation in both uniform and stratified environments are not fully understood due to the lack of detailed experimental and computational study. The present DNS database is aimed at assessing existing models and developing new ones.

Finally, the attention is focused on the confined wall attached thermal line plume. This type of configuration is a rarity in the literature. Therefore, there are many potential questions regarding the effect of the wall on the entrainment and filling process.

1.2 Objectives

The main objectives of this thesis are the following:

- Conduct direct numerical simulations of confined free and wall attached plumes from a line source,

- Describe the filling-box mechanisms for line plumes.
- Compute the entrainment coefficients in both free and wall attached line plumes, and compare with the help of theoretical models.
- Test the Baines and Turner (1969)'s model for line plumes in both transient and asymptotic stages,
- Extend the Kaye and Hunt (2007)'s model for the bulk properties of the horizontal outflow from a point plume to a line plume.
- Measure the horizontal front propagation in both uniform and stratified environments for different aspect ratio boxes and study using scaling laws.
- Develop a mathematical model for the filling processes of the wall attached line plumes in confined spaces by considering wall effects and validate using DNS results.

1.3 Outline of thesis

This Thesis is organised as follows: Chapter 2 provides a review of the previous experimental and numerical studies for different plume configurations considered in the present study. Chapter 3 investigates the confined plumes originate from a line heat source, located at the centre of the bottom wall. Then, this case is extended in chapter 4 to analyse the horizontal outflow from the impingement plumes for large aspect ratio boxes. Chapter 5 considers the stratification that develops from a wall attached thermal line plume. Chapter 6 investigates the entrainment process in both free and wall attached plumes. Finally, general conclusions from the present work are presented in chapter 7.

Chapter 2

Literature review

Plumes are a common phenomenon in environmental flows, which occurs due to a density difference between source fluid and the environment under the influence of gravity. For example, include small-scale flows like the smoke rising from a cigarette or smoke from chimneys to volcanic eruption (see figure 2.1).

FIGURE 2.1: Examples of turbulent buoyant plumes in nature.

Most of the real-world plumes are turbulent. Therefore, as opposed to laminar plumes, in this chapter, we mainly focus on turbulent plumes.

Turbulent plume behaviour varies depending on their source conditions. The flux balance parameter Ri, a local Richardson number at the source describes the behaviour of a turbulent plume. The Richardson number Ri classifies plumes in natural buoyancy-driven convection and forced momentum-driven convection (Hunt and Van den Bremer 2011):

$$Ri = \frac{B\,b}{w^2}, \tag{2.1}$$

where B denotes the buoyancy of the plume, b is a characteristic width of the plume and w is the characteristic vertical velocity.

The limit $Ri \to 0$ is refer to as a jet that is dominated by its source momentum flux, whereas a plume that is generated by a pure natural convection corresponds to the limit $Ri \to \infty$. Every buoyant plume, independent of starting Ri, with increasing height will eventually reach a constant Ri called the plume Richardson number, Ri_p. Plumes are classified into 'forced', 'pure' and 'lazy' depending on the source $Ri < Ri_p$, $= Ri_p$ or $> Ri_p$.

2.1 Plumes in unconfined environment

The primary quantities of interest for plumes in an unconfined environment are the distributions of velocity and temperature. The case of fully developed unconfined buoyant plumes is well documented in the literature for both a plume originating from a point source and a plane plume generated by a line source.

The first quantitative study of plumes in an open environment was conducted by Schmidt (1941), and he observed that the plume of hot air rising from small sources into a quiescent uniform environment occupies a conical region when the flow is turbulent. Schmidt used mixing-length-type hypotheses to obtain an expression for the mean velocity and temperature profiles for both round and plane plumes, and validated these with the use of small-scale experiments. Later, Rouse et al. (1952) conducted measurements in a room by using a gas burner as a heat source and found that the distribution of mean temperature and vertical velocity in a horizontal plane can be fitted by the Gaussian curves for both round and line plumes.

The work of Morton et al. (1956) on fundamental characteristics of plumes is generally known as classical plume theory. Morton et al. (hereafter referred to as MTT) developed a relatively simple analytical model for Boussinesq plumes in a uniform environment based on two important assumptions. The first assumption is the mean entrainment velocity u_e (the radial or transverse velocity at the edge of the plume) at a particular height from the source is directly proportional to the mean vertical velocity $\overline{w}$ at the same height, i.e. $u_e = \alpha\,\overline{w}$, where α is the entrainment coefficient for the plume. The second assumption is that the horizontal variations of mean buoyancy and vertical velocity profiles are self-similar

with height. MTT model describes the vertical variations in volume, momentum and buoyancy flux for a plume above a point source of buoyancy. From these bulk quantities, it is possible to derive expressions for the plume radius, vertical velocity and buoyancy as a function of height above the plume source.

Morton (1959) also classified plumes into three different categories by introducing a flux balance parameter Γ, which is proportional to the local Richardson number. The definition of Γ for a plume that arises from a point source with Gaussian assumptions for mean vertical velocity and buoyancy is

$$\Gamma = \frac{5\,F\,Q^2}{8\alpha\sqrt{\pi}M^{5/2}} = \frac{Ri}{Ri_p}, \tag{2.2}$$

where F, Q and M are the plume buoyancy flux, volume flux and momentum flux, respectively. Based on the source value of Γ, the plumes are classified as pure ($\Gamma = 1$), forced ($0 < \Gamma < 1$) and lazy ($\Gamma > 1$). However, as mentioned above for all lazy and forced plumes, the plume source parameter Γ approaches 1 in the far field (Morton and Middleton 1973), i.e. for all lazy and forced plumes take on pure plume behaviour at some distance from the source.

In the turbulent plume literature, some researchers (e.g.Plourde et al. 2008, Pham et al. 2007 and Elicer-Cortés 1998) use the term 'pure thermal plume' to refer a plume driven only by buoyancy source. Although, in that case, the limit of Γ at the source goes to $\Gamma_0 \to \infty$ and from the above mentioned terminology such plumes are classified as extremely lazy. In the following paragraphs we shall consider the literatures about purely convective plume, $\Gamma_0 = \infty$, which is more relevant to the present study.

The study of turbulent thermal plumes is essential to understand the convective behaviour of fluids and has lots of application in fire modelling, e.g. prediction of fire spread rates, smoke plume dynamics, etc. Elicer-Cortés (1998) experimentally analysed the temperature field of an axisymmetric thermal pure plume rising from a heated disk. Elicer-Cortés (1998) observed that the mean centreline temperature follows the $z^{-5/3}$ law only in the region $z/D > 2.15$, where the temperature filed achieved a state of self-similarity. Also, he found that the self-similar solution for half-width of temperature matched well with the experimental results, and the plume spread rate was $\mathrm{d}b_T/\mathrm{d}z = 0.096$. However, he did not measure any velocity field.

Pham et al. (2007) conducted direct numerical simulation (DNS) and large-eddy simulations (LES) with the dynamic Smagorinsky eddy-viscosity model of lazy thermal plume from an axisymmetric source and reported on the puffing phenomenon that occurs in the near-field region of the plume source. Plourde et al. (2008) investigated the influence of vortical structures of axisymmetric rapidly expanding thermal plume on the entrainment of ambient fluid using DNS. Plourde et al. (2008) observed three-dimensional hairpin-like vortex structures in the fully turbulent region of the plume. They mentioned two phases of local entrainment processes, namely, the contraction and expulsion phases and argued that these instantaneous mechanisms drive the entrainment process of the thermal plume. Devenish et al. (2010) studied buoyant radial thermal plumes in uniform and stably stratified environments with the help of large-eddy simulation (LES). They made some interesting observations at larger heights. In their study, they showed that the plume vertical velocity is $w \sim z^{-1/3}$ in the far field and the buoyancy follows $B \sim z^{-5/3}$, which is same as the power law relations of MTT. Apart from this, Devenish et al. (2010) showed that horizontal profiles of mean buoyancy and vertical velocity are approximately Gaussian variation, self-similar in the far field and have no significant difference in radial rate of spread for velocity and buoyancy. They estimated an entrainment coefficient of $\alpha = 0.15$ in the uniform environment. Recently, Marjanovic et al. (2017) investigated the near-field behaviours of axisymmetric lazy plumes in a uniform environment with increasing values of source plume parameters, Γ_0, up to $\Gamma_0 = \infty$. Marjanovic et al. (2017) observed that, in the near-field region, vortex rings are formed due to the effect of non-turbulent stress and mixing promoted by large-scale engulfing ambient fluid, that leads to faster decay of plumes. They also showed that the lazy plumes all converge on a far-field value of $\Gamma = 1$, which is the pure plume behaviour.

The studies mentioned above are mainly focused on axisymmetric plumes. Turbulent plumes arising from line sources (planar plumes) have received significantly less attention. It is difficult to achieve a uniform source condition along the length of the source in the laboratory. Only a few experimental and computational studies are available for turbulent plumes from line sources. One of the earliest works on line plumes was done by Lee and Emmons (1961). They measured temperature profiles above a line gas burner and estimated the entrainment coefficient $\alpha = 0.16$ by adopting the entrainment model proposed by MTT. The line plume velocities were not measured, but they calculated the growth of vertical velocity from the temperature measurement alone.

Later, Kotsovinos (1975) conducted a set of experiments to study the entrainment and mixing process in a planar turbulent buoyant plume. Kotsovinos (1975) found that the spreading rate of the mean velocity and temperature profiles are independent of initial Richardson number. They measured the value of entrainment coefficient $\alpha = 0.2$ in the self-similar region.

Kotsovinos and List (1977) observed turbulence in plane turbulent buoyant jets using laser Doppler velocimetry combined with tracer concentration measurements based on microbead thermistor measurement of temperature fluctuations in jets and plumes. He found mean turbulent fluxes as high as 10% of the mean advective flux in jets and as high as 40% in plane plumes.

Chu (1994) studied the turbulent entrainment in jets and plumes using Lagrangian reference frame. Chu correlated the spreading characteristics of jets and plumes with the length and velocity scales of the dominant eddies. In the Lagrangian reference frame, turbulent flows with dominant eddies of similar geometric structure are observed to spread with nearly identical rate.

Ramaprian and Chandrasekhara (1989) carried out experiments to measure mean-flow and turbulence quantities of two-dimensional turbulent line plumes in ambient environments. Ramaprian and Chandrasekhara found that buoyancy causes a significant increase in turbulent intensities and turbulent fluxes and transport coefficients. Their turbulence measurements indicated that the eddy viscosity and turbulence are significantly higher in the plume compared to an isothermal jet.

Lee and Chu (2003) developed a Lagrangian approach for the prediction of free jets and plumes, including effects of crossflow and ambient density stratification. They developed integral equations from the Reynolds equations and the continuity equation and shows good correlation of the different scales along with some details of turbulence properties from experiments.

In all these studies, the value of source plume parameter is $\Gamma_0 = \infty$ i.e. plume are driven only due to a pure buoyancy source, whereas Paillat and Kaminski (2014a) conducted some experiments on plane turbulent salt water plumes with a range of Γ_0, from 0.04 to 0.49. Paillat and Kaminski (2014a) developed a theoretical model for the entrainment coefficient by including the local Richardson number. They reported the value of the entrainment coefficient for Gaussian profiles $\alpha = 0.071$, which is much less than reported entrainment coefficients for fire plumes ($\Gamma_0 = \infty$) from line sources.

2.2 Plumes in confined environment

A turbulent plume arising from a local source of buoyancy in a confined region can lead to stratification of the fluid surrounding the plume, which is described in detail in the so-called filling box problem of Baines and Turner (1969).

The evolution of a plume in a confined region can be divided into two states: the first consists of the initial behaviour of the plume called the transient state. When the plume rises and impinges on the top wall, an interface layer is formed; this layer turns over and moves towards the bottom wall as time increases. The plume below the interface layer is still considered to be a plume in a uniform environment.

Once the interface layer reaches the bottom wall, the flow is considered to be in the asymptotic state. The second asymptotic state is defined by a balance between the mean temperature and mean pressure gradient. In the asymptotic state, all components of velocities are statistically stationary in time at every point in the filling box. Note that, over time, the temperature and pressure increase due to the source of buoyancy in the confined region.

The filling box problem is a relevant model of many industrial and geophysical fluid flows, for example, building ventilation (e.g. Linden et al. 1990 and Hunt et al. 2001), compartment fires (e.g. Zukoski 1986) and in the oceans (e.g. Killworth and Turner 1982).

Baines and Turner (1969) developed a mathematical model for the filling box problem based on the classical plume theory presented by MTT. More details of the filling box model can be found in section 4.3.1. The model describes the vertical position of the first horizontal front (cf. figure 4.10) of buoyant fluid from a localised source. They also developed solutions for the plume centreline vertical velocity, centreline buoyancy and plume half-width as a function of box height in the asymptotic state. The region far away from the plume is called the environment. Their model also predicts the environmental velocity and buoyancy variation with respect to height in the asymptotic state. Baines and Turner (1969) conducted some dye visualisation experiments to verify the solutions for the propagation of buoyant fluid and asymptotic buoyancy variation in the environment from a point source of buoyancy. The limited experimental results matched the model well, and obtained an entrainment coefficient $\alpha = 0.1$ for axisymmetric plumes. In experiments, they produced round plumes by discharging salt water

into a large reservoir of fresh water. However, Baines and Turner (1969) did not measure velocity or density within the plume or outside.

Manins (1979) extending Baines and Turner (1969) study, considered a conducting boundary at the source level in the model, while all other boundaries are considered to be insulating. Manins (1979) experimentally showed that when the aspect ratio $R/H \approx 1$ (R is the half box width and H is the height of the rectangular box) velocities in the ambient and the horizontal and vertical accelerations of the fluid are of similar order of magnitude and overturning occurs. From his experiments Manins found that the outflow occupies approximately 25% of the box height.

Subsequently Worster and Huppert (1983) extended this model and obtained an analytical expression for the time-dependent density profiles in the filling box problem.

Zukoski (1978) developed an analytical model based on mass and energy balances on upper and lower layers of smoke layer to determine the smoke propagation time for a room from a fire. Zukoski assumed that the room is closed, but considered small opening at either the floor or ceiling level. The propagation of smoke layer is calculated by measuring the time at which the temperature at a particular height starts to increase above ambient level.

The effect of aspect ratio (i.e. ratio of the radius of a circle to the height of the tank, R/H) on the filling box process for round plumes was investigated by Barnett (1991) both analytically and experimentally. Barnett (1991) found that the filling box process occurs only for large aspect ratios ($R/H \geq 1.0$). For moderate aspect ratios ($0.172 < R/H < 1.0$), the plume outflow in the environment is observed as horizontally inhomogeneous and overturning circulation is developed in the environment. In the case of extremely small aspect ratios ($R/H \leq 0.172$), the turbulent plume breaks down due to the interaction with the side walls and the plume no longer reaches the top of the tank.

Kaye and Hunt (2007) theoretically and experimentally investigated the horizontal outflow and the overturning effect of a turbulent round plume in a cylindrical filling box for different aspect ratios using saline plume. All their studies are limited to the transient regime. The theoretical model was divided into three different regions, the plume flow, the outflow due to impingement on the box bottom boundary and the flow rising from the side wall. Kaye and Hunt (2007) developed a model for the bulk properties of the horizontal outflow from a point

source. They also conducted dye visualisation experiments using a saline plume to verify the theoretical model.

Recently, Akhter and Kaye (2020) experimentally studied the front movements in the filling box driven by line plumes. Their front movement results indicate that the value of entrainment coefficient for an unconfined plume is 0.16 could be used to predict the front movement for both the centrally located plume and the wall-attached plume.

While all the above studies focus on the plumes generated from a point source in a confined box in the transient regime, investigation of plumes from a line source of buoyancy in the transient and the asymptotic regime has received less attention in the literature. Although important from a practical point of view, we have very limited knowledge about the confined line plumes. There has been no detailed study of range of validity of Baines and Turner (1969)'s model for fire plumes. Most of the previous studies have been carried out on salt water plume experiments. Previous confined plume studies, both point and line source have relied mostly on flow visualisation and employ single point measurements to ascertain the validity of their theoretical models. Detailed velocity and buoyancy measurements have not been carried out. This also precludes a more detailed comparison with models. Furthermore, over the past two decades direct numerical simulations (DNS) have became more affordable, and we have reached a point in time that we can resolve all the scales of the motion at reasonably high Reynolds number. This will allow us to observe limitations of the existing models, if any, and propose improved models.

2.3 Wall plumes

Fire safety engineers are interested in smoke produced by fire near the side walls of a room because of its great practical applications. The effect of walls on the amount of smoke generated by fires is determined by the amount of ambient air entrainment into their plumes, which is different to a free plume. There have been lots of studies regarding free plumes, and though wall plumes are similar to free plumes, and only limited studies have been carried out in this area.

Grella and Faeth (1975) carried out a similarity analysis on turbulent plumes originated from a line heat source at the base of a vertical adiabatic wall with

an assumption of constant skin friction coefficient C_f. Later, Liburdy and Faeth (1978) investigated on weakly buoyant thermal plumes along a vertical isothermal wall. Liburdy and Faeth (1978) experimentally measured the mean plume vertical velocity, temperature and the heat flux to the wall for various plume strength and distances above the source. They observed that isothermal wall plumes have higher velocities and temperature than a free line plumes at same source conditions.

Killworth and Manins (1980) developed a similarity description of horizontal convection driven by a quadratic temperature variation along the horizontal boundary at which the forcing is applied. However, instead of explicitly representing the plume, they extend the result of Manins (1979) and assume that a non-uniform buoyancy distribution on the lower boundary to supply the turbulent plume in the confined region .

Jaluria (1982) analytically studied the mixed convection flow that arises due to a finite heated element located on a vertical adiabatic surface. The study numerically determined the temperature and velocity fields that arises over a wide range of the mixed convection parameter.

Lai et al. (1986) studied the weakly buoyant turbulent wall plumes for vertical and inclined surfaces. Mean and fluctuating concentrations and streamwise velocities were measured at several stations along the wall. Gas mixtures leaving a slot provided well-defined source dimensions and buoyancy fluxes. The observations were used to evaluate predictions based on simplified mixing length and higher-order turbulence models, finding good predictions for mean properties but relatively poor predictions for turbulence properties. These measurements were limited to near-source conditions in order to highlight effects of flow development; therefore self-preserving behaviour was not achieved.

Bonnebaigt et al. (2018) experimentally studied the turbulent plume from a buoyancy source that is vertically distributed over the full area of a wall. They developed a peeling plume model, where density and vertical velocity vary linearly across the width of the plume, so that plume fluid peels off into the ambient at intermediate heights, more accurately captures the shape of the ambient buoyancy profiles measured in experiments

Recently, Parker et al. (2020) conducted a set of measurements on turbulent free and wall plumes. They found that the value of entrainment coefficient in the wall plume is slightly more than half that of the free plume. The reduction in

entrainment was investigated by considering a decomposition of the entrainment coefficient.

While all the above studies focus on the plumes generated at the side wall in an open environment, investigation of plumes attached to the wall in a confined environment has received less or almost no attention in the literature.

Chapter 3

Details of the direct numerical simulations

The details of the numerical methods used for the direct numerical simulations for all chapters of this thesis are provided in this chapter. This code is a variant of in-house written code in C and parallelised using MPI, and has been used in past studies, for example, Matheou and Chung (2012) and Ng et al. (2015).

The present code numerically solves the equations of mass, momentum and energy conservation under the Boussinesq approximation for an incompressible viscous flow. The resulting governing equations are:

$$\frac{\partial u_i}{\partial x_i} = 0, \tag{3.1}$$

$$\frac{\partial u_i}{\partial t} + u_j \frac{\partial u_i}{\partial x_j} = -\frac{1}{\rho}\frac{\partial p}{\partial x_i} + \nu \frac{\partial^2 u_i}{\partial x_j^2} + g\beta T\, \delta_{i3}, \tag{3.2}$$

$$\frac{\partial T}{\partial t} + u_j \frac{\partial T}{\partial x_j} = \kappa \frac{\partial^2 T}{\partial x_j^2}, \tag{3.3}$$

where ν is the kinematic viscosity, g is the gravitational acceleration, β is the coefficient of thermal expansion and κ is the thermal diffusivity. Velocity components are denoted by u_i, ρ is a constant reference density, and T is the temperature. Note that, for convenience we will also use the notation convention $(u_1, u_2, u_3) = (u, v, w)$.

In this code, the fourth-order staggered-grid finite difference scheme of Morinishi et al. (1998) is used for spatial discretisation of Navier Stokes equations in x and z

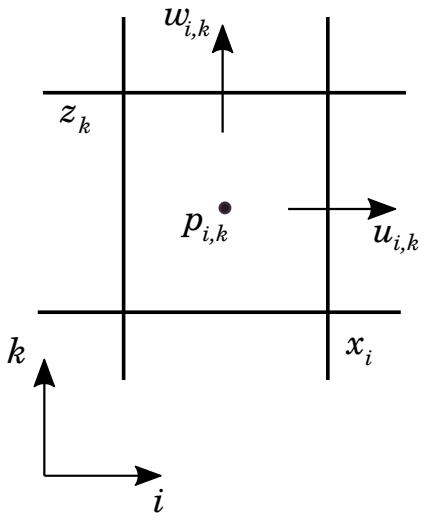

FIGURE 3.1: Two-dimensional representation of staggered grid used in the code.

directions. All three velocity components are stored at the cell faces , whereas the scalar variables such as pressure and temperature are stored in the cell centres of the control volume (figure 3.1). The approach has advantage of avoiding oscillatory pressure field.

The present implementation uses the fourth-order skew-symmetric finite difference discretisation of Verstappen and Veldman (2003) for the interior points, where is it shown to be stable, and to conserve mass, momentum and energy for the interior volumes (note that in the presence of the boundaries, the discretisation requires the boundary conditions of Sanderse et al. (2014) to ensure energy conservation). The present discretisation scheme is equivalent to that of Morinishi et al. (1998) on uniform grids, however on non-uniform grids, strict energy conservation was sacrificed by Morinishi et al. (1998) to maintain fourth-order accuracy by using mesh-dependent interpolation and differentiation. Furthermore, their boundary scheme maintained the mass and momentum conservation of the interior discretisation. Using the notation of Verstappen and Veldman (2003), the semi-discrete Navier-Stokes equations (3.1) and (3.2) appear as:

$$\boldsymbol{\Omega}\frac{\mathrm{d}\boldsymbol{u}_h}{\mathrm{d}t} + \boldsymbol{C}(\boldsymbol{u}_h) + \boldsymbol{D}\boldsymbol{u}_h - \boldsymbol{M}^*\boldsymbol{p}_h = 0, \tag{3.4}$$

$$\boldsymbol{M}\boldsymbol{u}_h = 0, \tag{3.5}$$

for $\boldsymbol{u}_h$ discrete velocities and $\boldsymbol{p}_h$ discrete pressure. Hence $\boldsymbol{\Omega}^{-1}\boldsymbol{D}$ is to be identified with $-(1/Re)\nabla^2, \boldsymbol{\Omega}^{-1}\boldsymbol{C}(\boldsymbol{u}_h)$ is to be identified with $\boldsymbol{u}\cdot\nabla$ and $\boldsymbol{\Omega}^{-1}\boldsymbol{M}^*$

is to be identified with ∇. Coefficient matrices $\boldsymbol{\Omega}$, $\boldsymbol{C}(\boldsymbol{u}_h)$, $\boldsymbol{D}$ and $\boldsymbol{M}$ are developed via a Richardson-extrapolation idea. A fourth order approximation for mass conservation is recovered from the second-order discretisation on control volumes within the fluid centred at $(x_{i-1/2}, y_{j-1/2}, z_{k-1/2})$ with faces $\Omega^{(1)}_{i,j,k} = [x_{i-1}, x_i] \times [y_{j-1}, y_j] \times [z_{k-1}, z_k]$. Volumes three times larger than these are the smallest volumes on which we can perform the same discretisation, so we consider a control volume with faces: $\Omega^{(3)}_{i,j,k} = [x_{i-2}, x_{i+1}] \times [y_{j-2}, y_{j+1}] \times [z_{k-2}, z_{k+1}]$. Elimination of the leading term of the discretisation error in the second-order continuity equation is completed by forcing conservation of mass over these volumes giving

$$\boldsymbol{M}\boldsymbol{u}_h = (3^{2+d}\boldsymbol{M}_1 - \boldsymbol{M}_3)\boldsymbol{u}_h = 0, \tag{3.6}$$

for $d = 3$ for a $3D$ grid, where coefficient matrix $\boldsymbol{M}_1$ is based on control volumes $\Omega^{(1)}_{i,j,k}$. Control volumes $\Omega^{(1)}_{i+1/2,j,k} = [x_{i-1/2}, x_{i+1/2}] \times [y_{j-1}, y_j] \times [z_{k-1}, z_k]$ for the second-order discretisation and volumes three times larger $\Omega^{(3)}_{i+1/2,j,k} = [x_{i-3/2}, x_{i+3/2}] \times [y_{j-2}, y_{j+1}] \times [z_{k-2}, z_{k+1}]$ are used for velocity $u_{i,k,k}$ to eliminate the second-order error in the $x-$ momentum equation by extrapolation (with analogous $\Omega^{(1)}_{i,j+1/2,k}, \Omega^{(3)}_{i,j+1/2,k}$ for velocity v and $\Omega^{(1)}_{i,j,k+1/2}.\Omega^{(3)}_{i,j,k+1/2}$ for velocity w in the k direction). We therefore arrive at

$$\boldsymbol{\Omega} = 3^{2+d}\boldsymbol{\Omega}_1 - \boldsymbol{\Omega}_3 \tag{3.7}$$

where $\boldsymbol{\Omega}_1, \boldsymbol{\Omega}_3$ are positive-definite diagonal matrices representing the sizes of these control volumes (i.e. $|\Omega^{(1)}_{i+1/2,j,k}|$, $\Omega^{(3)}_{i+1/2,j,k}|$, ...), and

$$\boldsymbol{C}(\boldsymbol{u}_h) = 3^{2+d}\boldsymbol{C}_1(\overline{\boldsymbol{u}}) - \boldsymbol{C}_3(\overline{\overline{\boldsymbol{u}}}), \tag{3.8}$$

where $\overline{\boldsymbol{u}}$ are the contributions through the faces of the 'original' control volumes (i.e. $\Omega^{(1)}_{i+1/2,j,k}$ for the u velocity), and $\overline{\overline{\boldsymbol{u}}}$ those through faces on the volumes three times larger (i.e. $\Omega^{(3)}_{i+1/2,j,k}$). The interpolation for the u's and $\overline{\overline{\boldsymbol{u}}}$'s on to the control faces is chosen such that the convective operator conserves energy by virtue of being skew-symmetric. The fourth-order diffusive operator is given by:

$$\boldsymbol{D} = \frac{1}{Re}(3^{2+d}\boldsymbol{\Delta}_1 - \boldsymbol{\Delta}_3)^*(3^{2+d}\boldsymbol{\Lambda}_1 - \boldsymbol{\Lambda}_3)^{-1}(3^{2+d}\boldsymbol{\Delta}_1 - \boldsymbol{\Delta}_3), \tag{3.9}$$

with $\boldsymbol{\Delta}_1^* = \text{diag}(\boldsymbol{M}_1^u, \boldsymbol{M}_1^v, \boldsymbol{M}_1^w)$, $\boldsymbol{\Delta}_1^*$ being the transpose of $\boldsymbol{\Delta}_1$, and $\boldsymbol{\Lambda}_1 = \text{diag}(\boldsymbol{\Omega}_1^u, \boldsymbol{\Omega}_1^v, \boldsymbol{M}\boldsymbol{\Omega}_1^w)$, with analogous expressions for $\boldsymbol{\Delta}_3$ and $\boldsymbol{\Lambda}_3$. Due to the staggered grid, the control volumes as used for the velocity components differ from the control volumes $\Omega_{i,j,k}^{(1)}$ and $\Omega_{i,j,k}^{(3)}$ which lead to coefficient matrices $\boldsymbol{M}_1$ and $\boldsymbol{M}_3$. Therefore new matrices $\boldsymbol{M}_1^u$, $\boldsymbol{M}_1^v$ and $\boldsymbol{M}_1^w$ (and relatives $\boldsymbol{M}_3^u$, $\boldsymbol{M}_3^v$ and $\boldsymbol{M}_3^w$) are introduced, allowing for discrete integration of the divergence of $\boldsymbol{D}\boldsymbol{u}_h$ over the control volumes for velocities u, v and w respectively. The gradient operator is approximated by

$$\boldsymbol{G} = \boldsymbol{\Omega}^{-1}\boldsymbol{M}^*, \tag{3.10}$$

for $\boldsymbol{M}^*$ the transpose of $\boldsymbol{M}$ in (3.6). The integration of the pressure gradient $\boldsymbol{G}\boldsymbol{p}_h$ over the control volumes, for discrete pressure $\boldsymbol{p}_h$, is given by $-\boldsymbol{M}^*$. Since the discrete gradient inherits the boundary conditions from the discrete divergence, boundary conditions are not required for the pressure, computed as it is from a Poisson equation, where as the Laplacian is approximated with matrix $-\boldsymbol{M}\boldsymbol{\Omega}^1\boldsymbol{M}^*$.

For boundaries, the fourth-order fully-conservative boundary scheme of Sanderse et al. (2014) is used. The boundary conditions given in Verstappen and Veldman (2003) (interior discretisation) conserve energy for homogeneous Dirichlet conditions, but do not if the boundary conditions are non-homogeneous, and the scheme also effectively introduced a Dirichlet condition on the pressure. High-order accuracy of the global error is obtained in the presence of walls with proper grid-refinement. The no-slip, impermeable Dirichlet condition is applied for velocity on wall boundaries, while Neumann condition is used for the temperature at the walls. The present code uses periodic boundary conditions in the y direction with uniform grid spacing. Ghost cells are created outside the domain boundary to facilitate the treatment of the boundary conditions. The velocity field in $y-$ direction is expanded in a Fourier series and the Navier-stokes equations are solved in wave-vector space. The discrete Fourier transform pair is defined by:

$$\tilde{g}(y,t) = \sum_k \hat{g}(k,t)e^{\mathrm{i}k\cdot y}, \;\; \hat{g}(k,t) = \frac{1}{N_y}\sum_k \tilde{g}(y,t)e^{\mathrm{i}k\cdot y}, \tag{3.11}$$

where $f \in \{v, p\}$, wave numbers $k_i = (-N_y/2..., N_y/2-1)(2\pi/L_y)$, and physical grid locations $y = (0, ..., N_i - 1)/(L_y/N_y)$, where N_y is the grid points in $y-$direction. An efficient strategy is to transform the velocity components to physical space using the fast Fourier transform (FFT).

Solutions are marched forward in time with the third-order storage low-storage Runge-Kutta scheme of Spalart (1991). The scheme uses three substeps to advance the solution for $\boldsymbol{u}_h^n$ at time t to $\boldsymbol{u}_h^{n+1}$ at time $t + \delta t$. We can rewrite our discrete representation of the momentum equation (3.4) in the following form:

$$\frac{\mathrm{d}\boldsymbol{u}_h}{\mathrm{d}t} = -\boldsymbol{\Omega}^{-1}\boldsymbol{C}(\boldsymbol{u}_h)\boldsymbol{u}_h - \boldsymbol{\Omega}^{-1}\boldsymbol{D}\boldsymbol{u}_h - \boldsymbol{G}\boldsymbol{p}_h = L(\boldsymbol{u}_h) + N(\boldsymbol{u}_h) - -\boldsymbol{G}\boldsymbol{p}_h. \quad (3.12)$$

Excluding the pressure term, we can regroup the terms in our discretised momentum equation following the notations of Spalart (1991):

$$-\boldsymbol{\Omega}^{-1}\boldsymbol{C}(\boldsymbol{u}_h)\boldsymbol{u}_h - \boldsymbol{\Omega}^{-1}\boldsymbol{D}\boldsymbol{u}_h = L(\boldsymbol{u}_h) + N(\boldsymbol{u}_h), \quad (3.13)$$

where $L(\boldsymbol{u}_h) = \boldsymbol{\Omega}_z^{-1}\boldsymbol{D}_z\boldsymbol{u}_h$ comprises the diffusion terms in the wall-normal direction and $N(\boldsymbol{u}_h) = -\boldsymbol{\Omega}^{-1}\boldsymbol{C}(\boldsymbol{u}_h)\boldsymbol{u}_h - \boldsymbol{\Omega}_{x,y}^{-1}\boldsymbol{D}_{x,y}\boldsymbol{u}_h$ contains the non-linear advective terms. Marching such a system forward in time according to their method requires the following three substeps:

$$\begin{aligned}
\boldsymbol{u}_h' &= \boldsymbol{u}_h^n + \Delta t[L(\alpha_1\boldsymbol{u}_h^n + \beta_1\boldsymbol{u}_h') + \gamma_1 N_n] - \Delta t\rho_1\boldsymbol{G}\boldsymbol{p}_h' && (3.14)\\
\boldsymbol{u}_h'' &= \boldsymbol{u}_h' + \Delta t[L(\alpha 2\boldsymbol{u}_h' + \beta_2\boldsymbol{u}_h'') + \gamma_2 N' + \zeta_1 N_n] - \Delta t\rho_2\boldsymbol{G}\boldsymbol{p}_h'' && (3.15)\\
\boldsymbol{u}_h^{n+1} &= \boldsymbol{u}_h'' + \Delta t[L(\alpha 3\boldsymbol{u}_h'' + \beta_3\boldsymbol{u}_h^{n+1}) + \gamma_3 N' + \zeta_2 N''] - \Delta t\rho_3\boldsymbol{G}\boldsymbol{p}_h^{n+1}, && (3.16)
\end{aligned}$$

where $N_n \equiv N(\boldsymbol{u}_h^n)$, $N' \equiv N(\boldsymbol{u}_h')$ and $N'' \equiv N(\boldsymbol{u}_h'')$ and

$$\begin{aligned}
\rho_1 &= \alpha_1 + \beta_1 = \gamma_1, && (3.17)\\
\rho_2 &= \alpha_2 + \beta_2 = \gamma_2 + \zeta_1, && (3.18)\\
\rho_3 &= \alpha_3 + \beta_3 = \gamma_3 + \zeta_2. && (3.19)
\end{aligned}$$

The relevant coefficients in (3.14)-(3.16) as:

$$\alpha_1 = \frac{29}{96} \quad \alpha_2 = -\frac{3}{40} \quad \alpha_3 = \frac{1}{6}$$
$$\beta_1 = \frac{37}{160} \quad \beta_2 = \frac{5}{24} \quad \beta_3 = \frac{1}{6}$$
$$\gamma_1 = \frac{8}{15} \quad \gamma_2 = \frac{5}{12} \quad \gamma_3 = \frac{3}{4}$$
$$\zeta_1 = -\frac{17}{60} \quad \zeta_2 = -\frac{5}{12}$$

The solutions are marched forward in time using the third-order low-storage Runge-Kutta scheme of Spalart (1991). The time step Δt is limited by the Courant-Friedrichs-Lewy (CFL) condition

$$N_{CFL} = \Delta t \max_{i=1,2,3} \{|u_i|/\Delta x_i\}, \tag{3.20}$$

and is set to $N_{CFL} = 1.0$ to achieve the stability for the numerical schemes.

The QUICK (Quadratic Upstream Interpolation for Convective Kinematics) of Leonard (1979) is used for the convective term in the energy equation (3.3), whereas the diffusive term is discretised using the scheme of Morinishi et al. (1998). The QUICK scheme is implemented to overcome the artifacts arising from numerical dispersion due to the implementation of the central differencing scheme. The QUICK scheme introduces numerical dissipation to control the artifacts. The artifacts were observed as wiggle-like isocontours in the temperature field observed in the simulations.

Chapter 4

Turbulent line plumes in a confined region

This chapter incorporates the results of N. George, A. Ooi, K. Moinuddin, G. Thorpe, I. Marusic & D. Chung (2016) Direct numerical simulation of a turbulent line plume in a confined region. Proceedings of the 20th Australasian Fluid Mechanics Conference 668, Perth

The purpose of the present study is to analyse confined line plumes using direct numerical simulation (DNS). We employ three Reynolds numbers (Re_H) and three plume lengths (L). We model and obtain the scaling laws for the horizontal outflow (horizontal flow after impinging the top wall) from a line source of buoyancy. Apart from investigating the transient regime of the filling box, in particular, we compare the simulation data to the theoretical models of Baines and Turner (1969) and Barnett (1991) in the asymptotic regime to test their validity.

4.1 Setup of the direct numerical simulations

Figure 4.1(a) shows the schematic of computational domain and flow configuration for the thermal line plume in a confined geometry considered in the present study. The line plume originates from a line heat source of length L and width b_0 placed along the $y-$ direction at the bottom wall. The confining box has half width R and height H in the $x-$ and $z-$directions, respectively. Here, the gravity acts in the negative $z-$direction i.e. in the opposite direction to the rising plume. Figure

4.1(b) shows an instantaneous isosurfaces of Q-criterion, which provide a clear indication of regions where vortical activity exists in a three-dimensional confined plume. In this study, we employ direct numerical simulation to solve the equations of mass, momentum and energy conservation under the Boussinesq approximation. The resulting governing equations are:

$$\frac{\partial u_i}{\partial x_i} = 0, \tag{4.1}$$

$$\frac{\partial u_i}{\partial t} + u_j \frac{\partial u_i}{\partial x_j} = -\frac{1}{\rho}\frac{\partial p}{\partial x_i} + \nu \frac{\partial^2 u_i}{\partial x_j^2} + g\beta T\, \delta_{i3}, \tag{4.2}$$

$$\frac{\partial T}{\partial t} + u_j \frac{\partial T}{\partial x_j} = \kappa \frac{\partial^2 T}{\partial x_j^2}, \tag{4.3}$$

where ν is the kinematic viscosity, g is the gravitational acceleration, β is the coefficient of thermal expansion and κ is the thermal diffusivity. Velocity components are denoted by u_i, ρ is a constant reference density, and T is the temperature. Note that, for convenience we will also use the notation convention $(u_1, u_2, u_3) = (u, v, w)$.

The flux of temperature per unit area at the wall $f_w \equiv \kappa\, |\mathrm{d}T/\mathrm{d}z|_w$ $(= q_w/(\rho\, C_p))$, where κ is the thermal diffusivity, q_w is the wall heat output per unit area (W/m^2), C_p is the specific heat at constant pressure and ρ is the reference density of the fluid; the subscript w denotes properties at the bottom wall. For numerical simulation we take a smooth Gaussian profile over a distance of $2R$ in $x-$ direction:

$$f_w = \kappa A_0 \exp(-x^2/b_0^2), \tag{4.4}$$

where A_0 is the maximum value of $|\mathrm{d}T/\mathrm{d}z|_w$ and b_0 is the plume width at $z = 0$. The buoyancy flux per unit area $= g\,\beta \times$ (temperature flux per unit area) $= g\,\beta\, f_w$. Now, buoyancy flux per unit length (in $y-$direction),

$$F_0 = g\,\beta \int_{-\infty}^{+\infty} f_w\, \mathrm{d}x = \sqrt{\pi} g\,\beta\,\kappa\, A_0\, b_0. \tag{4.5}$$

Here the turbulent plume develops as result only of heat released at the finite-sized line source on the bottom wall with no mass or momentum input. Therefore, the plume meet the requirements of a pure thermal plume (Hunt and Kaye 2001).

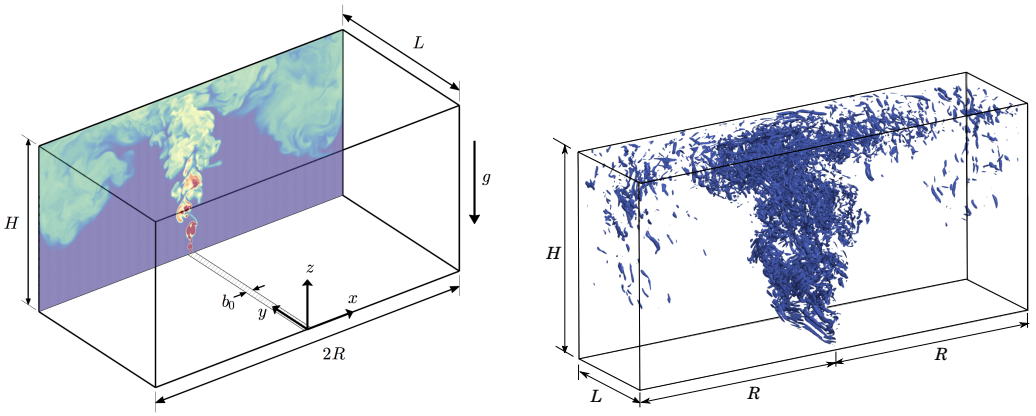

(a) (b)

FIGURE 4.1: (a) Setup of the filling box problem with contours of instantaneous temperature (hot, red and cold, blue) showing a turbulent thermal plume emerging from a line heat source at the centre of the bottom wall. b_0 is the initial plume width (the source width) and g is the acceleration due to gravity. (b) Instantaneous isosurface of Q-criterion ($Q \approx 1600$) in the filling box for $Re_H = 7200$ and $L/H = 2.0$. The Q-criterion is normalised with the buoyancy flux per unit length F_0 and the box height H.

The dimensionless parameters governing the present simulations are Reynolds number:

$$Re_H = F_0^{1/3} H/\nu \tag{4.6}$$

and Prandtl number, $Pr = \nu/\kappa$, which is fixed at the value for air: $Pr = 0.71$. We have selected three different Reynolds numbers, 1800, 3600 and 7200 for three plume lengths, $L/H = 1, 2$, and 4 (table 4.1). The values of b_0/H are 0.025, 0.0125 and 0.00625 for Reynolds numbers, 1800, 3600 and 7200, respectively.

The DNS employs a mixed spectral/finite-difference algorithm for the spatial discretisation. While a fully conservative fourth-order, staggered finite-difference scheme is used for the velocity field calculation in the $x-$ and $z-$ directions, a Fourier spectral method is used for that in the $y-$ direction. The QUICK scheme is used to advect the temperature field. The equations are marched using a low-storage third-order Runge -Kutta scheme.

Re_H	R/H	L/H	n_x	n_y	n_z	$t_{start}\,F_0^{1/3}/H$	$t_{end}\,F_0^{1/3}/H$		Approx. CPU time (hours)
1800	1	1	256	128	128	15	120		210
1800	1	2	256	256	128	14	120		450
1800	1	4	256	512	128	14	132		880
3600	1	1	512	256	256	13	95		1800
3600	1	2	512	512	256	13	71		3400
3600	1	4	512	1024	256	12	73		6800
7200	1	2	1024	1024	512	12	64	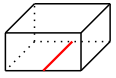	27500
3600	2	1	1024	256	256				3750
3600	4	1	2048	256	256				6800
3600	8	1	4096	256	256				14200
3600	16	0.5	8192	128	256			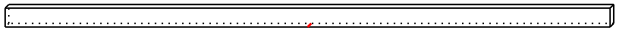	16520

TABLE 4.1: Simulation parameters of the present case.

Baines and Turner (1969) found that in order to avoid a large-scale circulation generated by the plume in the confined box, the stabilising buoyancy force in the region of plume outflow at the top of the box must be larger than the inertial force of the plume. The ratio between these forces depends purely on the geometry of the box, i.e. aspect ratio (R/H), not on the buoyancy flux or other flow properties. In their experiments, they concluded that the critical value of the aspect ratio is about one. Therefore, in the present case, the aspect ratio (R/H) of the box is set to one.

The bottom, top, left, and right boundaries are no-slip walls. Periodic boundary conditions are imposed on velocities (u_i), pressure (p) and temperature (T) in the $y-$direction. We set all initial velocities to zero and add a random perturbation to the temperature field in a semi-circular prism region $x^2 + z^2 < (2\,b_0)^2$, near the plume source, in order to trigger a transition to turbulence in the rising plume before the plume reaches the top wall. The magnitude of temperature perturbations $(T(t = 0))$ added to the flow is based on $(g\,\beta\,T\,b_0)^{1/2}\,b_0/\nu = 1.2$, and is kept constant for all simulations.

The grid spacing is uniform in the $x-$, $y-$ and $z-$directions. The resolutions of the present simulations are kept constant relative to $F_0^{1/3}$ and ν and the resolutions are based on the Kolmogorov length scale, $\eta = (\nu^3/\bar{\epsilon})^{1/4}$, where $\bar{\epsilon} = 15\nu\overline{(\partial w'/\partial z)^2}_{x=0}$ is the turbulent dissipation along the plume centre line in the asymptotic state. The initial Gaussian plume width (b_0) is calculated based on the ratio of the Gaussian width of temperature gradient distribution, which we imposed on the bottom wall of the box, to the grid spacing in the x-direction. The value of b_0 is maintained as small as possible to approximate as a line heat source. The ratio $b_0/\Delta x$ is fixed equal to 3.2 to ensure that there are 6 grid points on both sides of the Gaussian curve in order to ensure the numerical stability of the code.

In the present simulation, once the domain size, $(2R, L, H)$ is fixed, the number of grid points in all directions (n_x, n_y, n_z) and the kinematic viscosity (ν) are arbitrarily chosen as in a physical experiment. For a given Prandtl number $(Pr = 0.71)$ κ is then fixed. Similarly, a chosen Re_H provides F_0, which after using (4.5) fixes the value of the product βA_0. The value of β goes in (4.2) as A_0 provides the Neumann boundary condition via (4.4). The individual values of β and A_0 are arbitrary as long as the product βA_0 is fixed. For numerical discretisation for the first simulation, we arbitrarily choose the number of grid points in all directions

(n_x, n_y, n_z), such that $\Delta x = \Delta y = \Delta z$. We will firstly discuss the identification of the asymptotic state and return to verify that the resolution we have chosen is indeed sufficient for these simulations to be called a DNS (i.e. $\Delta x/\eta \approx 3$).

We denote the line-averaged properties along the $y-$ direction using $\widetilde{(\cdot)}$, which is defined as

$$\widetilde{(\cdot)} = \frac{1}{L}\int_0^L (\cdot)(x, y, z, t)\,\mathrm{d}y\,. \tag{4.7}$$

We use $\overline{(\cdot)}$ to denote the line-averaged and time-averaged properties, defined as

$$\overline{(\cdot)} = \frac{1}{N}\sum_{n=1}^{N}\frac{1}{L}\int_0^L (\cdot)(x, y, z, t_n)\,\mathrm{d}y\,, \tag{4.8}$$

where N is the total number of samples in time. The mean variance can be defined as $\overline{(\cdot)'^2}$. We can define fluctuations of the velocities about the mean quantities defined above, say for vertical velocity w,

$$w(x, y, z, t) = \widetilde{w}(x, z, t) + w''(x, y, z, t), \tag{4.9}$$

$$w(x, y, z, t) = \overline{w}(x, z) + w'(x, y, z, t), \tag{4.10}$$

where w'' and w' are the fluctuations about (4.7) (y-direction) and (4.8) respectively.

The time-averaged statistics are only calculated when the flow has reached the asymptotic state. To identify the beginning of the asymptotic state, figure 4.2(a) shows the evolution of the volume-averaged temperature, $\langle T\rangle$, and the line-averaged temperatures at different locations in the box for $Re_H = 3600$ and $L/H = 1$. It is clear that the temperature at all measured locations have reached the asymptotic state after $t{F_0}^{1/3}/H \approx 28$, because the line and volume averaged temperature at every point is increasing linearly with time. We can derive an expression for $\langle T\rangle$ in terms of time t from (4.3),

$$\frac{g\beta H\langle T\rangle}{{F_0}^{2/3}} = \frac{H/R}{2}\frac{{F_0}^{1/3}\,t}{H}. \tag{4.11}$$

From (4.11), when one plots temperature (non-dimensionalized using ${F_0}^{2/3}/g\beta H$) and time (non-dimensionalized with $H/{F_0}^{1/3}$), it can easily be seen that the slope of the line should be $(H/R)/2$, where H/R is inverse of the aspect ratio of the box .

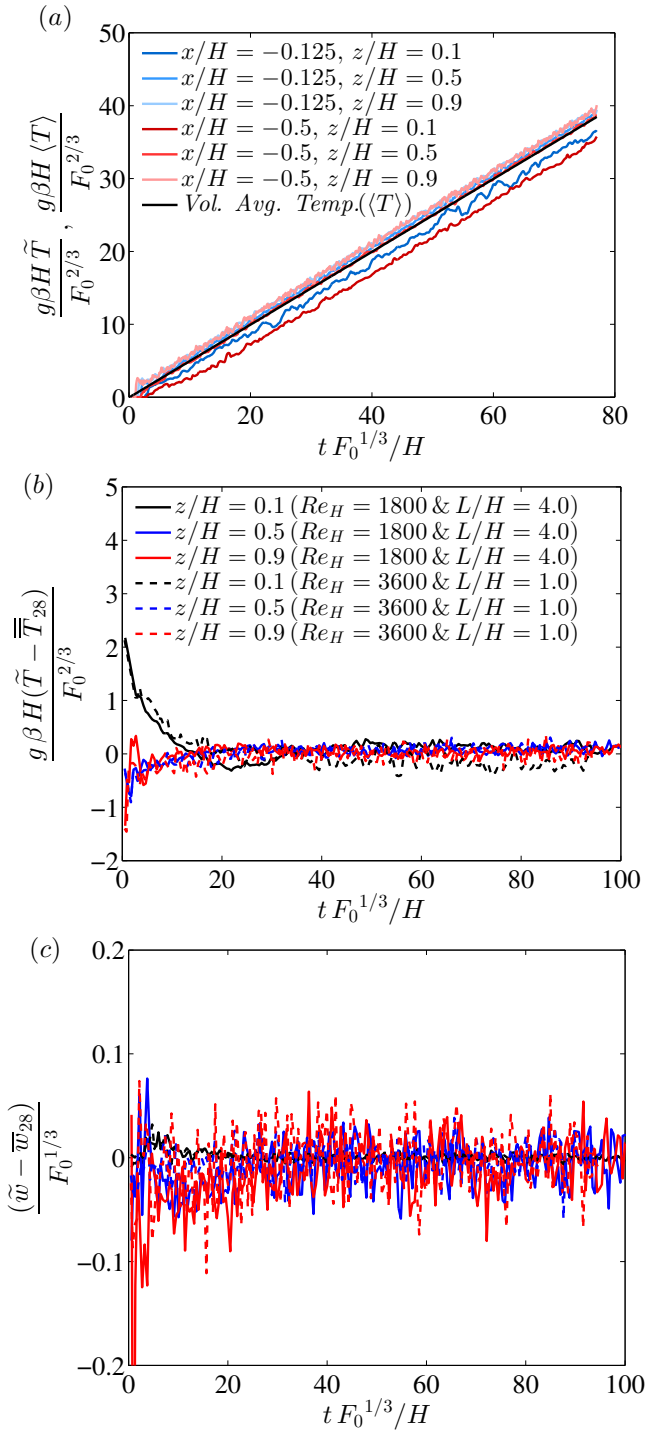

FIGURE 4.2: (a) Temperature fluctuations ($\widetilde{T}$) at different points and evolution of volume averaged temperature ($\langle T \rangle$), the asymptotic evolution of (b) temperature and (c) vertical velocity in the filling box, for $Re_H = 3600$ and $L/H = 1.0$. The legend (b) applies to (c).

We will identify the start of the asymptotic state as the location where the line-averaged temperature has a constant slope of $(H/R)/2$. Therefore, we have plotted the quantity $(\widetilde{T} - \overline{\overline{T}}_{28})$ as a function of time, where $\overline{\overline{T}}_{28}$ is a straight line fitted

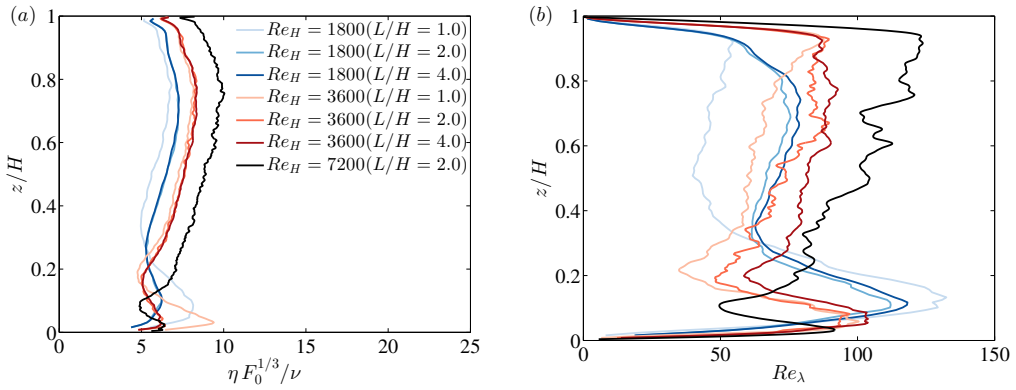

FIGURE 4.3: Kolmogorov (a) and Taylor Reynolds numbers (b) at the plume centreline for different Re_H and L/H cases. The legend (a) applies to (b).

to the data of non-dimensionalized $\widetilde{T}$ and t after 28 non-dimensionalized time units. The term $\overline{\overline{T}}$ can be expressed as $\overline{\overline{T}}(x,z,t) = pt + q$, where p is the slope which is set to $(H/R)/2$ and q is the point at which the line crosses the $\widetilde{T}$-axis and the value of q can be calculated from the linear regression equation. From figure 4.2(b), we can observe that the quantity $(\widetilde{T} - \overline{\overline{T}}_{28})$ reaches a statistically steady state at $t{F_0}^{1/3}/H \approx 13$. We have also plotted $(\widetilde{w} - \overline{w}_{28})$ as a function of time (figure 4.2c) to identify the time when vertical velocity reaches the asymptotic sate. In that case, the statistics of the vertical velocity quickly reaches the self-similar state compared to the temperature statistics. The data plotted in figure 4.2(b) and (c) are averaged over three points in x-direction (i.e. $x/H = -0.75$, -0.5 and -0.25). Thus, the start of the asymptotic state for the present case is set close to $t{F_0}^{1/3}/H \approx 13$. The commencement of the asymptotic state ($t_{start}{F_0}^{1/3}/H$) for different cases are shown in table 4.1. After the asymptotic state is reached, mean statistics are computed by averaging over at least 60 non-dimensional time units at the interval of 0.42 time units.

Note that at the asymptotic state, it can be shown that

$$\frac{1}{\rho H}(\widetilde{p}(x = H) - \widetilde{p}(z = 0)) = g\beta\langle T\rangle. \tag{4.12}$$

Hence the increase in T is perfectly balanced by the pressure difference between the top and bottom walls. So both the temperature and pressure will increase but the values of the velocities do not increase with time.

The basic requirement for conducting DNS is to resolve the smallest dissipative scale, i.e. the Kolmogorov scale of the flow. Figure 4.3(a) shows the variations

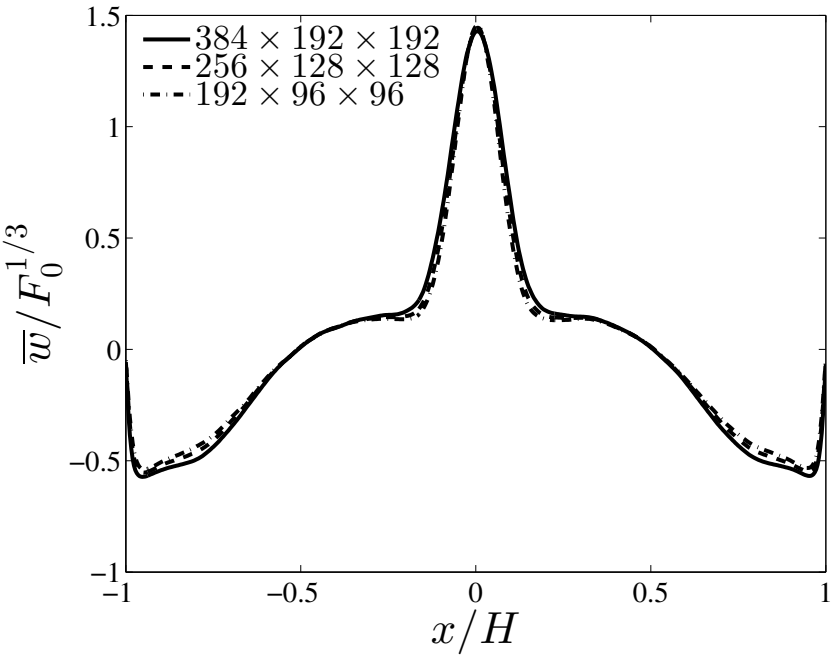

FIGURE 4.4: The variation of mean velocity profile at $z/H = 0.5$ for $Re_H = 1800$ and $L/H = 1.0$ for various grid densities.

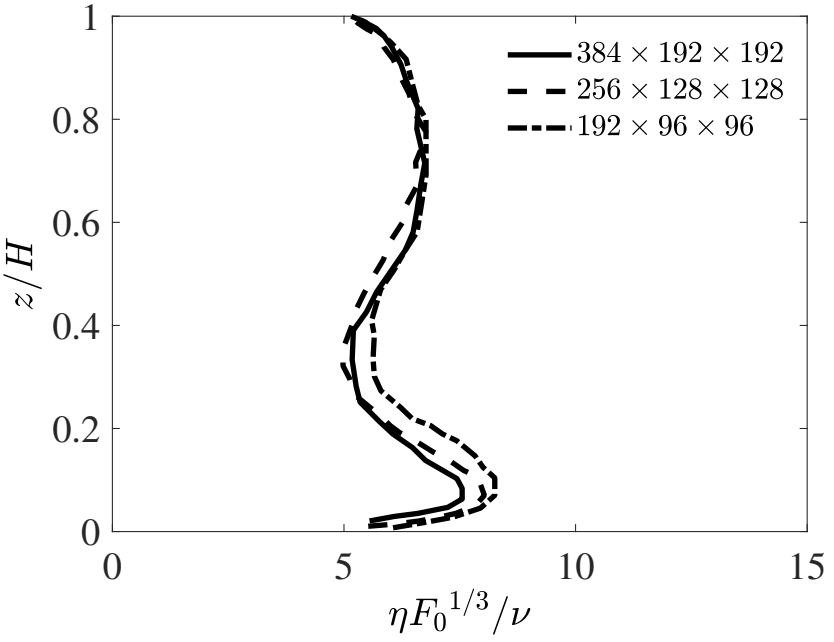

FIGURE 4.5: Kolmogorov results at the plume centreline for $Re_H = 1800$ and $L/H = 1.0$ for various grid densities.

of Kolmogorov length scale along the plume centreline (i.e. $x/H = 0$) for all the cases simulated here. In the present study, we observed that the maximum ratio between physical grid spacing and the Kolmogorov length scale is about 2.93 at $z/H = 0.16$, which satisfies the criteria $[\Delta x, \Delta y, \Delta z]_{max} \leq \pi\eta$ (see Stevens et al. 2010). We note that grid resolutions Δx, Δy and Δy are fixed to fully resolve all the turbulent scales up to the Kolmogorov scale by following the recommendations Stevens et al. (2010), as well as employing a grid independence test. To see the effect of size of the numerical grid, a thorough grid independent test has been conducted for aspect ratio $R/H = 1.0$ with $Re_H = 1800$ case. Three levels of grids namely, $384 \times 192 \times 192$, $256 \times 128 \times 128$ and $192 \times 96 \times 96$ have been tested. Figure 4.4 shows the variation of mean velocity profile at $z/H = 0.5$ for $Re_H = 1800$ and $L/H = 1.0$ for various grid densities. Kolmogorov results at the plume centreline for various grid densities are shown in figure 4.5. It has been observed that as the grid is refined, variation in the results between two successive grids decreases. For the two finest level of grids, variation in mean velocity remains below 1%. This also led us to use the resolutions of the grid $256 \times 128 \times 128$ to achieve consistent accuracy. Therefore, the current grid spacing is considered to be fine enough to capture the entire range of flow scales.

It can also be seen from Figure 4.3(a) that the smallest length scales are towards the lower end of the computational domain. For our initial simulations we observed (empirically) that the minimum value of $\eta {F_0}^{1/3}/\nu \approx 4.7$. For all future simulations we used $\eta {F_0}^{1/3}/\nu = 4.7$ to obtain the approximate value of η, which was then employed to obtain the required resolution.

The variation of the Taylor Reynolds number Re_λ is shown in figure 4.3(b). The Taylor Reynolds number is defined as $Re_\lambda = (\overline{w'^2})_{x=0}^{0.5}\,\lambda/\nu$, where $\lambda = (\overline{w'^2})_{x=0}^{0.5}/(\partial\overline{w'^2}/\partial z)_{x=0}^{0.5}$. In the turbulent region of the plume (i.e. $z/H > 0.2$), the maximum values of Re_λ are observed in the region close to $z/H = 0.8$ and the values of Re_λ are 80, 90 and 110 for $Re_H = 1800$, $Re_H = 3600$ and $Re_H = 7200$, respectively.

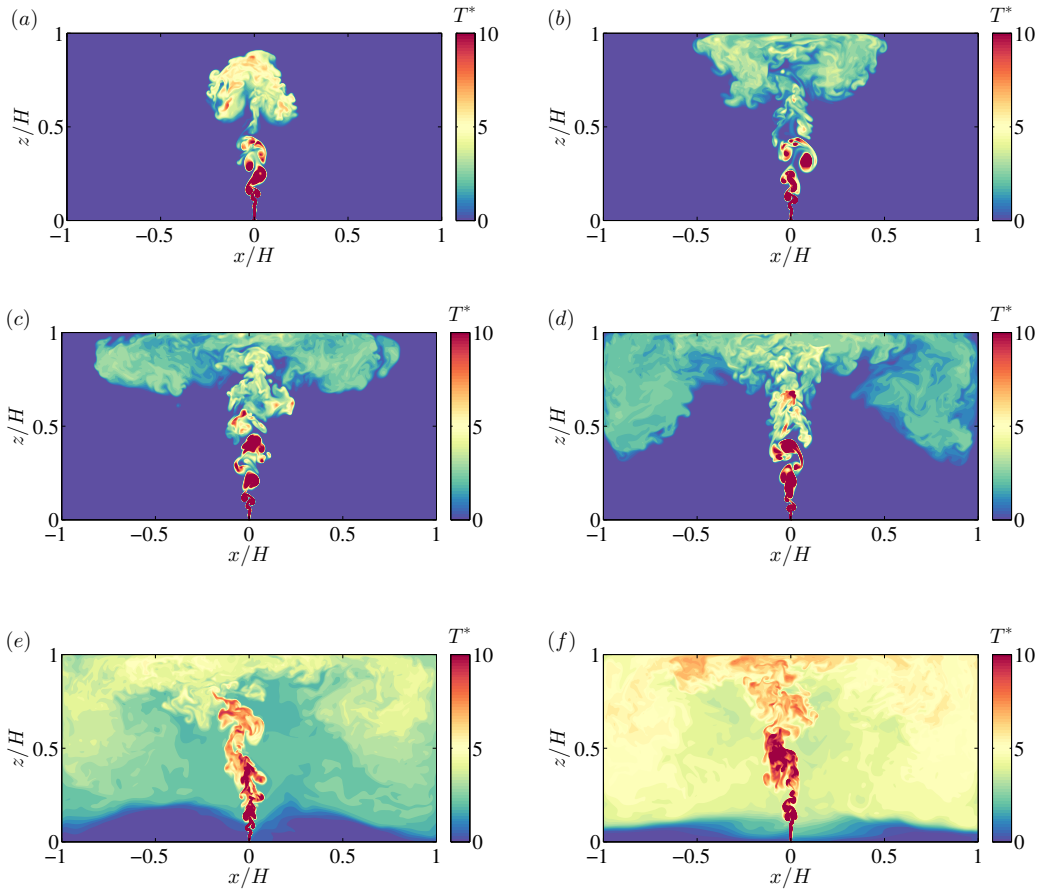

FIGURE 4.6: Contour plots of the instantaneous temperature (at $y/H = 0.5$) showing the evolution of the plume to the asymptotic state for $Re_H = 7200 (L/H = 2.0)$; (a) $t^* = 0.82$; (b) $t^* = 1.18$; (c) $t^* = 1.57$; (d) $t^* = 2.32$; (e) $t^* = 5.83$; and (f) $t^* = 9.04$.

4.2 The filling box regimes

Figure 4.6 shows a series of instantaneous contour plots of the temperature field for $Re_H = 7200$ and $L/H = 2.0$ at the location $y/H = 1.0$ in order to visualise the evolution of the plume from the transient to the asymptotic state. The non-dimensional temperature and time are, respectively, defined as, $T^* = T/({F_0}^{2/3}/g\beta H)$ and $t^* = t/(H/{F_0}^{1/3})$. At the start of the simulation, the plume emerges from a line heat source located at the centre of the bottom wall in a uniform environment. Initially, the plume is laminar, and at some point between the top and bottom wall, it becomes turbulent (figure 4.6*a*). In the region $0.2 \leq z/H \leq 0.4$ there is a clear indication of the presence of large scale eddies in the left and right sides of the plume. Later, these eddies interact with each other by their rolling motion and engulf ambient fluid and incorporate it into the

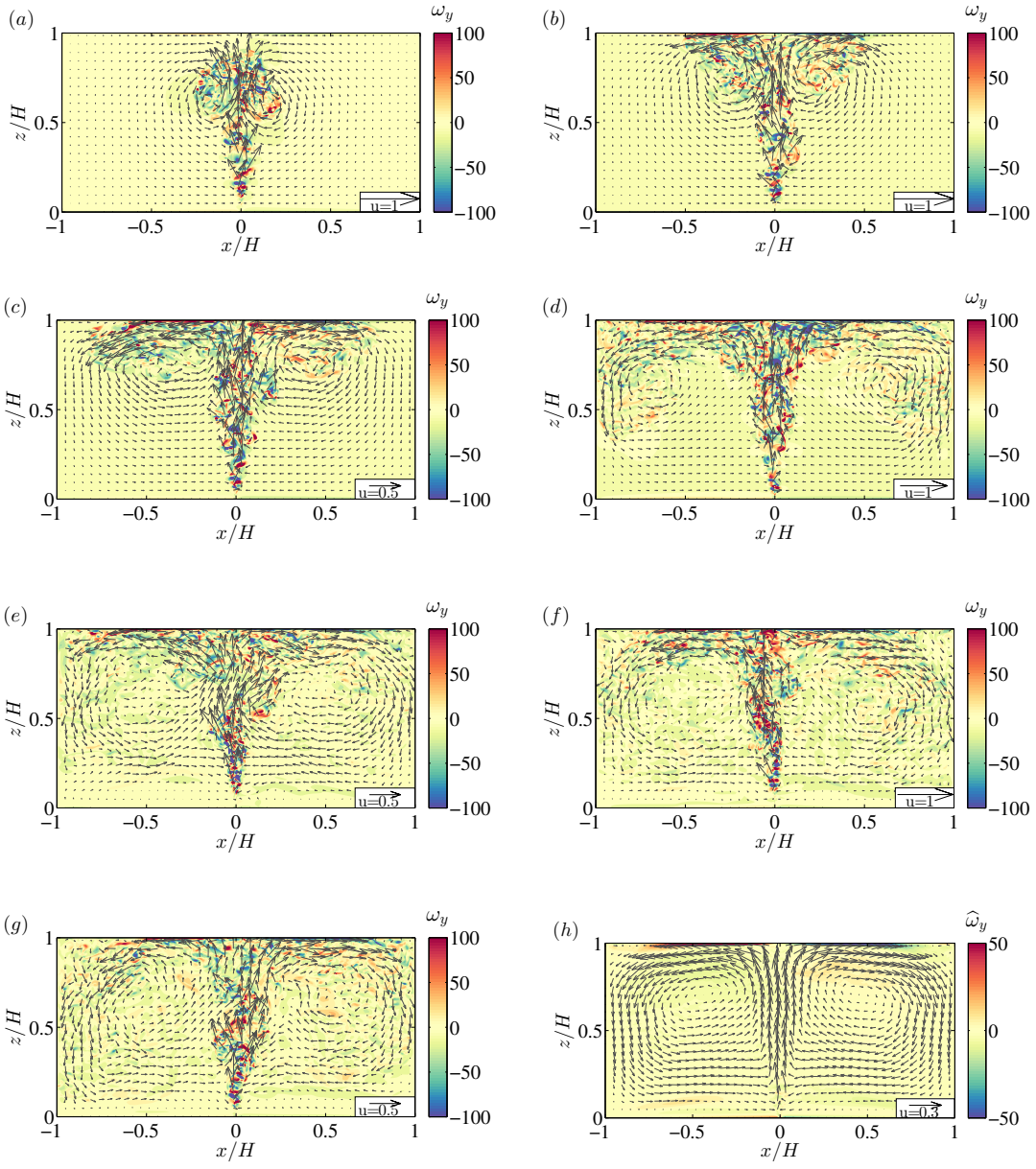

FIGURE 4.7: Vorticity distributions and velocity vectors for $Re_H = 7200$ and $L/H = 2.0$; (a) $t^* = 0.82$; (b) $t^* = 1.18$; (c) $t^* = 1.57$; (d) $t^* = 2.32$; (e) $t^* = 5.83$; (f) $t^* = 9.04$; (g) $t^* = 11.9$; and (h) time-averaged contour of ω_y.

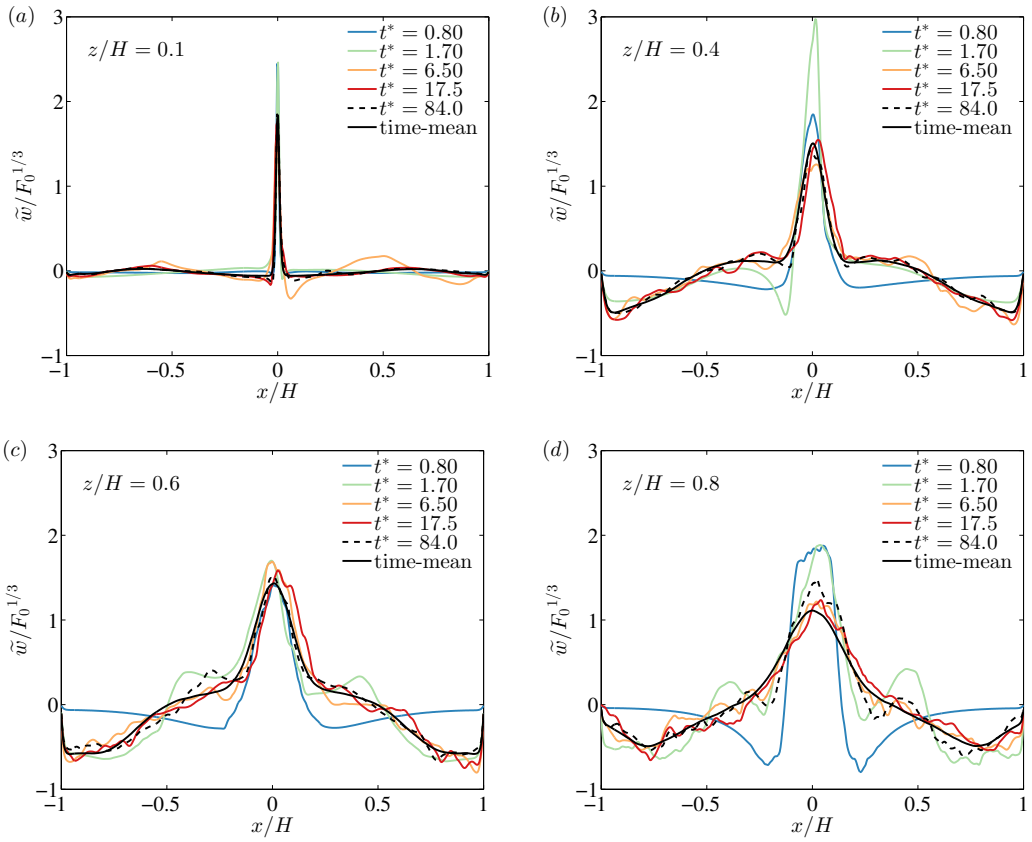

FIGURE 4.8: Horizontal profiles of line-averaged vertical velocity ($\widetilde{w}$) at different times and different z/H locations for $Re_H = 3600$ and $L/H = 1.0$.

mainstream flow. The rising plume impinges on the top wall of the confined box and spread towards the side walls (figures 4.6*b* and *c*). When the laterally spreading plume impacts the side walls, an overturning motion is set up (see Kaye and Hunt 2007) and the outflow moves vertically downwards against the direction of buoyancy (figure 4.6*d*). Eventually, the entire box is filled with fluid that comes from the plume outflow (figures 4.6*e* and *f*), and the fluid inside the box is said to have reached the asymptotic state.

To clearly elucidate the dynamics of the plume in a confined environment, figure 4.7 shows vorticity contours overlaid on velocity vectors plots for the evolution of the plume for case $Re_H = 7200$ and $L/H = 2$. In the region located near the heat source, a strong vertical motion occurs due to the continuous supply of the buoyancy at the bottom wall. After the plume impinges on the top wall, we observe the exchange of fluid from the plume outflow to a surrounding ambient environment. Also, two counter-rotating circulations are formed near the sidewalls (figure 4.7*c*). Later, a strong downward motion is observed through the sidewalls

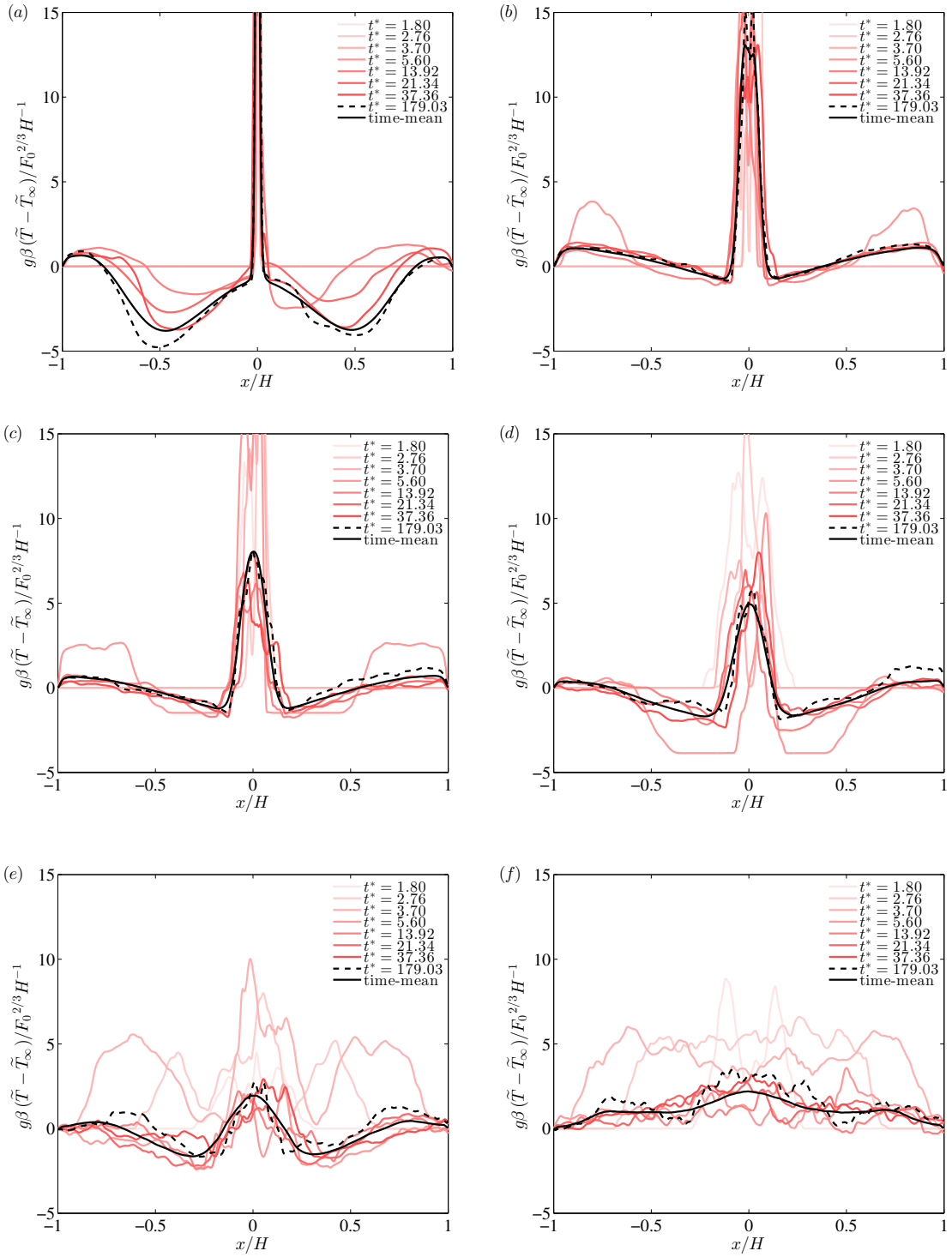

FIGURE 4.9: Horizontal profiles of line-averaged reduced gravity at different times and different z/H locations for $Re_H = 3600$ and $L/H = 1.0$.

(figure 4.7d) and then the plume outflow re-entrained into the plume (figure 4.7e). Figure 4.7(h) shows the smoothed vorticity and the velocity vectors at $t^* \approx 16.9$. Here the smoothed contour is generated by averaging across three adjacent time instances ($\widehat{\omega}_y$) with time interval $\Delta t^* \approx 0.5$. Two symmetrical vortex cells are observed at $t^* \approx 16.9$, which is in the asymptotic state.

The horizontal variations of line averaged vertical velocity ($\widetilde{w}$) at different vertical locations (z/H) is plotted in figures 4.8. The different colours indicate the vertical velocity profiles at different times. Blue colour indicates the lower time profile and the red colour indicates the higher time profiles. It can be observed for $z/H = 0.1$ that the vertical velocity profile (figure 4.8a) shows a sharp peak at all times. This is due to an intense flow development in the region very close to the heat source. When moving away from the source, the value of vertical velocities near the side walls become negative due to the downward movement of the plume outflow. Therefore, these velocity profiles are different from the plumes in an open environment. These velocity profiles remain very similar in shape after 12 time units, i.e. after the interface layer reaches the bottom wall (figure 4.6f). It is seen that the profiles at time 84 closely follow the time-averaged profiles.

The horizontal variations of line averaged reduced gravity, $g\beta(\widetilde{T} - \widetilde{T}_\infty)$, at different vertical locations (z/H) is plotted in figures 4.9. The reduced gravity profiles are similar to the vertical vertical velocity profiles at different box heights. Here, the reduced gravity is calculated by subtracting the environmental temperature (T_∞) from the temperature inside the box (T). The environmental temperature (T_∞) is defined as the temperature at $x/H = -0.99$, i.e. far away from the plume. Reduced gravity profiles remain very similar in shape after 22 time units, i.e. after the interface layer reached the bottom of the wall (figure 4.9 (f)). It is seen that the profiles at time 179 are closely followed the time-averaged profiles.

4.3 Analytical models of a confined plume

4.3.1 Governing equations and Baines and Turner (1969)'s model

Baines and Turner (1969) first studied the stratification developed by a turbulent plume originated from a local heat source in a confined region, which is commonly

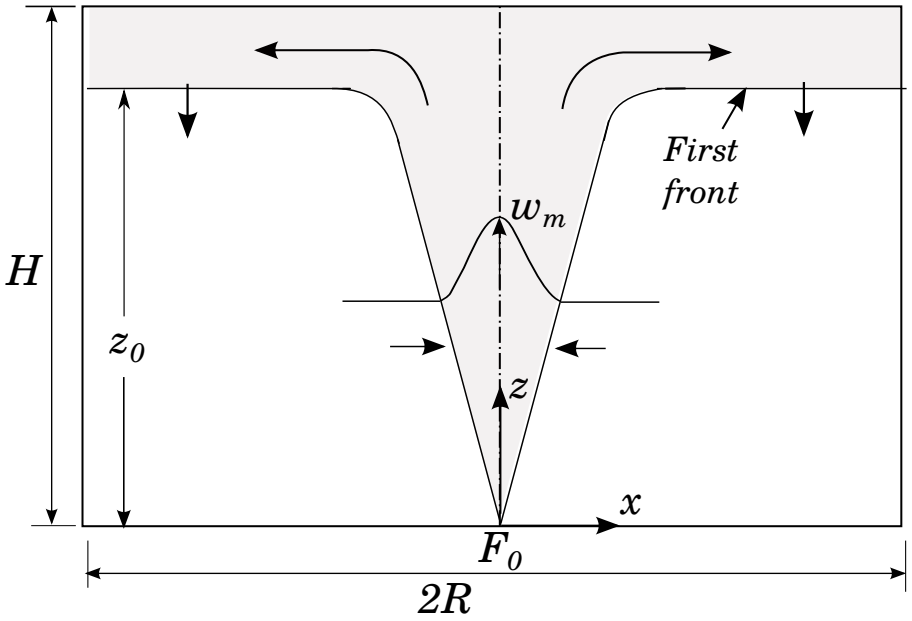

FIGURE 4.10: Schematic diagram of filling box problem

referred to as a filling box, problem. In order to validate the filling box model with the present DNS data, we review the theory of Baines and Turner (1969). The filling box model is shown schematically in figure 4.10, where a line heat source is located on the bottom wall of a box, the box height and width are H and $2R$, respectively. The source generates a buoyancy flux F_0 per unit length and zero fluxes of volume and momentum.

To derive the steady-state solution for turbulent line plume in a confined region, we begin by considering the volume Q, momentum M, and buoyancy fluxes F for a line plume. The fluxes Q, M and F are defined respectively by

$$Q = \int_{-x_\infty}^{+x_\infty} \overline{w}\,\mathrm{d}x, \qquad M = \int_{-x_\infty}^{+x_\infty} \overline{w}^2\,\mathrm{d}x, \qquad F = \int_{-x_\infty}^{+x_\infty} g\beta\,(\overline{T} - \overline{T}_\infty)\,\overline{w}\,\mathrm{d}x, \tag{4.13}$$

where the integration limit x_∞ is taken outside the plume region and $\overline{T}_\infty$ is the ambient temperature outside the plume. Also, the mean velocity in the vertical direction z is denoted by $\overline{w}$, and in the $x-$direction is denoted by $\overline{u}$.

Expressions for Q, M, and F can be derived by integrating the Reynolds averaged momentum equations, continuity equation (see Lee and Emmons 1961), and following the definitions in (4.13). The governing equation for the volume flux is

given by

$$\frac{\mathrm{d}Q}{\mathrm{d}z} = 2u_e\,, \tag{4.14}$$

where Q is the volume flux and u_e is the entrainment velocity ($u_e = \overline{u}|_{\pm x_\infty}$) which is evaluated far from the plume. The governing equation for the momentum flux is given by

$$\frac{\mathrm{d}M}{\mathrm{d}z} = \int_{-x_\infty}^{+x_\infty} g\beta\,(\overline{T} - \overline{T}_\infty)\,\mathrm{d}x. \tag{4.15}$$

Note that in the steady state, the ambient fluid will become stratified with a mean temperature gradient $\mathrm{d}\overline{T}_\infty/\mathrm{d}z$. Consequently, the equation for the buoyancy flux is given by

$$\frac{\mathrm{d}F}{\mathrm{d}z} = -Q\,\frac{\partial \Delta_\infty}{\partial z}, \tag{4.16}$$

where F is the buoyancy flux and $\partial\Delta_\infty/\partial z$ is the environmental buoyancy gradient which can be expressed in terms of environmental temperature gradient $\partial\Delta_\infty/\partial z = g\,\beta\,\partial\overline{T}_\infty/\partial z$.

The mean vertical velocity ($\overline{w}$) and reduced gravity ($g\beta(\overline{T} - \overline{T}_\infty)$) are approximated by a Gaussian form, i.e. $\overline{w} = w_m \exp(-x^2/b_w^2)$ and $g\beta(\overline{T} - \overline{T}_\infty) = \Delta(z)\exp(-x^2/b_T^2)$, where $w_m(z)$ is the centreline vertical velocity, $\Delta(z)$ is the centreline reduced gravity

$$\Delta = \Big(\, g\beta(\overline{T} - \overline{T}_\infty)\Big)_{\max}, \tag{4.17}$$

and b_w and b_T are typical plume width associated with the vertical velocity and reduced gravity, respectively. Here, Gaussian profiles of equal width have been assumed for the vertical velocity and reduced gravity fields in the plume, i.e. $b_w = b_T = b$.

As suggested by Morton et al. (1956), the rate at which fluid is entrained into the plume is taken as proportional to the mean vertical velocity on the axis of the plume, $u_e = \alpha\, w_m$, where α is the entrainment coefficient.

Now we can express the fluxes in terms of the maximum vertical velocity, $w_m(z)$, and reduced gravity, $\Delta(z)$, along with a plume width, $b(z)$, after employing (4.13) are given by

$$Q = \sqrt{\pi}\,b\,w_m, \qquad M = \sqrt{\pi/2}\,b\,w_m^2, \qquad F = \sqrt{\pi/2}\,b\,w_m\,\Delta\,. \tag{4.18}$$

In terms of the fluxes, (4.14) and (4.15) become

$$\frac{\mathrm{d}Q}{\mathrm{d}z} = 2\sqrt{2}\,\alpha\frac{M}{Q}, \tag{4.19}$$

and

$$\frac{\mathrm{d}M}{\mathrm{d}z} = \frac{FQ}{M}, \tag{4.20}$$

respectively.

The plume equations described above are valid for the line plumes in unconfined environments(e.g. Lee and Emmons 1961; Paillat and Kaminski 2014a). In the case of confined plumes, two other equations are considered for describing the environmental flow parameters. The conservation of mass in the filling box can be written as

$$Q = -2RU, \tag{4.21}$$

where U is assumed to be the magnitude of uniform downward velocity of the environment, and the plume width is taken to be much smaller than the width of the box $2R$ (Baines and Turner 1969). Also, the development of the buoyancy field in the environment is governed by

$$\frac{\partial \Delta_\infty}{\partial t} = -U\frac{\partial \Delta_\infty}{\partial z}. \tag{4.22}$$

Furthermore, Baines and Turner (1969) developed an analytical model for the position of the buoyant layer formed after the plume impinges on the top wall as a function of time, which is described in section 4.3.2.

4.3.2 The first front propagation

When the buoyant fluid first impinges on the upper boundary of the confined box, a horizontal thin buoyant layer is formed and then proceed downwards. The dynamics of horizontal spreading-out flow is ignored. The interface between the buoyant fluid and the ambient fluid is referred as the first front. This terminology was first introduced by Baines and Turner (1969). After this layer reaches the bottom wall, the flow is said to be in the asymptotic state (Baines and Turner 1969). The rate of advancement of the first front can be calculated by considering the uniform temperature case, i.e. $\partial \overline{T}_\infty/\partial z = 0$. The properties of the plume below the front (see Morton et al. 1956) can be expressed in terms of the buoyancy

flux, F_0 and z, using (4.19) and (4.20), where

$$F_0 = \sqrt{\pi/2}\, b\, w_m\, \Delta\Big|_{z=0}, \text{ and,} \tag{4.23}$$
$$b = \frac{2}{\sqrt{\pi}}\alpha z,\ w_m = {F_0}^{1/3}\alpha^{-1/3}, \text{ and } \Delta = \frac{1}{\sqrt{2}}{F_0}^{2/3}\alpha^{-2/3}z^{-1}.$$

A DNS study of the line plume in a uniform environment is described in appendix A to verify present DNS setup by using the classical plume theory.

The velocity of the front, $U = \mathrm{d}z_0/\mathrm{d}t$, where z_0 is the first front height (figure 4.10), is obtained when (4.21) and (4.23) are applied at this level, $\mathrm{d}z_0/\mathrm{d}t = -{F_0}^{1/3}\alpha^{2/3}R^{-1}z_0$. Integration gives the relationship between first front position z_0 (measured from the bottom wall) and the time t (Baines and Turner 1969). The time $t = 0$ is defined when the plume first reaches the top wall (i.e. $z_0 = H$),

$$\tau \equiv {F_0}^{1/3}\,\alpha^{2/3}\,R^{-1}\,t = -\ln(z_0/H). \tag{4.24}$$

4.3.3 Environmental temperature profiles

Worster and Huppert (1983) presented an approximate analytical expression for the time-dependent environmental temperature profile by using Baines and Turner's filling box model. These profiles are used here to compare present DNS results. Figure 4.11 shows the comparison of Worster and Huppert's analytical expression with present DNS results. The solid black line shows Worster and Huppert's analytical solution and black dashed line shows the numerical solution (time-dependent environmental temperature profile obtained from the Baines and Turner's model) which is explained in appendix B. The dash-dotted line indicates the position of the first front at each non-dimensional time τ (see 4.24).

In figure 4.11, the symbols represent the horizontally averaged temperatures from $x/H = \pm 0.25$ to $x/H = \pm 0.99$. The approximate analytical solutions of Worster and Huppert's and numerical solutions described in Appendix B are matched for all times (figure 4.11). Considering the assumptions involved, the model shows reasonable agreement for the buoyancy profile with the DNS results at all times. However, the observed interface locations are different from the model and DNS data over predicted the analytical model below $z/H \approx 0.6$. This discrepancy

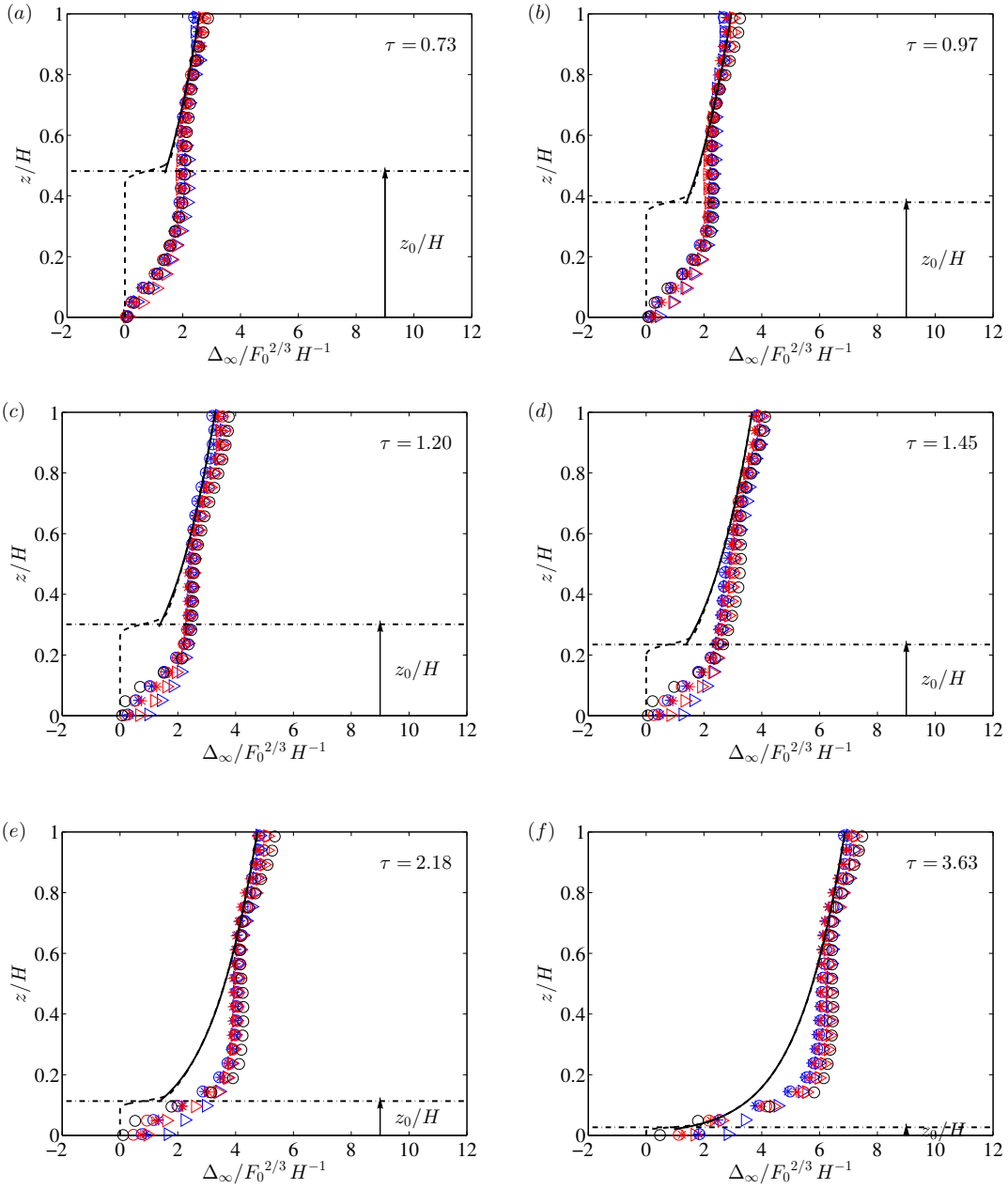

FIGURE 4.11: Comparison of environmental temperature profiles at different non-dimensional times ($\tau = {F_0}^{1/3}\,\alpha^{2/3}\,R^{-1}\,t$) for different Re_H and L/H cases. Blue, red and black symbols are used for Reynolds numbers $Re_H = 1800$, 3600 and 7200, respectively. Triangles, circles, and diamonds represent the $L/H = 1, 2, 4$ cases respectively. The solid black line shows Worster and Huppert (1983)'s analytical solutions, dashed line shows the numerical solution and dash-dotted line shows the position of the first front; (a) $\tau = 0.73$, $t^* = 2.13$; (b) $\tau = 0.97$, $t^* = 2.83$; (c) $\tau = 1.2$, $t^* = 3.5$; (d) $\tau = 1.45$, $t^* = 4.2$; (e) $\tau = 2.18$, $t^* = 6.37$; and (f) $\tau = 3.63$, $t^* = 10.6$.

appears to result from the fact that buoyant fluid outside the plume is not as uniform as is assumed in the analysis. This may be due to the overturning of the upper buoyant fluid layer during the initial transients. This would suggest that even larger values of R/H might be required to before the inertial overturning effects become negligible.

4.3.4 The asymptotic state

We now consider the full set of equations (three plume equations, 4.14 - 4.16 and two describing the environment, 4.21 - 4.22) for obtaining the asymptotic solutions () of confined plume variables. In the asymptotic state, we can define the non-dimensionalised plume variables as

$$Q/(F_0^{\frac{1}{3}}H) = 2\,\alpha^{\frac{2}{3}}\,q(z/H), \tag{4.25}$$

$$M/(F_0^{\frac{2}{3}}H) = \sqrt{2}\,\alpha^{\frac{1}{3}}\,m(z/H), \tag{4.26}$$

$$F/F_0 = f(z/H), \tag{4.27}$$

$$\Delta_\infty/(F_0^{\frac{2}{3}}H^{-1}) = 2^{-1}\alpha^{-\frac{2}{3}}\,[f_0(z/H) - \tau], \tag{4.28}$$

$$U/(F_0^{\frac{1}{3}}H/R) = \alpha^{\frac{2}{3}}\,j(z/H), \tag{4.29}$$

where q, m, f, f_0 and j are the dimensionless variables in terms of vertical distance from the plume source, and τ is the non-dimensional time defined in (4.24). A set of power series solutions is obtained for these dimensionless variables and which is not mentioned here. Note that the above equations are slightly different from Baines and Turner (1969), because they did not consider a factor of 2 that appears in right-hand-side of the volume flux equation 4.14.

4.3.5 Barnett(1991)'s model

Barnett (1991) extended the filling box model for round plumes by considering aspect ratios less than unity. In that case, the environmental downward momentum plays a significant role in the filling box process. But the line plume in the filling box with aspect ratio equal to unity also experiences sufficient downward momentum in the environment. Therefore, similar to Barnett (1991), the momentum equation is modified by considering the environmental downward momentum

flux. In the case of line plume, the momentum conservation equation (4.20) can be rewritten as

$$\frac{\mathrm{d}}{\mathrm{d}z}(M + M_d) = \frac{F\,Q}{M}, \tag{4.30}$$

where M_d is the downward momentum flux which is defined as $(2R - 2b)\,U^2$ and the mass conservation in the filling box, can be rewritten as $Q = -(2R - 2b)\,U$, the final momentum flux equation can be rearranged and simplified for $AR = 1$ as

$$\frac{\mathrm{d}M}{\mathrm{d}z} = \frac{-8\sqrt{2}\pi\alpha M^4 + 4\pi F M^2 Q - 4\sqrt{2\pi} F M Q^3 + 2F Q^5}{M(4\pi M^2 - 4\sqrt{2\pi} M Q^2 + (2 - \sqrt{2\pi})Q^4)} \tag{4.31}$$

and other equations remain unchanged.

4.4 Comparison between DNS and theoretical models

4.4.1 Plume centreline alignment

Before we carry out any quantitative comparison between the different models and DNS, in the asymptotic state we observed that the turbulent line plume within a confined space shows a flapping behaviour. The dynamical plume centreline is deviating from its geometrical centreline in the asymptotic state (Figure 4.12). Here, the dynamical plume centreline is based on the vertical plume velocity and the geometrical centreline is at $x/H = 0$. This centreline deviation is due to the flapping motion of the plume and it meanders along the $y-$direction. The meandering motion of the plume is shown in figure 4.13 (a) and (b) for two different times for when the plume is in the asymptotic state. Cetegen et al. (1998) experimentally studied the oscillatory behaviour of turbulent line plume in an open environment. This kind of dynamic behaviour may affect the steady-state characteristics of line plumes, which precludes a straightforward comparison with the analytical model. Therefore, we introduce a shifting technique for the lateral displacement of dynamical plume centreline (Figure 4.12), originally developed by Hübner (2004) to correct the DNS data to allow more meaningful comparisons between the DNS results and the theoretical models.

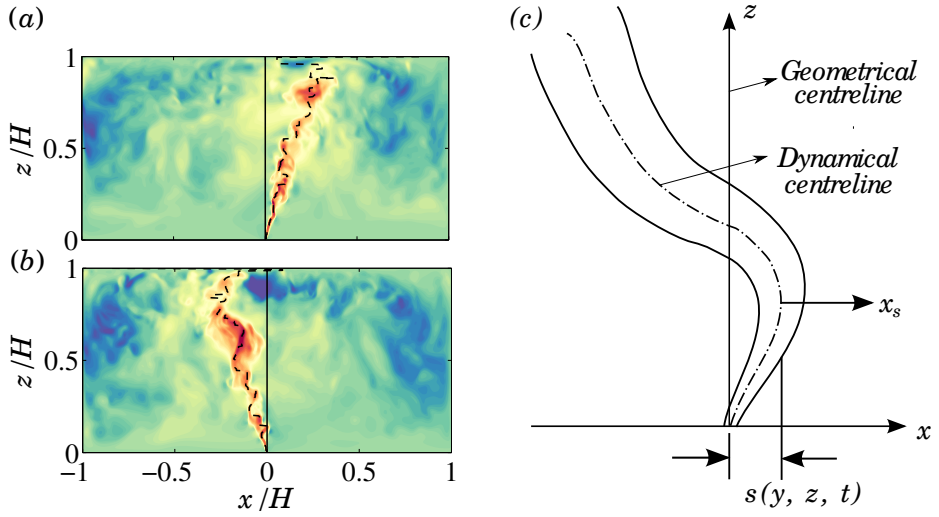

FIGURE 4.12: Flapping motion of confined line plume. (a) Vertical velocity contour for $Re_H = 3600$ and $L/H = 4$ at $t^* \approx 48$ at $y/H = 1$, (b) $y/H = 2$ and (c) schematic diagram of the flapping plume.

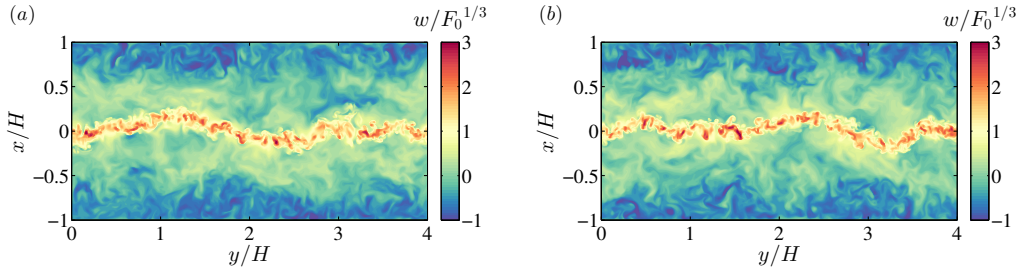

FIGURE 4.13: Contour plots of instantaneous vertical velocity (w) at $z/H = 0.5$ showing the flapping phenomenon of the thermal plumes in the asymptotic state for $Re_H = 3600$ and $L/H = 4.0$; (a) $t^* = 34$; (b) $t^* = 38$.

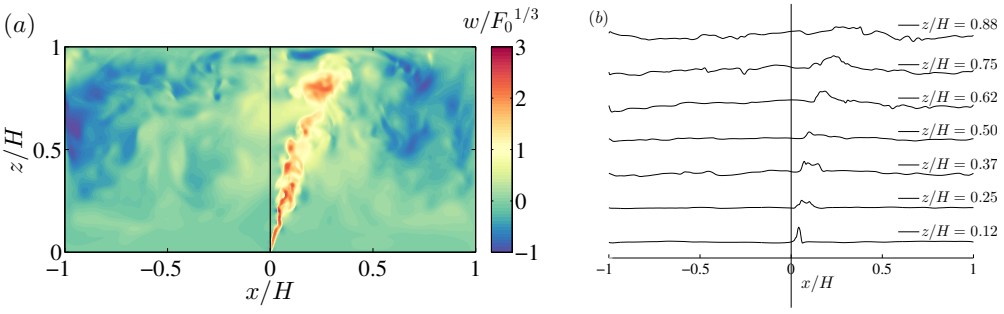

FIGURE 4.14: Contour plot of instantaneous vertical velocity (w) for $Re_H = 3600$ and $L/H = 4.0$ at time $t^* \approx 45$ (a) showing the deflected plume from its geometrical centreline (solid black line) and corresponding horizontal variations of vertical velocity at different z/H locations (b).

The flow properties can thus be defined based on dynamical plume centreline coordinate system

$$(\cdot)_s(x_s, y, z, t) = (\cdot)(x_s + s(y, z, t), y, z, t). \tag{4.32}$$

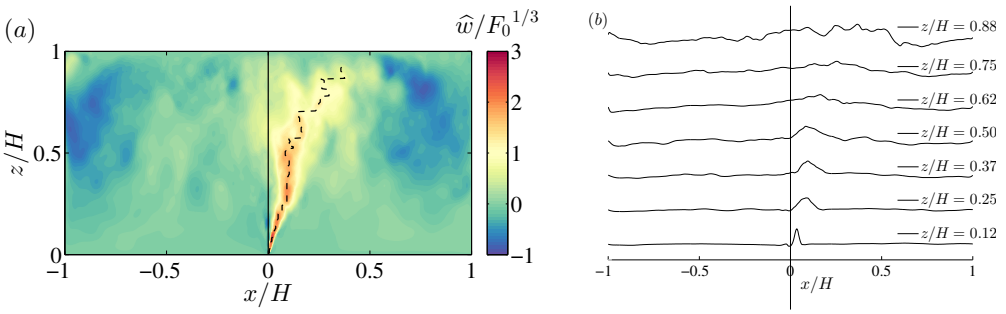

FIGURE 4.15: Contour plot of smoothed vertical velocity ($\widehat{w}$) for $Re_H = 3600$ and $L/H = 4.0$ at time $t^* \approx 45$ (a) showing both geometrical (solid black line) and dynamical centreline (dashed black line) of the plume and corresponding horizontal variations of vertical velocity at different z/H locations (b).

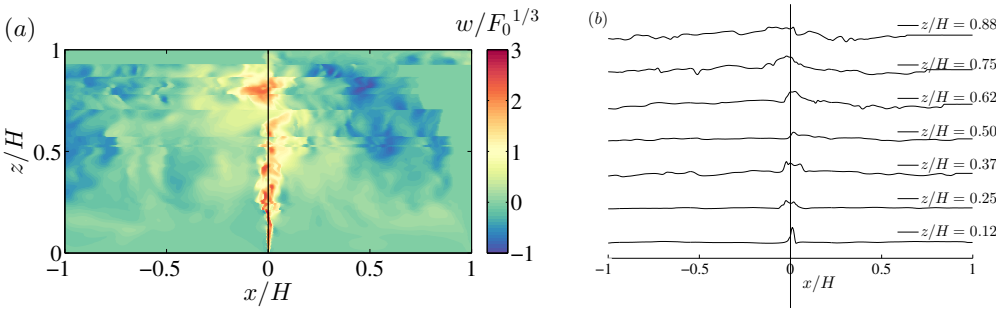

FIGURE 4.16: Contour plot of instantaneous vertical velocity (w) for $Re_H = 3600$ and $L/H = 4.0$ at time $t^* \approx 45$ (a) showing the plume dynamical centreline shifted to its geometrical centreline and corresponding horizontal variations of vertical velocity at different z/H locations (b).

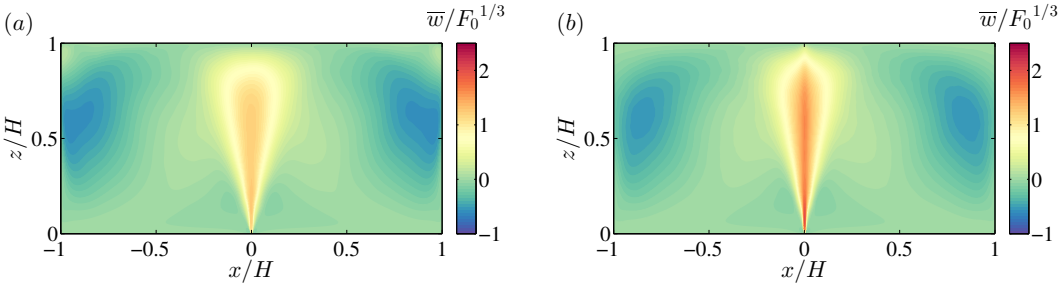

FIGURE 4.17: Contour plots of time averaged vertical velocity ($\overline{w}$) for $Re_H = 3600$ and $L/H = 4.0$ for non-shifted case (a) and dynamical centreline shifted case (b).

Here, x_s is the horizontal coordinate of plume dynamical centreline and s is the deviation of the dynamical centre from the geometrical centre (Figure 4.12 c). The dynamical centreline is chosen as the location of the maximum vertical velocity (w).

To determine the peak location of vertical velocity (w) from the wriggly shape of the vertical velocity profile (figure 4.14 b), a low-pass spectral cut-off filter is used along the $y-$direction with a cut-off wavelength of $\lambda_c = 0.5H$. In other words, Fourier coefficients greater than λ_c are set to zero, and the inverse Fourier transform is taken to obtain the smoothed velocity ($\widehat{w}$). Contour plot of the smoothed vertical velocity and corresponding horizontal profiles of vertical velocity at different z/H locations are shown in figure 4.15. Then, identify the deviation of the dynamical plume centre from the geometrical centre at all vertical locations and shift the dynamical plume centre in Fourier space. Figure 4.16 (a) shows the centreline shifted instantaneous vertical velocity contour and the corresponding horizontal profiles of vertical velocity at different z/H locations are shown in figure 4.16 (b). The $y-$line average and temporal average, which are defined in (4.7) and (4.8) are subsequently calculated. Figure 4.17 (a) and (b) show the contours of temporal averaged vertical velocity for non-shifted and shifted cases, respectively.

4.4.2 Comparison of DNS results and analytical models

The numerical methods used for solving the theoretical models presented in §§4.3.1 (Baines and Turner's model) and 4.3.5 (Barnett's model) are given in appendix B.

Figures 4.18 and 4.19 show the comparison of DNS results for the plume variables (Q, M and F) and the environmental variables (U and Δ_∞), respectively, with theoretical models presented in §§4.3.1 and 4.3.5. Also, figures 4.18 (a, c and e) show the DNS results of non-aligned cases while figures 4.18 (b, d and f) show the results from centreline aligned case which is described in §§4.4.1. The solutions to the theoretical model are obtained by using an entrainment coefficient $\alpha = 0.2$, which was found from the calculations of line plume in a uniform quiescent environment and it is described in appendix A. The values of α reported in literatures for line plumes in a uniform environment vary from 0.12 to 0.2, for example, $\alpha = 0.12$ in Paillat and Kaminski (2014b), $\alpha = 0.162$ in Rouse et al. (1952), $\alpha = 0.16$ in Lee and Emmons (1961) and $\alpha = 0.2$ in Kotsovinos (1975). There is a broad agreement with previously measured entrainment coefficient values for free plumes. This is somewhat surprising given the additional difficulties associated with measuring the velocity of the free plume, which is perhaps reflected in the variation in other parameters between these experiments, especially

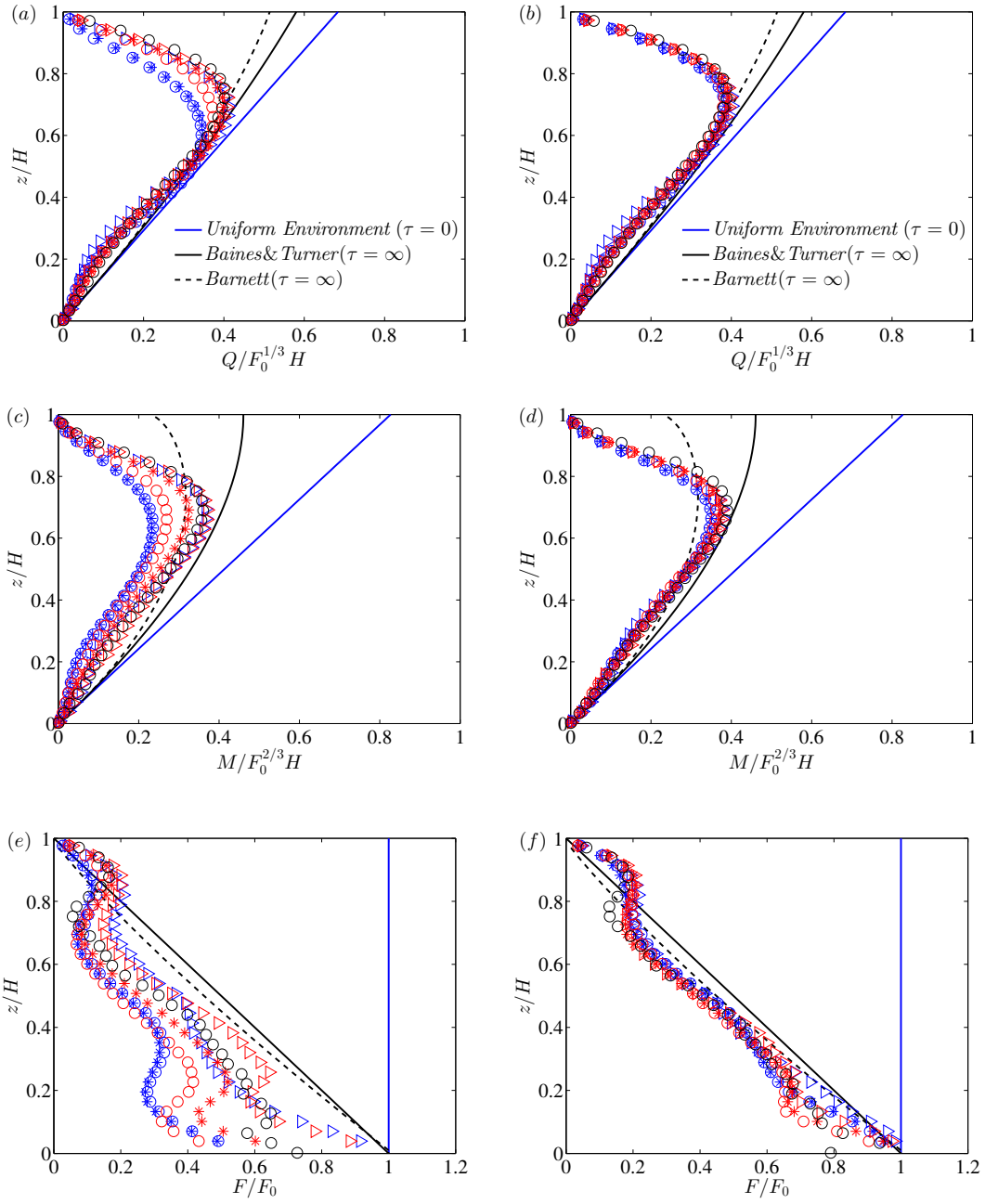

FIGURE 4.18: Comparison of volume flux, momentum flux and buoyancy flux for non-aligned (a, c, e) and aligned (b, d, f) for different Re_H and L/H cases. The solid blue line shows the solution of plume in uniform environment. The solid black line shows Baines and Turner (1969)'s model and dotted black line shows the Barnett (1991)'s model. Blue, red and black symbols are used for Reynolds numbers $Re_H = 1800$, 3600 and 7200, respectively. Triangles, circles, and diamonds represent the $L/H = 1, 2, 4$ cases respectively.

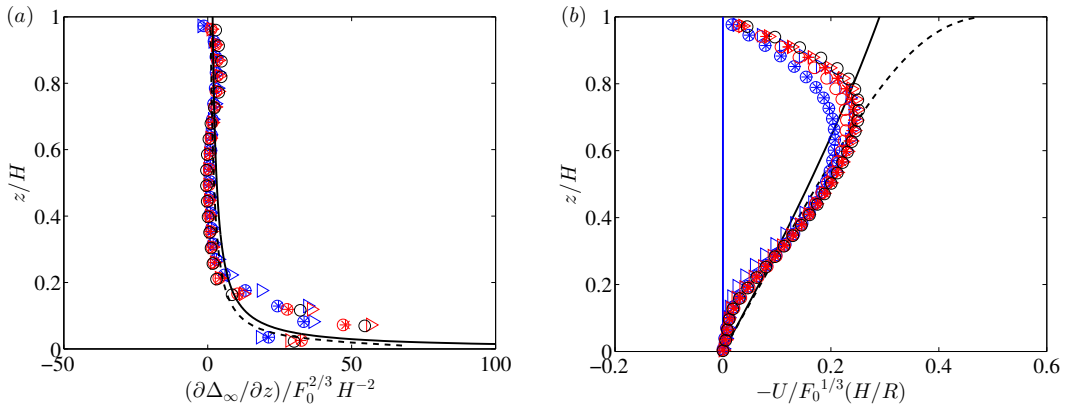

FIGURE 4.19: Comparison of environmental buoyancy gradient (a) and environmental velocity (b) for different Re_H and L/H cases. The solid blue line shows the solution of plume in uniform environment. The solid black line shows Baines and Turner (1969)'s model and dotted black line shows the Barnett (1991)'s model. Blue, red and black symbols are used for Reynolds numbers $Re_H = 1800$, 3600 and 7200, respectively. Triangles, circles, and diamonds represent the $L/H = 1, 2, 4$ cases respectively.

maximum mean velocity used in the calculation of α. In the present study, the value of $\alpha = 0.2$ is set to a fixed value and used for all calculations related to free plumes. The results are for Reynolds numbers, 1800, 3600 and 7200 and the three different plume lengths ($L/H = 1$, 2 and 4) for Reynolds numbers 1800 and 3600 and $L/H = 2$ for $Re_H = 7200$. To compute the integrals over the $x-$ directions of the plume, we fitted a Gaussian curve to the vertical velocity profile at each z/H locations based on the maximum vertical velocity w_m and width b_w (width at which the vertical velocity has fallen to $1/e$ of its central value, where e is a mathematical constant that is the base of natural logarithm) and we defined the integration limit $\pm x_\infty$ such that $\overline{w}(\pm x_\infty, z) = w_m(z)/100$ from the fitted Gaussian curve, which ensures that the vertical environmental velocity is small relative to that of the plume.

Figures 4.18(a) and (b) show the non-aligned and aligned (i.e., corrected for flapping) plume volume flux (Q) profiles, respectively. The symbols are same as in figure 4.11. The solid black line represents the analytical model of Baines and Turner described in §§4.3.1. The dotted line in figures 4.18 and 4.19 represented the asymptotic solution of the Barnett's model and the solid blue line shows the solution for the line plume in a uniform environment. There are only marginal differences in the volume flux profiles between non-aligned and aligned cases. The cases tend to exhibit improved collapse to a single curve; however, some dependence of the volume flux on plume length clearly remains. The Baines and Turner (1969)

model predicts well the plume volume fluxes from $z/H = 0$ to $z/H \approx 0.7$, also the Barnett (1991) model improves the prediction of the volume fluxes marginally.

The Baines and Turner (1969) model shows good agreement with the plume momentum flux (M) profiles for aligned cases (figures 4.18 d). Observe that the DNS results in figure 4.18(c) have not collapsed to a single curve due to the flapping motion of the plume which occurs in the asymptotic state, and this problem is alleviated in figure 4.18(d) after correcting for the flapping motion. It can be seen that the mean quantities of volume (4.18 a), momentum (4.18 c) and buoyancy flux (4.18 e) have some dependency on Reynolds numbers and plume lengths. In the case of low Reynolds number, the DNS results are away from the analytical model and for the case of high Reynolds number the results are closer to the model for all non-aligned cases.

Figures 4.18(e) and (f) show the buoyancy flux profiles for non-aligned and aligned cases. It is clearly seen that the non-aligned DNS results are scattered about the model predictions but aligned buoyancy flux profiles good agreement with all the model predictions.

Non-aligned profiles are used for environmental variables. The environmental buoyancy gradient $\partial\Delta_\infty/\partial z = -g\,\beta\,\partial\overline{T}_\infty/\partial z$ variation with respect to height is plotted in figure 4.19(a). Similar to the environmental buoyancy, the environmental temperature T_∞ is defined as the the horizontally averaged temperature from $x/H = \pm 0.25$ to $x/H = \pm 0.99$. The DNS results show reasonable agreement with the all the models in the region between $z/H = 0.2$ to $z/H = 0.8$. Also, the environmental velocity U, here taken to be the horizontally averaged vertical velocity from $x/H = \pm 0.25$ to $x/H = \pm 0.99$ and shown in figure 4.19(b). The Baines and Turner (1969) and Barnett (1991) models both yield fairly satisfactory profiles.

4.5 Chapter summary

The development and the asymptotic behaviour of a thermal line plume originating from a local line heat source is analysed using direct numerical simulation. The Reynolds number of the confined plume based on the box height and buoyant velocity scale of the fluid are chosen to be 1800, 3600 and 7200, and with plume lengths, $L/H = 1$, 2 and 4 for aspect ratio, $R/H = 1$. The fluid mechanics of the

filling box process is divided into two states. First, the evolution of the buoyant fluid toward the asymptotic state. In this state, the transient behaviour have been observed for the thermal plumes. The second stage is when the plume reaches the large-time asymptotic state. In the asymptotic state, we observed a flapping and meandering of the plume with a counter-rotating vortex pair on either side of the plume. The plume lengths $L/H = 2$ and 4 are found to be sensitive to the flapping behaviour of the line plumes. These phenomena precludes a straight forward comparison with the Baines and Turner (1969)'s and Barnett (1991)'s analytical models. A centreline alignment method is used to alleviate the effect of flapping and meandering behaviours of the plume. We have compared all the analytical models with present DNS results. All the comparisons are made with an entrainment constant α equal to 0.2. The Baines and Turner (1969)'s model showed good agreement with the centreline aligned DNS profiles of plume volume, momentum and buoyancy fluxes in the asymptotic state. The Barnett (1991)'s model predicted almost similar profiles of the Baines and Turner (1969)'s model in the asymptotic state for aspect ratio, $R/H = 1$. The environmental parameters are also well predicted by the Baines and Turner (1969)'s model in the asymptotic state.

Chapter 5

Development of horizontal outflow from impinging line plumes in large aspect ratio boxes

In this chapter, we investigate the propagation of horizontal front from a thermal line plume after impinging onto the top wall in uniform quiescent and stratified environment. In the following, we first describe the theoretical model for the horizontal outflow. This is followed by the comparison of present DNS results with model.

5.1 Theoretical model for horizontal front propagation

Kaye and Hunt (2007) developed a model for the bulk properties of the horizontal outflow from a point plume. Here, we extend this model for the horizontal outflow from a line plume.

Figure 5.1 shows a schematic of the horizontal outflow along the top wall from a turbulent line plume. Kaye and Hunt (2007) decomposed the horizontal outflow from a point source into different zones, namely impinging, jet-like and gravity current flow zones. Similarly, we consider three different zones for the outflow from a line plume and these zones are shown in figure 5.1 (impinging zone I, jet-like zone II and gravity current flow zone III). Immediately after the impingement

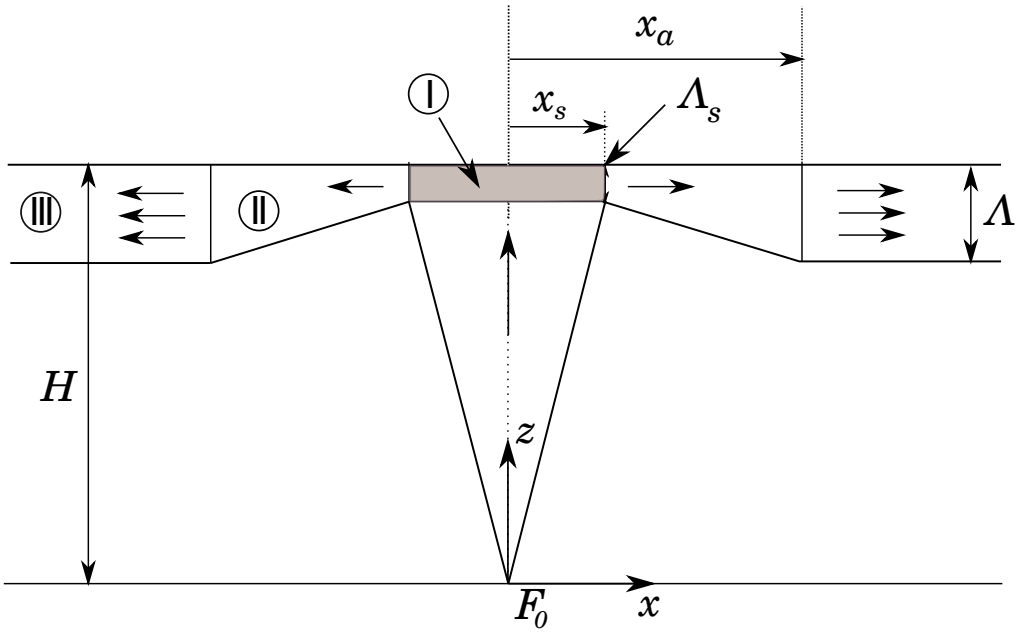

FIGURE 5.1: Schematic diagram of a horizontal outflow from a constant buoyancy flux turbulent plume from a line source (similar to Kaye and Hunt (2007) model for point source). The different regions are marked as (I) impinging zone, (II) jet-like flow zone and (III) gravity current flow zone.

of plume on the top wall, the fluid behave as a horizontal wall jet for a particular length $x_a - x_s$. The initial depth of horizontal wall jet is denoted by Λ_s. In the jet-like zone, a linear increase in current depth with horizontal distance was observed. The length x_a is considered to be the flow development length for a constant depth gravity current flow. The depth of current in the gravity current zone is denoted by Λ.

Chen (1980) obtained an expression for the position of the front of a planar gravity current with time (t) by balancing the buoyancy force per unit length ($\rho g' \Lambda^2$) and inertial force per unit length ($\rho x^2 \Lambda / t^2$) in the inertial regime, where g' is the buoyancy of the fluid layer. Also, the continuous source discharge $Q_s t$ is similar to $x\Lambda$ and the final expression for the position of the front of gravity current is

$$x = c_i \, {F_s}^{1/3} t, \tag{5.1}$$

where c_i is a constant in the inertial regime and F_s is the source buoyancy flux of the gravity current.

The other main parameters involved in this study are the volume flux and the momentum flux which can be expressed in terms of x, Λ and F_s. Note that in the

unstratified environment, the line plume and the gravity current source buoyancy fluxes are half of the plume source buoyancy flux ($F_s = F_0/2 =$ constant). The volume flux (Q_h) and momentum flux (M_h) in the gravity current regime can be expressed as $Q_h \sim \Lambda U_h$ and $M_h \sim \Lambda U_h^2$, where U_h is the horizontal velocity of the gravity current. The value of U_h can be estimated by differentiating (5.1)

$$U_h = c_i {F_s}^{1/3} \tag{5.2}$$

and now

$$Q_h = c_i \Lambda {F_s}^{1/3}, \text{ and, } M_h = c_i^2 \Lambda {F_s}^{2/3}. \tag{5.3}$$

The source of horizontal current along the the top wall is from the outflow of line plume at $z/H = 1.0$. Therefore, we can define the outflow conditions of the plume for the plume width (x_p), volume flux (Q_p) and momentum flux (M_p) as

$$x_p = b(z/H = 1.0) = c_1 H, \tag{5.4}$$

$$Q_p = \frac{Q}{2}(z/H = 1.0) = c_2 {F_s}^{1/3} H, \tag{5.5}$$

$$M_p = \frac{M}{2}(z/H = 1.0) = c_3 {F_s}^{2/3} H. \tag{5.6}$$

The values of the constants c_1, c_2 and c_3 depends on the entrainment coefficient α and the assumptions of the plume vertical velocity profiles (top-hat or Gaussian). The outflow source horizontal distance x_s is identical to x_p. At the impinging zone shown in figure 5.1, we can apply volume conservation relation

$$Q_s = \Lambda_s U_h = c_2 {F_s}^{1/3} H = Q_p. \tag{5.7}$$

When the plume impinges on the top wall, the vertical momentum flux reduces to zero and there will be an energy loss due to the change in flow direction from vertical to horizontal. Therefore, the outflow source momentum flux can be expressed as

$$M_s = \Lambda_s U_h^2 \sim c_3 {F_s}^{2/3} H \sim M_p. \tag{5.8}$$

Hence

$$M_s = \Lambda_s U_h^2 = \gamma M_p = \gamma c_3 {F_s}^{2/3} H \tag{5.9}$$

where γ is a constant. The source depth Λ_s can be calculated from (5.7) and (5.9), which is

$$\Lambda_s = \frac{Q_s^2}{M_s} = \frac{c_2^2}{c_3\,\gamma} H, \tag{5.10}$$

which implies that the initial outflow depth increases as the energy loss due to the change in flow direction increases (i.e. γ decreases). In the jet-like zone (II), the horizontal momentum flux (M_h) is assumed to be a constant (similar to a constant momentum flux wall jet), i.e.

$$M_h = M_s = \gamma c_3 {F_s}^{2/3} H = \text{constant} \tag{5.11}$$

and the depth expected to increase linearly with respect to horizontal distance x, i.e.

$$\Lambda = \Lambda_s + \frac{\mathrm{d}\Lambda}{\mathrm{d}x}(x - x_s), \tag{5.12}$$

where $\mathrm{d}\Lambda/\mathrm{d}x$ is an unknown constant. We can now express the horizontal velocity U_h and volume flux Q_h as

$$U_h = \sqrt{\frac{M_s}{\Lambda}} = \frac{\gamma^{1/2}\, c_3^{1/2} {F_s}^{1/3}\, H^{1/2}}{\sqrt{\Lambda}} \tag{5.13}$$

and

$$Q_h = \Lambda\, U_h = \gamma^{1/2}\, c_3^{1/2} {F_s}^{1/3}\, H^{1/2}\, \Lambda^{1/2}. \tag{5.14}$$

For very large values of x with in the jet-like zone ((II)), the outflow depth Λ can be approximated as $\Lambda \approx (\mathrm{d}\Lambda/\mathrm{d}x)x$. Thus, we can estimate the movement of the planar horizontal front with time in the jet-like zone by using (5.13) as

$$\frac{\mathrm{d}x}{\mathrm{d}t} \approx \sqrt{\frac{\gamma\, c_3}{\mathrm{d}\Lambda/\mathrm{d}x}}\, \frac{{F_s}^{1/3}\, H^{1/2}}{x^{1/2}}. \tag{5.15}$$

Integrating (5.15) gives

$$x \approx \left(\frac{\gamma\, c_3}{\mathrm{d}\Lambda/\mathrm{d}x}\right)^{1/3} {F_s}^{2/9} H^{1/3} t^{2/3}. \tag{5.16}$$

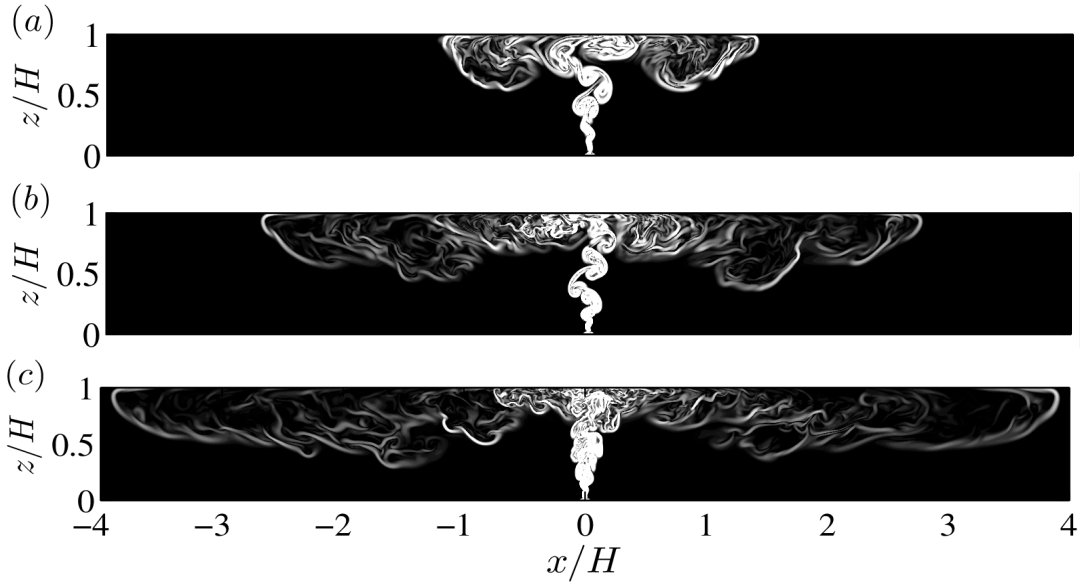

FIGURE 5.2: Magnitude of the temperature gradient (at $y/H = 0.5$) for $Re_H = 3600$ and $R/H = 4$ at times $t_n = 1.42$ (a), 3.58 (b) and 5.76 (c).

We can express the non-dimensional planar horizontal front position in the jet-like zone, from (5.16) as

$$\phi = c_j \, {t_n}^{2/3}, \tag{5.17}$$

where $c_j = (\gamma \, c_3/(\mathrm{d}\Lambda/\mathrm{d}x))^{1/3}$ is a constant, $\phi = x/H$, is dimensionless horizontal distance and $t_n = ({F_s}^{1/3} \, t/H)$, is dimensionless time. Similarly, in the far-field gravity current zone, the non-dimensional planar horizontal front position, from (5.1), as

$$\phi = c_i \, t_n. \tag{5.18}$$

In the following section, we discuss the DNS of horizontal front propagation in order to find the value of constants in (5.17) and (5.18).

5.2 DNS of horizontal front propagation and comparison with model

5.2.1 Horizontal front position

We conducted a set of DNS with different aspect ratios (R/H) of the box to validate the scaling laws and establish the constants in the theoretical model for

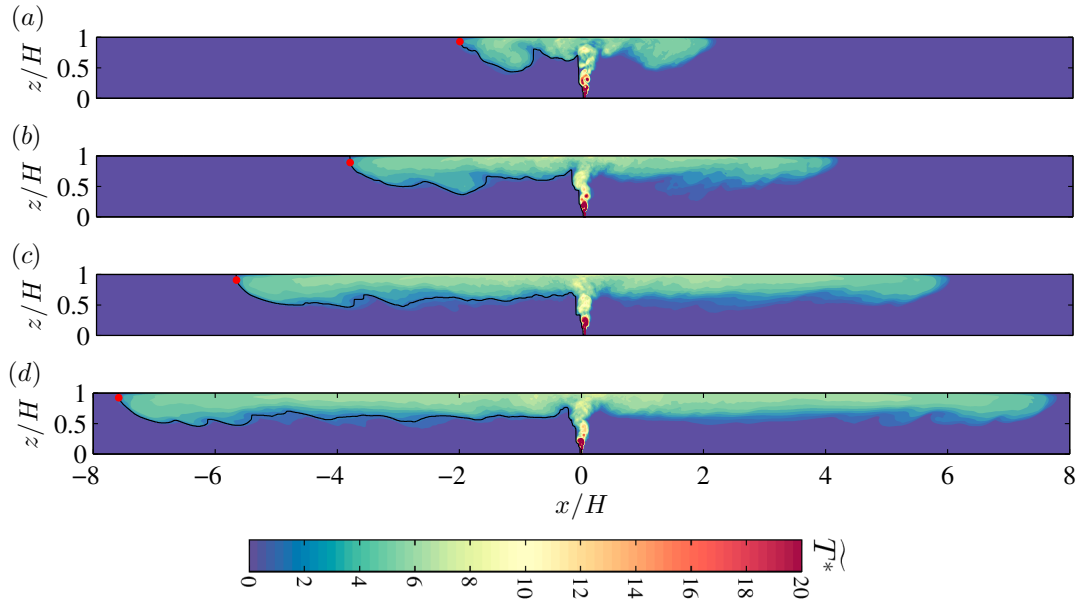

FIGURE 5.3: Contour plots of the line-averaged non-dimensionalised temperature ($\widetilde{T^*}$) for aspect ratio (R/H) = 8.0, showing the propagation of horizontal front. At times $t^* = 3.35\,(a)$, $6.55\,(b)$, $9.88\,(c)$, $13.17\,(d)$. The red dots indicates the location of horizontal front front as a function of time. A threshold of 1.2 is chosen for non-dimensionalised temperature to define the interface (solid black lines).

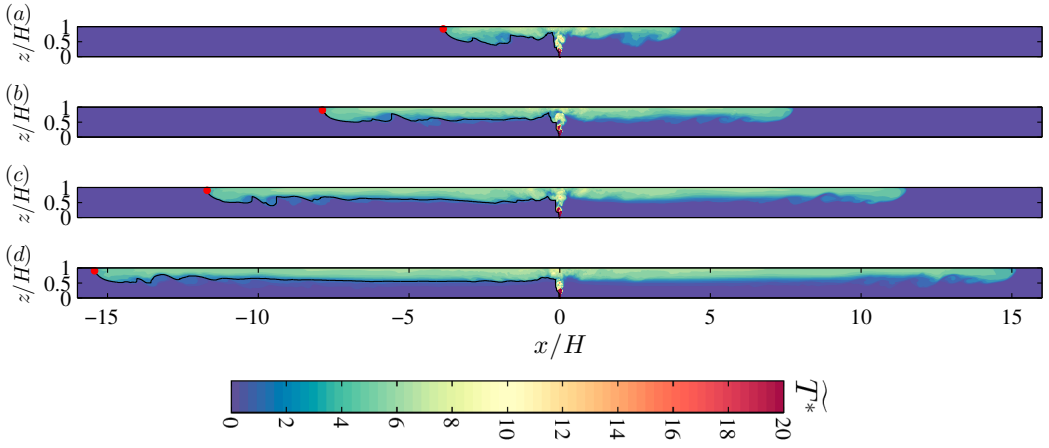

FIGURE 5.4: Contour plots of the line-averaged non-dimensionalised temperature ($\widetilde{T^*}$) for aspect ratio (R/H) = 16.0, showing the propagation of horizontal front. At times $t^* = 6.43\,(a)$, $12.9\,(b)$, $19.43\,(c)$, $26.38\,(d)$. The red dots indicates the location of horizontal front front as a function of time. A threshold of 1.2 is chosen for non-dimensionalised temperature to define the interface (solid black lines).

the position of planar horizontal front with time. In this study, we have chosen a Reynolds number, $Re_H = 3600$ with five different aspect ratios $1, 2, 4, 8$ and 16 (table 4.1). Figure 5.2 shows the contour plots for the magnitude of temperature

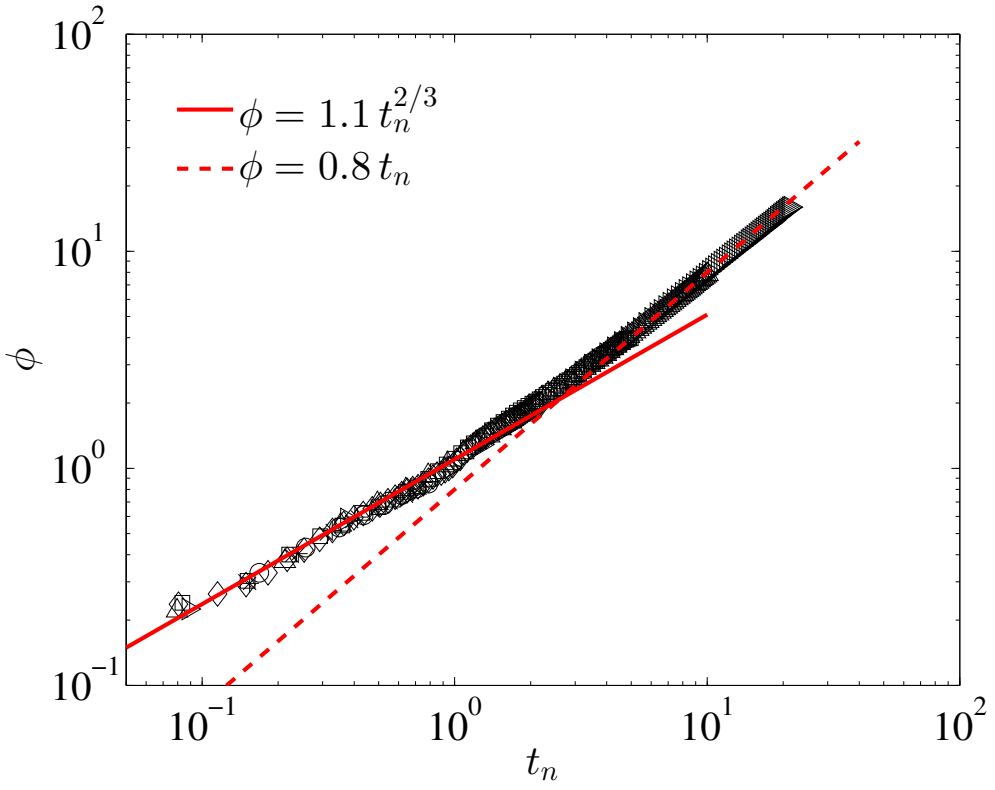

FIGURE 5.5: Non-dimensional planar horizontal front position ϕ against time t_n for five different aspect ratio boxes $(1, 2, 4, 8$ and $16)$ and $Re_H = 3600$. The symbols used for different cases are not distinguishable due to the collapse of the DNS data onto a single line. The solid red line is given by $\phi = 1.1\, t_n^{2/3}$, indicates the jet-like zone. The dashed red line is given by $\phi = 0.8\, t_n$.

gradient at different times to visualise horizontal front propagation. We measured the temporal evolution of the planar horizontal front for both sides of the line plume after the plume impinges on the top wall. Here, the horizontal front position is defined as the maximum horizontal extent from a line-averaged temperature interface of the planar current at a particular time. In order to identify the most adequate interface position, several threshold values are tested. A threshold of 1.2 is chosen for temperature because it closely corresponds to a visually observed interface position. Figure 5.3 and 5.4 show the contour plots of line averaged non-dimensionalised temperature $(\widetilde{T^*})$ to identify the position of the horizontal front propagation as a function of time for aspect ratio (R/H), 8 and 16, respectively. The solid black lines in figures 5.3 and 5.4 correspond to the interface position for the front propagation and the red dots indicate the maximum horizontal extent, which is taken as the front position at a particular time. The movement of the front position is measured with a non-dimensional time step of 4×10^{-3}. The time $t_n = 0.0$ is at the moment when the plume first touches the top wall, which is

taken as the reference time.

Figure 5.5 shows the non-dimensional planar horizontal front position (mean of the left and right side horizontal front position) with respect to the time for different aspect ratio boxes. From the analytical predictions described in §5.1, initially, we expect a jet-like zone with scaling $\phi \sim t_n^{2/3}$ (5.17) and then a gravity current zone with scaling $\phi \sim t_n$ (5.18). These scalings can be clearly seen in figure 5.5. The solid red line indicates $\phi = 1.1\, t_n^{2/3}$ for the initial jet-like region and dashed red line indicates $\phi = 0.8\, t_n$ for the gravity current region. From our DNS study, we obtained the value of the constants in (5.17) and (5.18), which is $c_j = 1.1$ and $c_i = 0.8$. The intersection of red solid and dashed line show the transition point from jet-like zone to gravity current zone, which is $\phi \approx 2.2$. This transition point is much higher than in the case of outflow from a axisymmetric constant buoyancy flux from a point source (Kaye and Hunt (2007)), which is $\phi = 0.66$.

5.2.2 Mean velocity and temperature profiles

The mean contours of non-dimensionalised temperature ($\overline{T}^* = g\beta H\overline{T}/F_s^{2/3}$), horizontal velocity ($\overline{u}/F_s^{1/3}$) and vertical velocity ($\overline{w}/F_s^{1/3}$) in the right-hand side of the box are shown in figures 5.6 (a), (b) and (c), respectively. Henceforth, the half of the initial buoyancy flux, $F_s = F_0/2$ is used for normalising the values of temperature and velocity. Due to the excessive computational cost (approximately 16520 CPU hours), the mean profiles are obtained by averaging spatially along the $y-$ direction as well as averaging across the time instances during which the horizontal front travels from $x/H \approx \pm 10$ till $x/H \approx \pm 16$ (approximately 120 data sample in time). In this scenario, the properties of the horizontal front will lost between $x/H \approx \pm 10$ and $x/H \approx \pm 16$. However, we will get a nearly smooth region upto $x/H \approx \pm 10$ for analysing the mean quantities for the horizontal outflow from the plume. The mean quantities are smooth up to $x/H \approx \pm 10$, which is only used for analyse the flow properties.

The mean profiles of temperature ($\overline{T}$) normalised by $F_s^{2/3}/g\beta H\overline{T}$ and maximum temperature $\overline{T}_m$ at different x/H locations are plotted in figures 5.7 (a) and (b), respectively. The maximum temperature is observed near the line plume, i.e. $x/H = 1.0$ and these profiles show good collapse when the mean temperature is normalised by the maximum temperature of each profile at different x/H locations.

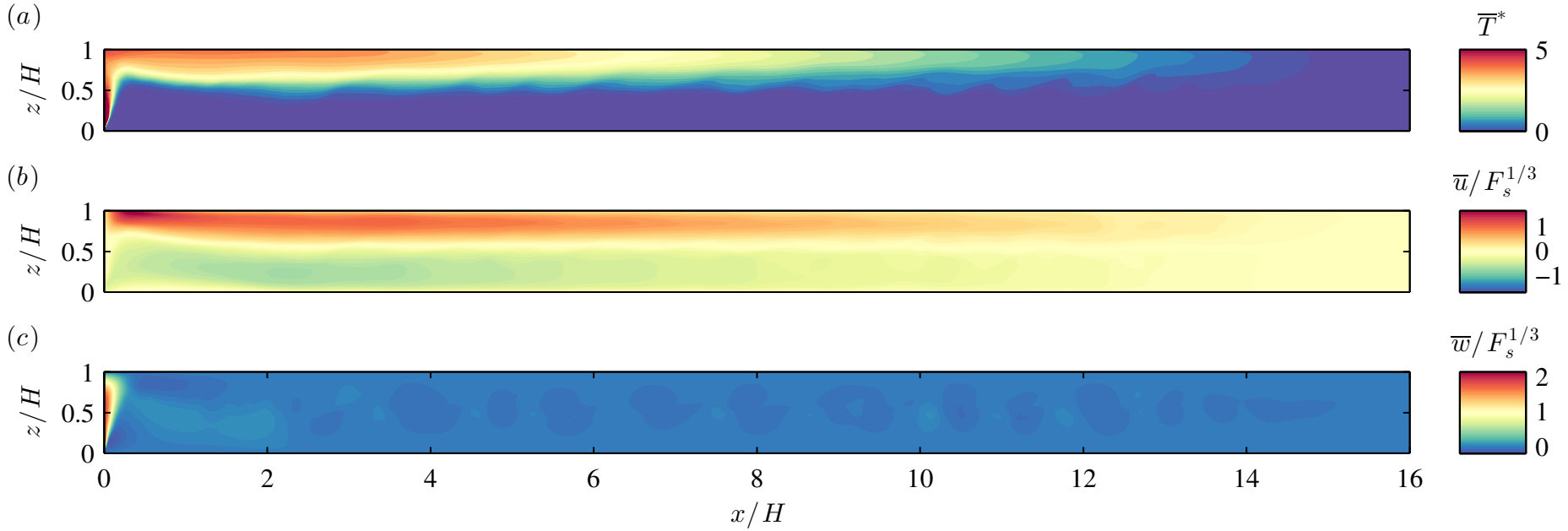

FIGURE 5.6: Mean contour plots of (a) non-dimensionalised temperature ($\overline{T}^*$), (b) horizontal velocity ($\overline{u}/F_s^{1/3}$) and (c) vertical velocity ($\overline{w}/F_s^{1/3}$) for $R/H = 16$ case. Due to symmetry, only the right-hand half of the box is shown here. The mean profiles are obtained by averaging spatially along the $y-$ direction as well as averaging across the time instances during which the horizontal front travels from $x/H \approx \pm 10$ till $x/H \approx \pm 16$ (approximately 120 data sample in time).

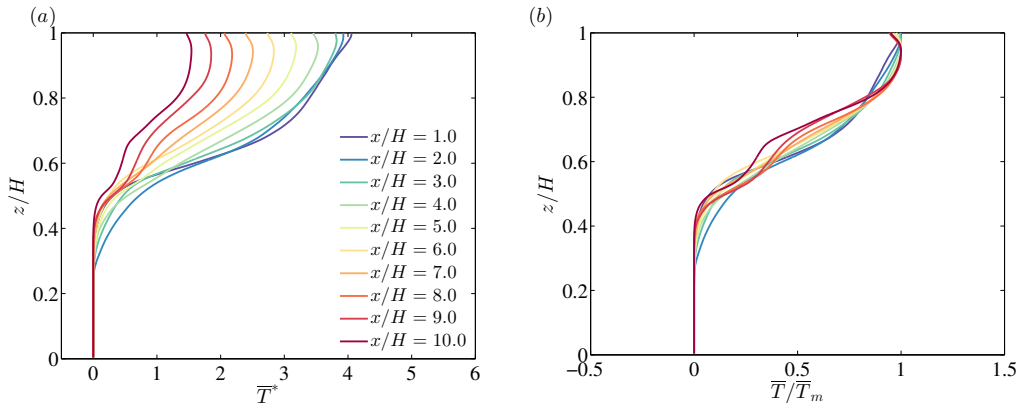

FIGURE 5.7: Mean profiles of temperature at different x/H locations ($1.0 \leq x/H \leq 10.0$) for the $R/H = 16$ case. (a) The temperature is normalised by $F_s^{2/3}/(g\beta H)$ and (b) normalised by maximum temperature $\overline{T}_m$.

These observations indicate that there is similarity of the mean horizontal velocity and temperature profiles in the region $3.0 \leq x/H \leq 10$.

5.2.3 Longitudinal dependence of integral quantities

One of the main focus of this study is the behaviour of integral quantities such as the mean volume flux, momentum flux and the mean buoyancy flux and their scalings for different regimes in the horizontal outflow from a line plume. Figure 5.8 shows the longitudinal dependence of these quantities for $R/H = 16$ case. Here, the mean horizontal volume flux (Q_h), mean horizontal momentum flux (M_h) and mean horizontal buoyancy flux (F_h) are defined respectively by

$$Q_h = \int_0^{z_u} \overline{u}\,\mathrm{d}z, \quad M_h = \int_0^{z_u} \overline{u}^2\,\mathrm{d}z, \quad F_h = \int_0^{z_u} g\beta\,(\overline{T} - \overline{T}_{int})\,\overline{u}\,\mathrm{d}z, \tag{5.19}$$

here the lower integration limit starts at $z = H$ and set as 0 and the upper integration limit z_u is defined as $H - z_{int}$, where z_{int} is the interface location in $z-$ direction. We used the method described in §5.2.1 to obtain the interface location for horizontal gravity current. The ambient temperature $\overline{T}_{int}$ is defined as the temperature at the interface location.

The grey lines in figure 5.8 (a), (b) and (c) corresponds to the individual members of the ensemble for the normalised horizontal volume flux, momentum flux and buoyancy flux, respectively. These data are plotted in the time period during which the horizontal front travels from $x/H \approx \pm 10$ till $x/H \approx \pm 16$. Each

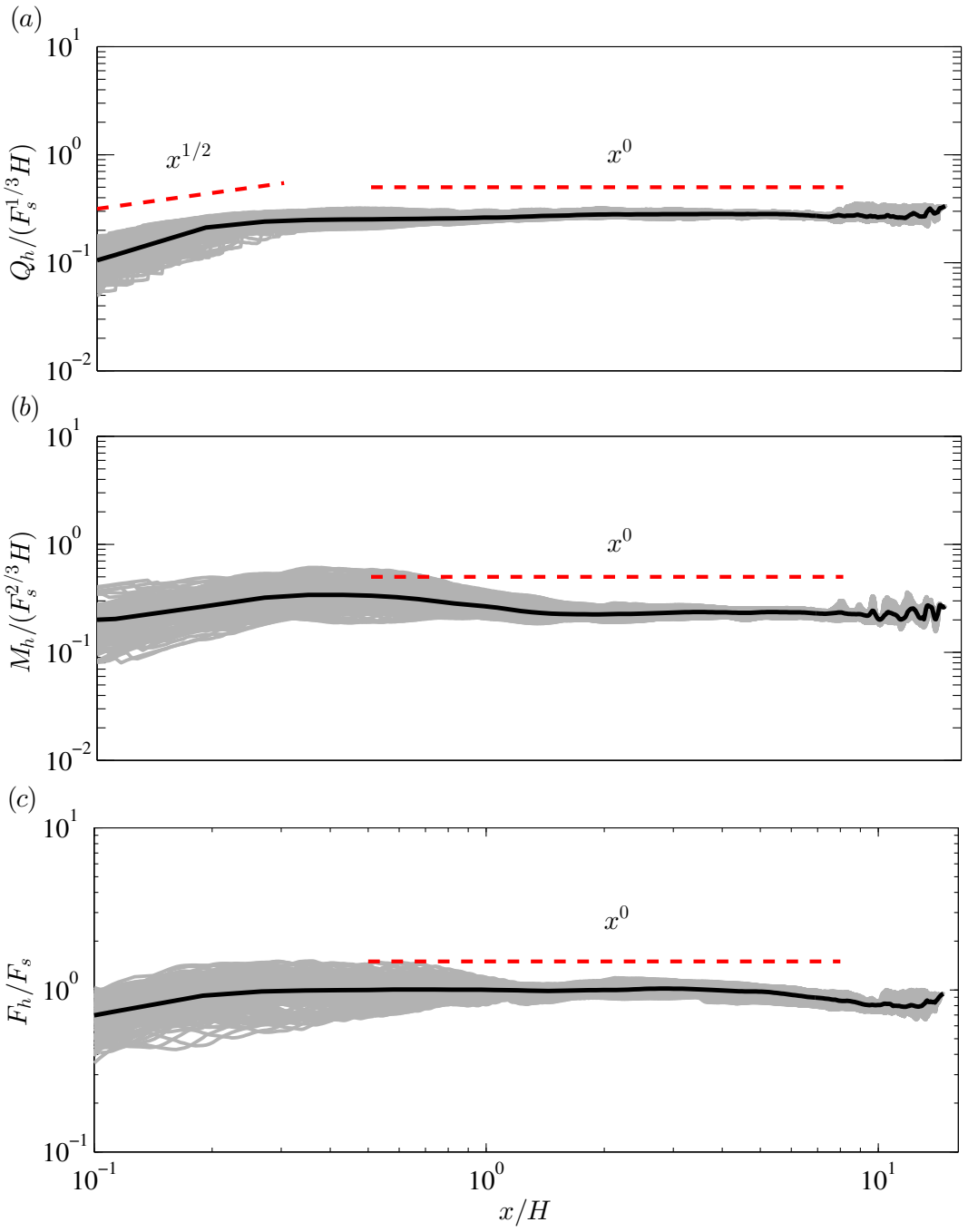

FIGURE 5.8: (a) Dimensionless horizontal volume flux, (b) dimensionless horizontal momentum flux and (c) dimensionless horizontal buoyancy flux, corresponding to individual members of the ensemble (grey lines) and their ensemble average (thick black line) for $R/H = 16$ case. The grey lines are plotted when the horizontal front travels from $x/H \approx \pm 10$ till $x/H \approx \pm 16$.

ensemble comprising 120 data samples in time and the thick black line indicates the ensemble average.

The theoretical model for horizontal gravity current is described in §§5.1. We

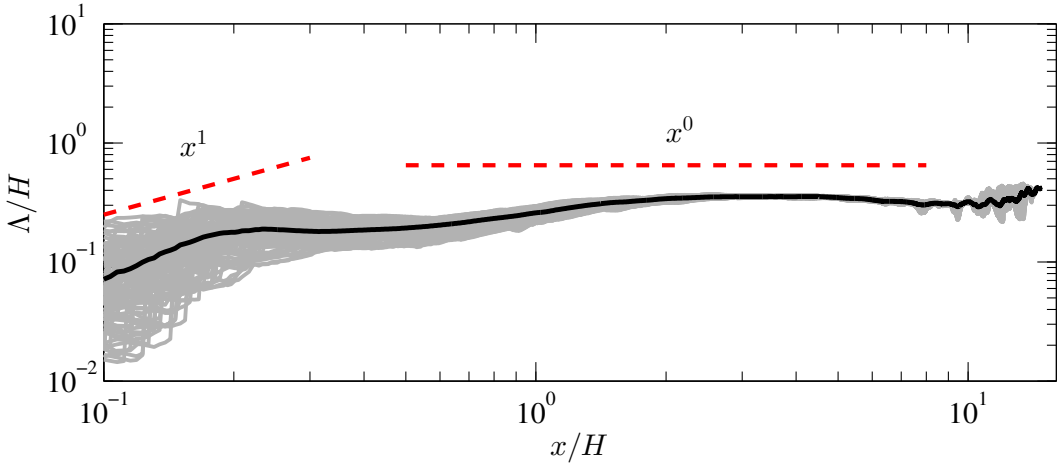

FIGURE 5.9: Space evolution of the non-dimensional horizontal current height Λ/H. The grey lines corresponds to the individual members of the ensemble and the black line corresponds to their ensemble average.

mainly divided the horizontal outflow from a turbulent line plume into two different zones, namely jet-like and gravity current flow zones. The jet-like zone is near the plume impinging region and the gravity current zone is far from the plume (see figure 5.1).

In the jet like zone, the horizontal front position x is proportional to $t^{2/3}$. So, the horizontal velocity $U_h (= \mathrm{d}x/\mathrm{d}t)$ is proportional to $x^{-1/2}$. Also, the horizontal outflow thickness Λ as a function of x in the jet-like region. Therefore, the horizontal outflow volume flux Q_h $(= U_h \Lambda)$ is proportional to $x^{1/2}$. But for the gravity current region, the horizontal front position x proportional to t and the horizontal velocity U_h is constant with respect to x. Therefore, the volume flux in the gravity current region is also constant, under the assumption of constant thickness of outflow in that region.

Similarly, using the same scalings for U_h and Λ, the horizontal momentum flux M_h $(= U_h^2 \Lambda)$ is remain constant in both jet-like and gravity current regions. The horizontal buoyancy flux F_h is assumed to be constant with respect to x in the entire region of the horizontal outflow.

The horizontal outflow thickness obtained from the volume and momentum flux as $\Lambda = Q_h^2/M_h$ is plotted in figure 5.9. The expected scalings for all the bulk quantities are shown in figure 5.8 with dashed red lines. The DNS results show good agreement for the predicted scalings for the bulk quantities in the gravity

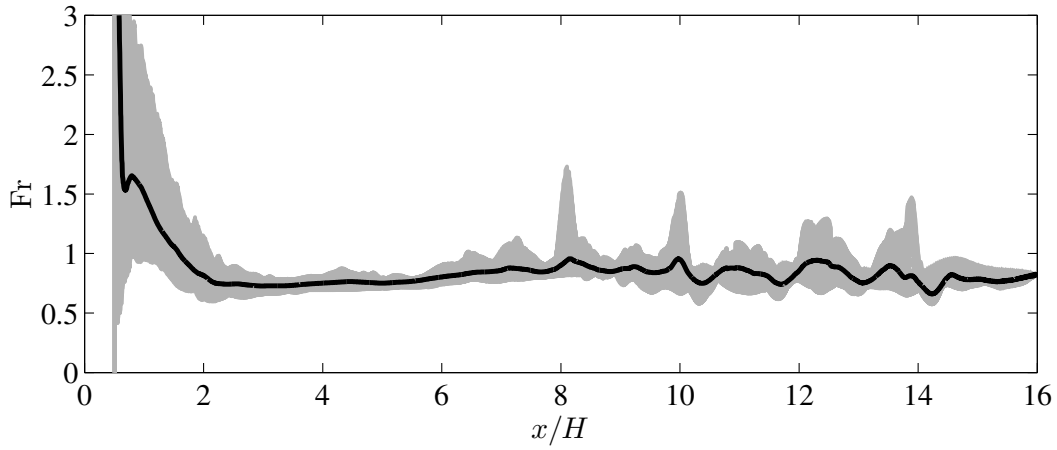

FIGURE 5.10: Space evolution of the Froude number Fr. The grey lines corresponds to the individual members of the ensemble and the black line corresponds to their ensemble average.

region and moderate agreement is observed in the jet-like regimes of the horizontal outflow from a line plume.

The Froude number is an important dimensionless parameter measuring the ratio of the inertia force to the gravitational force on a element of fluid for Boussinesq gravity current. The longitudinal variation of Froude number (Fr) can be expressed in terms of mean bulk quantities

$$\mathrm{Fr} = \frac{U_h}{\sqrt{B_h \Lambda}}, \tag{5.20}$$

where $B_h = F_h/Q_h$ is the mean bulk buoyancy. Figure 5.10 presents longitudinal variation of the Froude number Fr for aspect ratio (R/H) box. An evident distinction between jet-like and gravity current regions is observed in this plot. At the beginning of the horizontal flow, the Froude number is observed to be high. Kaye and Hunt (2007) theoretically argued that, the momentum flux is dominated close to the impingement zone created by a round plume and therefore the value of Froude number expected to be greater than unity. Later, the value of Froude number starts decrease in the jet-like regime and became constant in the gravity current regime where the inertia and buoyancy forces are balance each other.

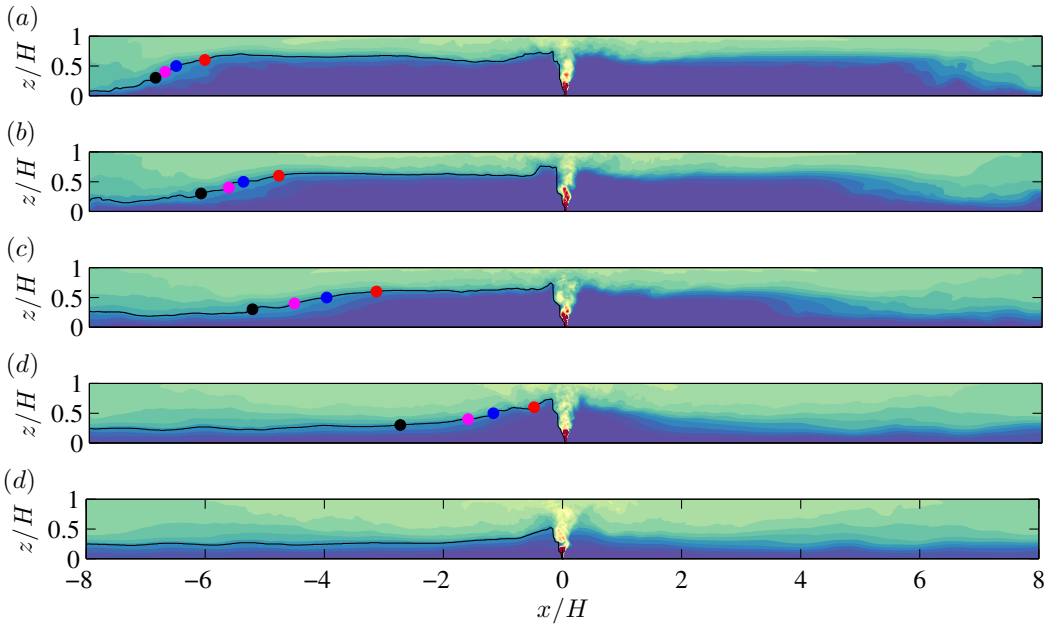

FIGURE 5.11: Contour plots of the line-averaged non-dimensionalised temperature ($\widetilde{T^*}$) for aspect ratio (R/H) = 8.0, showing the filling of the box from both sideways. At times $t^* = 17.66\,(a)$, $19.82\,(b)$, $22.04\,(c)$, $26.43\,(d)$, $28.55\,(e)$. The black, magenta, blue and red dots indicate the location of return front at $z/H = 0.3$, 0.4, 0.5 and 0.6, respectively. A threshold of 1.2 is chosen for non-dimensionalised temperature to define the interface (solid black lines).

5.2.4 Counter-flowing gravity current front position in a uniform environment

Once the horizontal outflow along the top wall reaches the side walls, it begins to flow downwards and then move in the opposite direction as a counter-flowing gravity current. The horizontal propagation of counter-flowing gravity current like flow is illustrated in figure 5.11. The contour plots in figure 5.11 shows the line averaged non-dimensionalised temperature ($\widetilde{T}^*$) at different times for aspect ratio ($R/H = 8.0$) box. We selected a threshold value of 1.2 for the non-dimensionalised temperature same as that for the previous horizontal front propagation to define the interface location, which is marked by solid black lines in figure 5.11. The black, magenta, blue and red dots indicates the location of counter-flowing gravity current front position at $z/H = 0.3$, 0.4, 0.5 and 0.6, respectively.

Figure 5.12 shows the positions of counter-flowing gravity current front as function of time in the uniform environment for aspect ratio (AR) = 8.0. Here, the front propagation time t_b is based on a reference time t_{ref}, i.e. $t_b = t - t_{ref}$. The reference time t_{ref} is calculated when the buoyant fluid reaches the bottom wall.

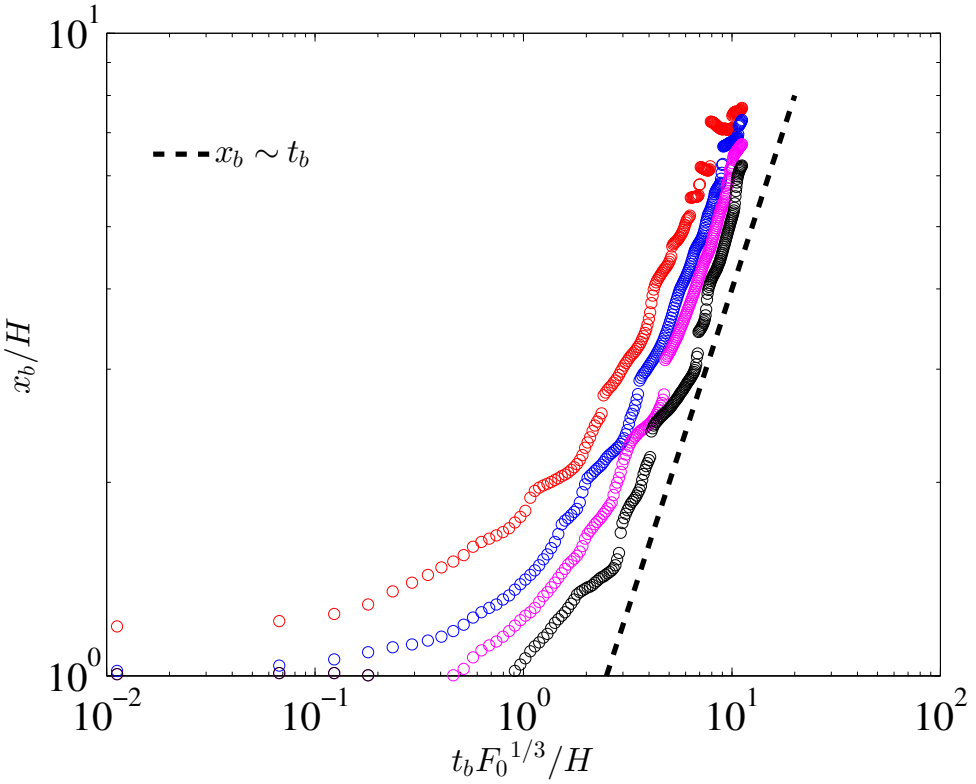

FIGURE 5.12: Position of counter-flowing gravity current front as function of time in the uniform environment for aspect ratio $(AR) = 8.0$. The black, magenta, blue and red dots indicates the location of return front at $z/H = 0.3$, 0.4, 0.5 and 0.6, respectively.

In this case, we considered the left wall as a reference location and the position of the front measured from that location, i.e $x_b = R + x$. The front position at four different locations in the $z-$ directions are indicated by different colours. These data suggest that the counter-flowing gravity currents front position is approximately linear with respect to time in all locations, which is equivalent to the normal planar gravity current flows (5.1).

5.2.5 Horizontal front propagation in a stratified environment

We measured the subsequent horizontal front movement generated by an impinging line plume in a stratified environment. We considered the continuing plume discharge (yellow colour in figure 5.13) after the domain has become partially stratified. Figure 5.14 shows vertical temperature profiles measured outside the plume for several x/H locations. These temperature profiles indicate that the

ambient fluid outside the plume is stratified. Figure 5.13 shows the subsequent front propagation in a stratified environment. Here, a threshold of 2.4 is chosen for non-dimensionalised temperature to identify the subsequent horizontal front. The front position is indicated by red dots which is the maximum horizontal extent of the interface curve (black line). We plot the subsequent horizontal front position

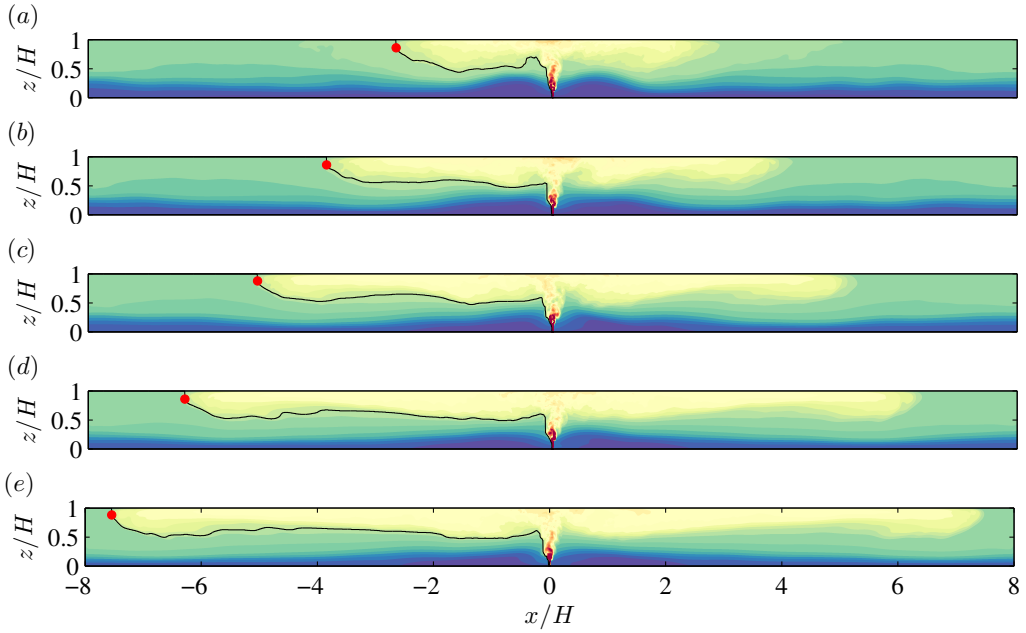

FIGURE 5.13: Contour plots of the line-averaged non-dimensionalised temperature ($\widetilde{T^*}$) for aspect ratio (R/H) = 8.0, showing the propagation of horizontal front in the stratified environment. At times $t^* = 33.65\,(a)$, $35.9\,(b)$, $38.14\,(c)$, $40.38\,(d)$ and $42.63\,(e)$. The red dots indicates the location of horizontal front front as a function of time. A threshold of 2.4 is chosen for non-dimensionalised temperature to define the interface (solid black lines).

as a function of time for aspect ratio ($R/H = 8.0$) as shown in figure 5.15. Here, the subsequent front propagation time t_s is based on a reference time t_{ref}, i.e. $t_s = t - t_{ref}$. The reference time t_{ref} is calculated when the subsequent buoyant fluid reaches the top wall. We can observe that the horizontal front moves linearly ($x \sim t_s$) in time after $x/H \approx 3.0$, which is similar to the earlier observations of the horizontal front position in uniform environment. However, in the region close to the impingement, the data do not follow the relationship $x \sim t_s^{2/3}$ which was expected in that regime (§5.2.1).

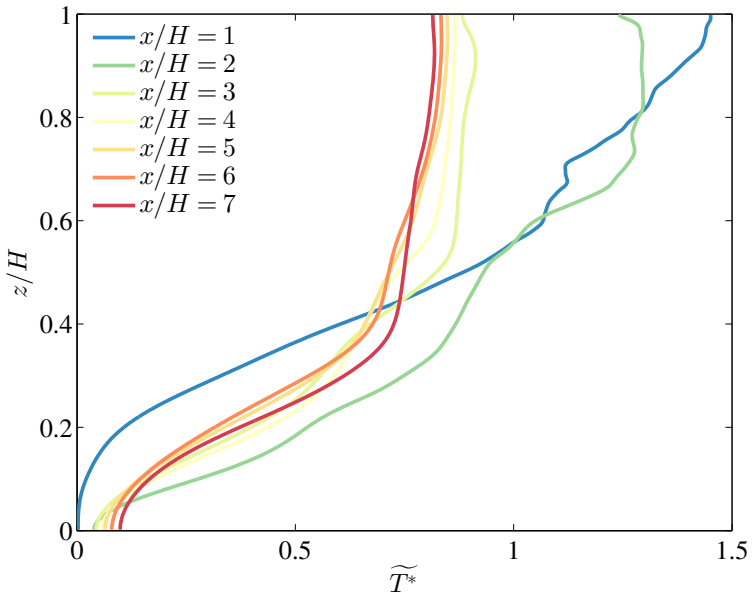

FIGURE 5.14: Vertical temperature profiles out side the plume at $t^* = 33.65$ for $R/H = 8$ and $Re_H = 3600$.

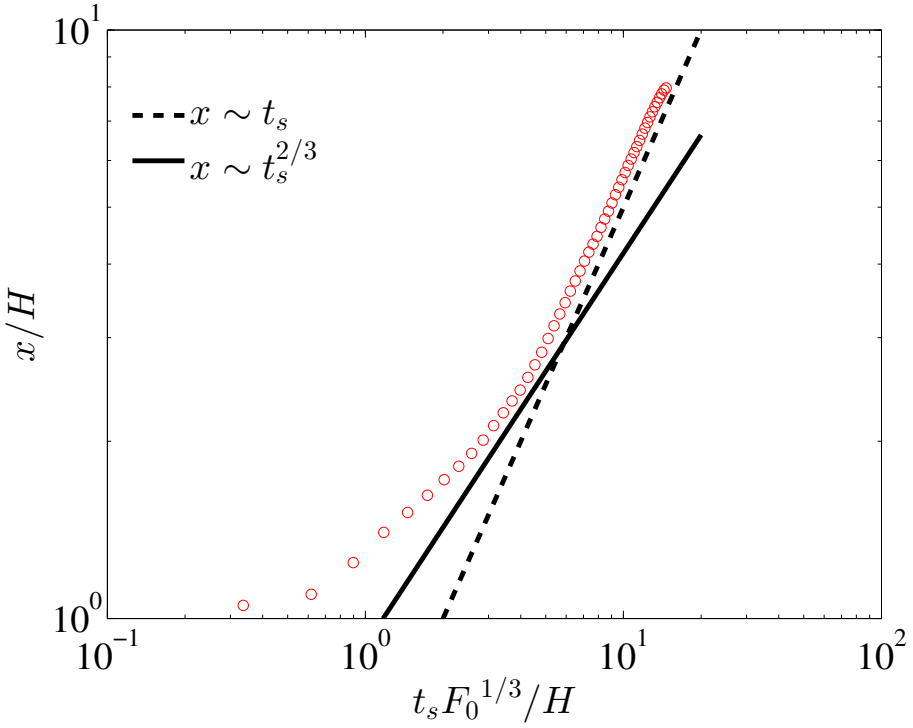

FIGURE 5.15: Non-dimensional subsequent planar horizontal front position x/H against time t_s in the stratified environment for aspect ratio box 8 and $Re_H = 3600$.

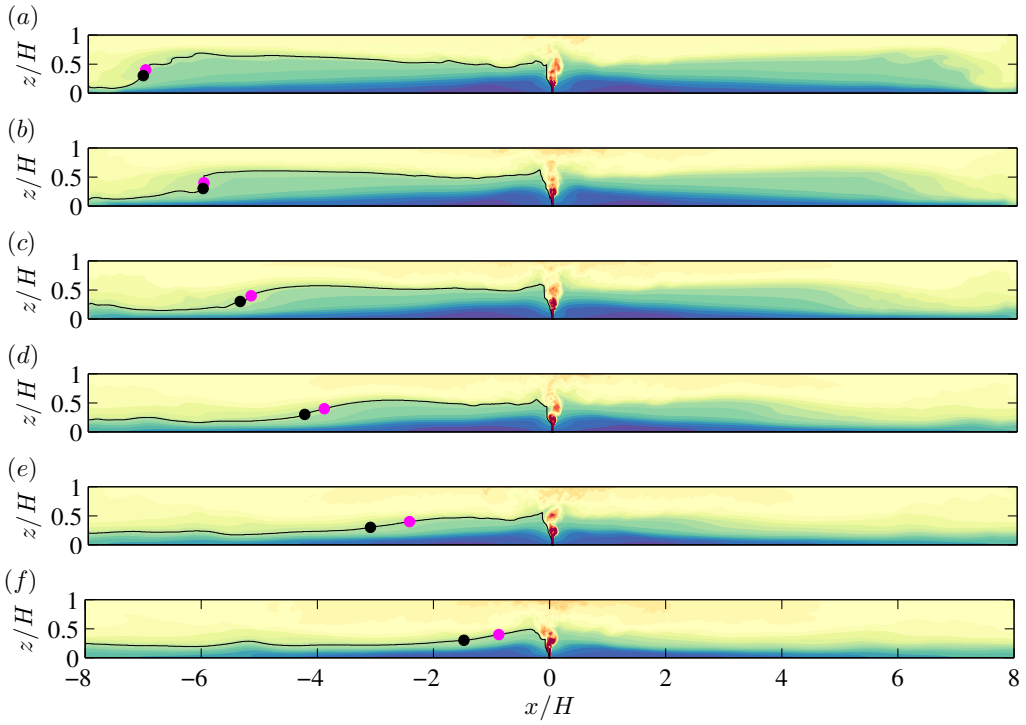

FIGURE 5.16: Contour plots of the line-averaged non-dimensionalised temperature ($\widetilde{T^*}$) for aspect ratio (R/H) = 8.0, showing the filling of the box from both sideways in the stratified environment. At times $t^* = 45.77\,(a)$, $48.01\,(b)$, $50.26\,(c)$, $52.50\,(d)$, $54.74\,(e)$, $56.82\,(e)$. The black and magenta dots indicates the location of return front at $z/H = 0.3$ and 0.4, respectively. A threshold of 2.4 is chosen for non-dimensionalised temperature to define the interface (solid black lines).

5.2.6 Counter-flowing gravity current front position in a stratified environment

We conducted an analysis for counter-flowing gravity current front position in a stratified environment. Figure 5.16 shows the evolution of counter-flowing gravity current and the contour plots are for the line-averaged non-dimensionalised temperature for aspect ratio (R/H) 8. The black and magenta dots indicates the location of return front at $z/H = 0.3$ and 0.4, respectively.

Figure 5.17 shows the positions of the front as function of time. The dashed black line represents the scaling laws for the normal gravity current like flows generated due to the impingement of the line plume (i.e. $x_b \sim t_b$). The notations x_b and t_b are the same that we used in §5.2.4. We can observe that the horizontal front moves linearly ($x_b \sim t_b$) in time after $x/H \approx 3.0$, which is similar to the earlier observations of the horizontal front position in uniform environment. However, in

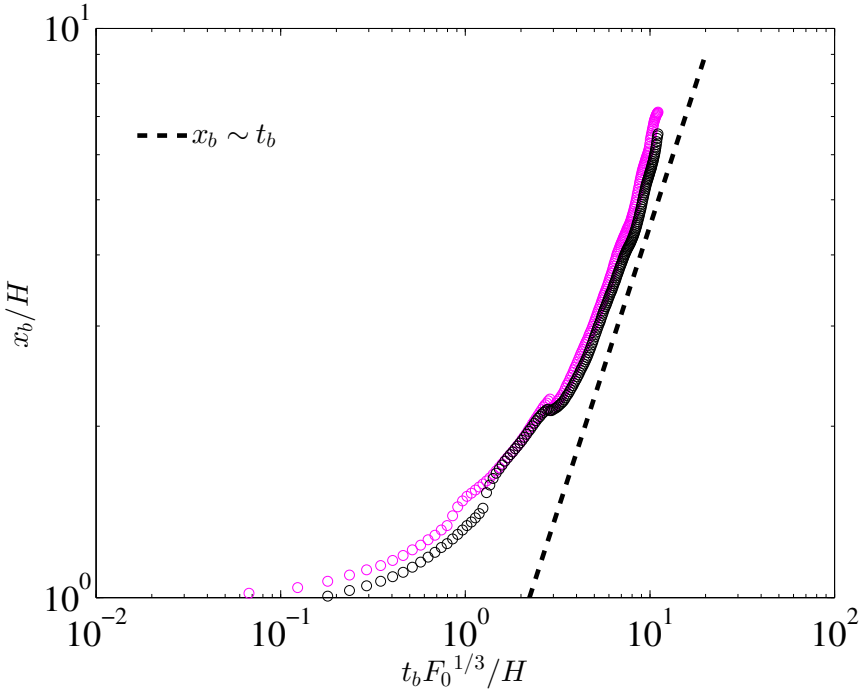

FIGURE 5.17: Position of counter-flowing gravity current front as function of time in the stratified environment for aspect ratio $(AR) = 8.0$. The black and magenta dots indicates the location of return front at $z/H = 0.3$ and 0.4, respectively.

the region close to the horizontal front impingement, the data do not follow the relationship $x_b \sim t_b$ which was expected in that regime (§5.2.1).

5.3 Chapter summary

In this chapter, the horizontal outflow from a thermal line plume after impinging onto the top wall is investigated. A set of direct numerical simulation (DNS) is conducted for different aspect ratio boxes ($R/H = 1, 2, 4, 8$ and16) to study the phenomenon of horizontal propagation of buoyant fluids in both uniform quiescent and stratified environments. A theoretical model has been developed for the bulk properties of horizontal outflow from a line plume similar to the work of Kaye and Hunt (2007) for axisymmetric plumes. The models agree well with the data obtained from the DNS. The constants of proportionality between the front position and the time are found by fitting curves to the DNS data. When the horizontal outflow reaches the side walls, it begins to flow downwards and then move in the opposite direction as a counter-flowing gravity currents. The front positions of

these types of buoyancy driven flows are measured and scaling relationships are obtained in both uniform quiescent and stratified environments.

Chapter 6

Confined wall plumes

This chapter incorporates the results of N. George, J. Philip & A. Ooi (2018) Direct Numerical Simulation of Confined Wall Plumes. Proceedings of the 21st Australasian Fluid Mechanics Conference 790, Adelaide

In this chapter, we carry out direct numerical simulations (DNS) of wall attached line plume in confined boxes, and compare the results with a modified version of Baines and Turner (1969)'s analytical model. The present study is restricted only to the transient stage and the results from the asymptotic stage are not discussed.

6.1 Theoretical model

We have adapted the original filling box model developed by Baines and Turner (1969) to model the wall attached line plumes in a confined region by including wall effects. The schematic diagram of wall attached plume in a confined region is shown in figure 6.1, where a line heat source is located at the bottom left corner of the box. The box height and width are H and R, respectively. The source generates a buoyancy flux F_0 per unit length and zero fluxes of volume and momentum.

We begin by considering the volume, momentum and buoyancy fluxes for a wall attached line plume, which can be derived from the continuity equation, the simplified Reynolds averaged momentum equation with Boussinesq approximation in the vertical direction (the pressure and the fluctuating terms are neglected) and the simplified energy equation (equations 6.1, 6.2 and 6.3, respectively). The

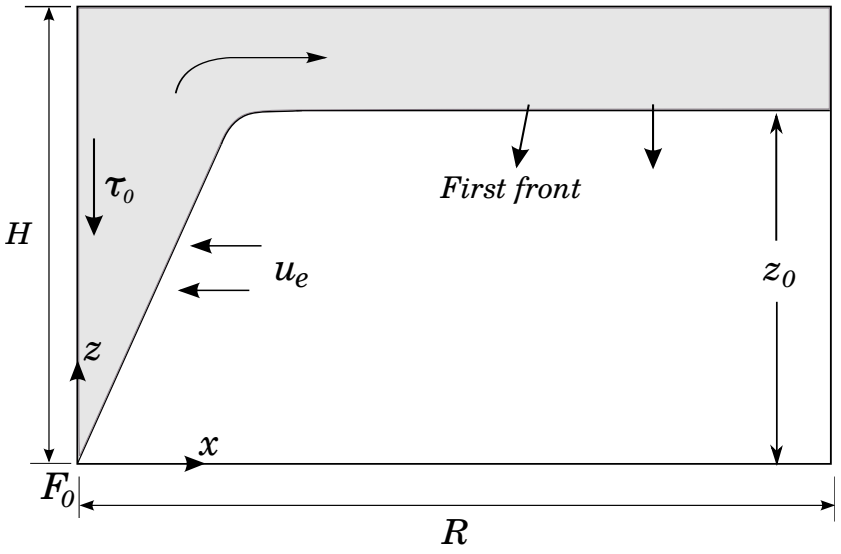

FIGURE 6.1: Schematic diagram of filling box model of wall attached line plume. The first front is the interface between buoyant fluid and the ambient fluid. The time-dependant position of the first front position is denoted by z_0.

mean velocity in the vertical direction z is denoted by $\overline{w}$, and in the $x-$direction is denoted by $\overline{u}$

$$\frac{\partial \overline{u}}{\partial x}+\frac{\partial \overline{w}}{\partial z}=0, \tag{6.1}$$

$$\frac{\partial \overline{u}\,\overline{w}}{\partial x}+\frac{\partial \overline{w}\,\overline{w}}{\partial z}+\frac{\partial \overline{u'w'}}{\partial x}+\frac{\partial(\overline{w'^2}-\overline{u'^2})}{\partial z}=\frac{1}{\rho}\frac{\partial \tau_x}{\partial x}+\frac{1}{\rho}\frac{\partial \tau_z}{\partial z}+g\beta(\overline{T}-\overline{T}_\infty), \tag{6.2}$$

$$\frac{\partial \overline{u}\,(\overline{T}-\overline{T}_\infty)}{\partial x}+\frac{\partial \overline{w}\,(\overline{T}-\overline{T}_\infty)}{\partial z}+\frac{\partial \overline{T'u'}}{\partial x}+\frac{\partial \overline{T'w'}}{\partial z}=-\overline{w}\frac{\partial \overline{T}_\infty}{\partial z}. \tag{6.3}$$

Here ρ is the density of the ambient fluid, g is the gravitational acceleration, β is the coefficient of thermal expansion, $\overline{T}$ is the mean temperature and $\overline{T}_\infty$ is the mean environmental temperature, which is far away from the plume. Also, u', w' and T' are the fluctuating components of u, w and T, respectively. Lastly, $\tau_x=\mu\,\partial\overline{w}/\partial x$ and $\tau_z=\mu\,\partial\overline{w}/\partial z$ are the shear stresses, where μ is the dynamic viscosity.

Integration of equation 6.1 along x gives

$$\frac{\mathrm{d}Q}{\mathrm{d}z}=-u_e, \tag{6.4}$$

where $Q=\int_0^\infty \overline{w}\,\mathrm{d}x$ is the volume flux and u_e is the entrainment velocity ($u_e=\overline{u}|_{x=\infty}$), which is evaluated far from the plume. Similarly, integration of equation

6.2 and 6.3 (ignoring the contribution of the fluctuating terms in the momentum and buoyancy flux) along x gives

$$\frac{\mathrm{d}M}{\mathrm{d}z} = \int_0^\infty g\beta\,(\overline{T} - \overline{T}_\infty)\,\mathrm{d}x - \tau_0, \text{ and} \tag{6.5}$$

$$\frac{\mathrm{d}F}{\mathrm{d}z} = -Q\,\frac{\partial \Delta_\infty}{\partial z}. \tag{6.6}$$

Here $M = \int_0^\infty \overline{w}^2\,\mathrm{d}x$ is the momentum flux, and $\tau_0 = c_f\,\frac{1}{2}w_m^2$ is the wall shear stress, where c_f is the skin friction coefficient and w_m is the maximum vertical velocity, $F = \int_0^\infty g\beta\,(\overline{T} - \overline{T}_\infty)\,\overline{w}\,\mathrm{d}x$ is the buoyancy flux and $\partial\Delta_\infty/\partial z$ is the environmental buoyancy gradient, with $\Delta_\infty = g\,\beta\,\overline{T}_\infty$.

Here, the mean vertical velocity($\overline{w}$) and reduced gravity($g\beta(\overline{T} - \overline{T}_\infty)$) are approximated by a half-Gaussian form, i.e. $\overline{w} = w_m \exp(-x^2/b_w^2)$, $g\beta(\overline{T} - \overline{T}_\infty) = \Delta \exp(-x^2/b_T^2)$, where $w_m(z)$ is the maximum vertical velocity, $\Delta(z)$ is the centreline reduced gravity and b_w and b_T are typical plume width associated with the vertical velocity and reduced gravity, respectively. Here, Gaussian profiles of equal width have been assumed for the vertical velocity and reduced gravity fields in the plume (i.e. $b_w = b_T = b$).

As suggested by Morton et al. (1956), the rate at which fluid is entrained into the plume is taken as proportional to the mean maximum vertical velocity of the plume, $u_e = \alpha\,w_m$, where α is the entrainment coefficient.

Now we can express the fluxes in terms of a maximum vertical velocity, $w_m(z)$, and reduced gravity, $\Delta(z)$, along with a plume width, $b(z)$, which are defined by,

$$Q = \frac{\sqrt{\pi}\,b\,w_m}{2},\quad M = \frac{\sqrt{\pi/2}\,b\,w_m^2}{2},\quad F = \frac{\sqrt{\pi/2}\,b\,w_m\,\Delta}{2}. \tag{6.7}$$

In terms of the fluxes, (6.4) and (6.5) become

$$\frac{\mathrm{d}Q}{\mathrm{d}z} = \sqrt{2}\,\alpha\frac{M}{Q}, \text{ and,} \tag{6.8}$$

$$\frac{\mathrm{d}M}{\mathrm{d}z} = \frac{FQ}{M} - c_f\,\frac{M^2}{Q^2}, \tag{6.9}$$

respectively.

The plume equations described above are reasonable approximations for the line plumes in unconfined environments with $c_f = 0$ (e.g. Lee and Emmons (1961);

Re_H	R/H	L/H	n_x	n_y	n_z	$\Delta x_c/b_0$	$\Delta y/b_0$	$\Delta z/b_0$	Approx. CPU time
14530	1	0.5	1024	256	512	0.123	0.157	0.157	7200 hours
14530	2	0.5	2048	256	512	0.123	0.157	0.157	15200 hours
29060	0.5	0.5	1024	256	2048	0.123	0.157	0.157	3100 hours

TABLE 6.1: Simulation parameters of the present cases. The cell grid sizes, Δx_c, Δy and Δz are non-dimensionalised by initial plume width b_0. The grid spacing in $x-$ direction, Δx_c is measured at the centre.

Paillat and Kaminski (2014a)). In the case of confined plumes, two other equations are considered for describing the environmental flow parameters. The conservation of mass in the filling box can be written as

$$Q = -R\,U, \tag{6.10}$$

where U is the downward velocity of the environment, and the development of the buoyancy field in the environment is governed by

$$\frac{\partial \Delta_\infty}{\partial t} = -U\frac{\partial \Delta_\infty}{\partial z}. \tag{6.11}$$

6.2 Set-up of direct numerical simulations

In this study, we employ direct numerical simulation (DNS) to solve the equations of mass, momentum and energy conservation within the Boussinesq approximation. The line plume originates from a line heat source of length L and initial width b_0 placed along the $y-$ direction at the bottom left corner of the box. The confining box has width R and height H in the $x-$ and $z-$directions, respectively. Here, the gravity acts in the negative $z-$direction, i.e. in the opposite direction to the rising plume.

The flux of temperature per unit area at the wall $f_w \equiv \kappa\,|\mathrm{d}T/\mathrm{d}z|_w$ $(= q_w/(\rho\,C_p))$, where κ is the thermal diffusivity, q_w is the wall heat output per unit area (W/m^2), C_p is the specific heat at constant pressure and ρ is the reference density of the fluid; the subscript w denotes properties at the bottom wall. For numerical simulation we take a smooth half-Gaussian profile at the wall over a distance of R

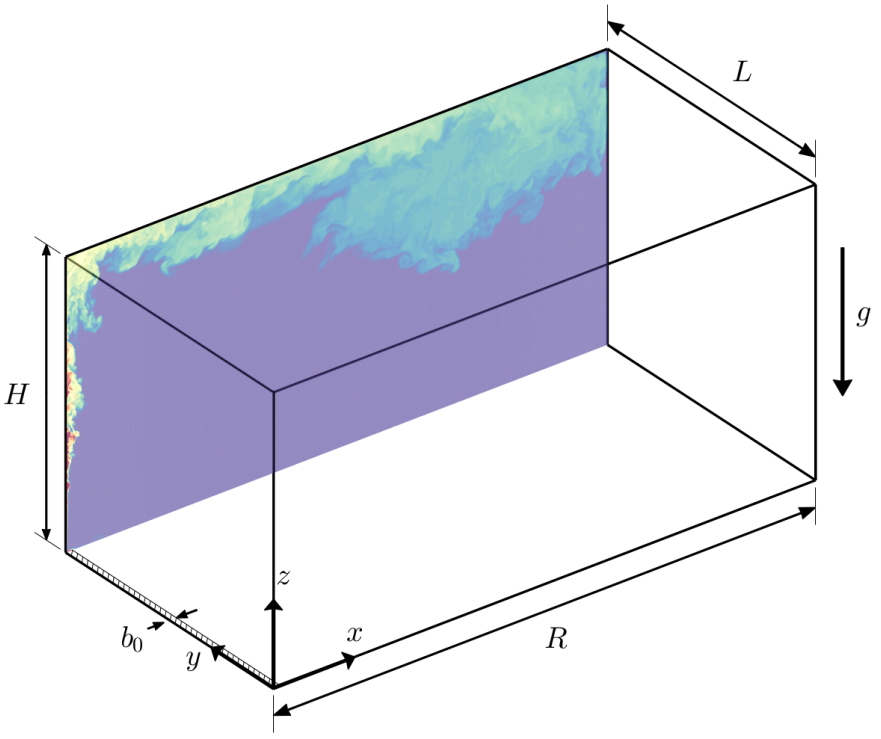

FIGURE 6.2: Contour plot of the instantaneous non-dimensionalised temperature (T^*) at $y/H = 0.5$ for aspect ratio $(AR) = 2$.

in $x-$ direction: $f_w = \kappa A_0 \exp(-x^2/b_0^2)$, where A_0 is the maximum value of $|\mathrm{d}T/\mathrm{d}z|_w$ and b_0 is the initial plume width. The buoyancy flux per unit area = $g\beta \times$ (temperature flux per unit area) $= g\beta f_w$. Now, buoyancy flux per unit length (in $y-$direction),

$$F_0 = g\beta \int_0^\infty f_w \, \mathrm{d}x = \sqrt{\pi} g \beta \kappa A_0 b_0/2. \tag{6.12}$$

The dimensionless parameters governing the present simulations are Reynolds number:

$$Re_H = F_0^{1/3} H/\nu, \tag{6.13}$$

where ν is the kinematic viscosity and Prandtl number, $Pr = \nu/\kappa$, which is fixed at the value for air: $Pr = 0.71$. The Reynolds number considered is $Re_H = 14530$ for boxes of two different aspect ratios, $R/H = 1$ and 2 (table 6.1). The value of b_0/H is 0.0125 for Reynolds number 14530. Baines and Turner (1969) observed that in order to avoid a large-scale circulation generated by the plume in the confined box, the stabilising buoyancy force in the region of plume outflow at the top of the box have to be larger than the inertial force of the plume. The ratio between these forces depends purely on the geometry of the box, i.e. aspect ratio

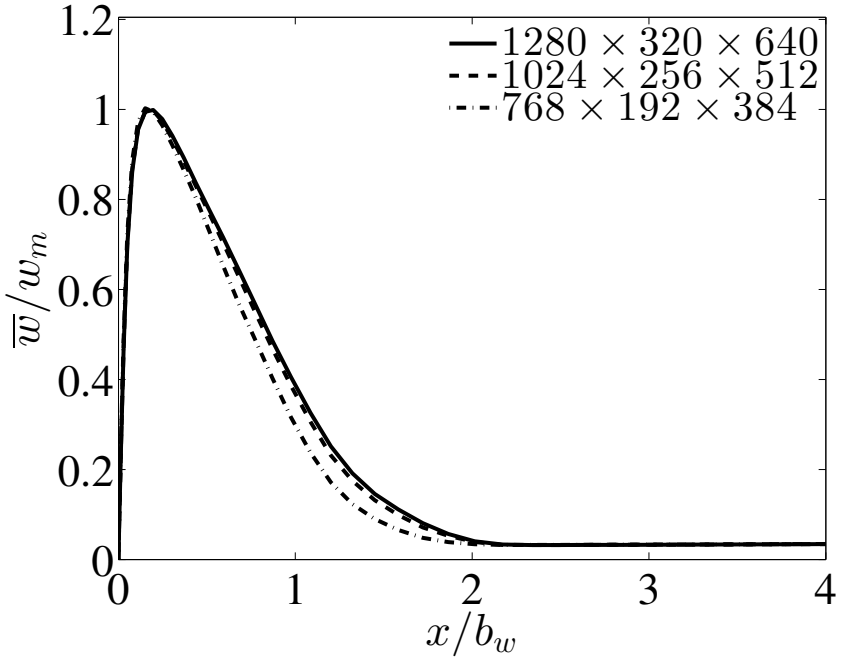

FIGURE 6.3: The variation of mean velocity profile at $z/H = 0.5$ for aspect ratio $R/H = 1.0$ for various grid densities.

(R/H) in this case, and not on the buoyancy flux or any other flow properties. In their experiments, they concluded that the critical value of the aspect ratio is about one. Therefore, in the present case, the lowest aspect ratio (R/H) of the box is set to one.

The bottom, top, left, and right boundaries are no-slip walls. Periodic boundary conditions are imposed on velocities, pressure and temperature in the $y-$direction. We set all initial velocities to zero and add a random perturbation to the temperature field in the entire domain, in order to trigger a transition to turbulence in the rising plume. The magnitude of temperature perturbations $(T(t = 0))$ added to the flow is based on $(g\,\beta\,T\,b_0)^{1/2}\,b_0/\nu = 25.0$, and is kept constant for all simulations. Before we run the two case listed in table 6.1, we have to ensure that the box is tall enough that we get a 'nearly turbulent' plume. This is because, the plume starts laminar at the bottom as it develops upward along the wall, and takes some distance in z before the instabilities develop over the laminar buoyant base flow and transitions to a nearly turbulent wall flow. Although this transitional flow is of interest by itself, it is not the focus of this work. The theoretical model here (in anticipation of the practical cases) is constructed for a turbulent plume. As such, as an initial case, we run simulations in a taller box. Within the available computational resources, we start with a tall box of dimensions $80\,b_0 \times 40\,b_0 \times 160\,b_0$

in the x, y and z directions, respectively. We recall that the boxes in table 6.1 are only $80\,b_0$ in height, which we decided after running this taller box. The grid resolutions in all directions and other flow parameters are kept constant for this taller case. We note that grid resolutions Δx, Δy and Δy are fixed to fully resolve all the turbulent scales up to the Kolmogorov scale by following the recommendations Stevens et al. (2010), as well as employing a grid independence test. To see the effect of size of the numerical grid, a thorough grid independent test has been conducted for aspect ratio $R/H = 1.0$ with $Re_H = 14530$ case. Three levels of grids namely, $1280 \times 320 \times 640$, $1024 \times 256 \times 512$ and $768 \times 192 \times 384$ have been tested. Figure 6.3 shows the variation of mean velocity profile at $z/H = 0.5$ for aspect ratio $R/H = 1$ and $Re_H = 14530$ for various grids. It has been observed that the grid is refined, variation in the results between two successive grids decreases. For the two finest level of grids, variation in mean velocity remains below 1%. This also led us to use the grid $1024 \times 256 \times 512$ for $R/H = 2$ case to achieve consistent accuracy.

The grid spacing is uniform in the $y-$ and $z-$directions and a cosine stretching grid is set in the $x-$ direction. The DNS employs a mixed spectral/finite-difference algorithm for the spatial discretisation. While a fully conservative fourth-order, staggered finite-difference scheme is used for the velocity field calculation in the $x-$ and $z-$ directions, a Fourier spectral method is used in the $y-$ direction. The QUICK scheme is used to advect the temperature field. The equations are marched using a low-storage third-order Runge - Kutta scheme.

6.3 DNS results

6.3.1 Wall plume in uniform environment

6.3.1.1 Wall plume development

In order to fix the height of the box to obtain a fully developed wall plumes within the available computational resources, we start with a long box of dimensions $80\,b_0 \times 40\,b_0 \times 160\,b_0$ in the x, y and z directions, respectively. The grid used for this case is $1024 \times 256 \times 2048$. The grid resolutions in all directions (table 6.1) and other flow parameters are kept constant for this case. Figure 6.4 (a)

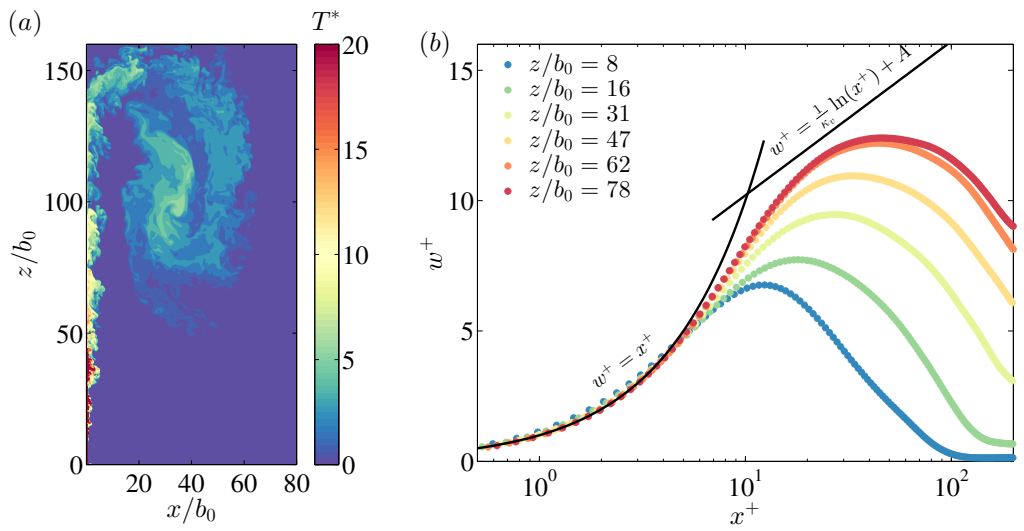

FIGURE 6.4: (a) Instantaneous contour plot of vertical velocity at $y/b_0 = 5.0$ and (b) evolution of mean vertical velocity profile scaled in inner variables.

shows the instantaneous contour plots of non-dimensionalised temperature ($T^* = T/(F_0^{2/3}/(g\beta H))$, where $H = 160\,b_0$), which indicates the development of wall plume along the left side wall. The axes are non-dimensionalised with the initial Gaussian half width of the wall plume b_0. In this case, we have chosen the non-dimensionalised time t^* as $t^* = t\,F_0^{1/3}/b_0$. The Reynolds number of the plume is based on the initial plume width b_0 and the buoyant velocity $F_0^{1/3}$,

$$Re_0 = F_0^{1/3} b_0/\nu, \tag{6.14}$$

is chosen to be 182, which is sufficiently large so that the flow turns into a nearly turbulent state within the height $H/b_0 \approx 160$. Before we run the two case listed in table 4.1, we have to ensure that the box is tall enough that we get a 'nearly -turbulent' plume. This is because, the plume starts laminar at the bottom as it develops upward along the wall (6.5), and takes some distance in z before the instabilities develop over the laminar buoyant base flow and transitions to a nearly turbulent wall flow Once the wall plume reaches the steady state, the time-averaged statistics are taken from when $t^* = 155$ to 218 at an interval of 0.15 time units.

The evolution of mean vertical velocity profile scaled in inner variables is shown in figure 6.4 (b), where the profiles are coloured from blue to red indicate increasing z/b_0. Here, $x^+ \equiv x/\delta_v$, where $\delta_v \equiv \nu/w_\tau$ is the viscous length scale and $w_\tau \equiv \sqrt{\nu\,\mathrm{d}\overline{w}/\mathrm{d}x|_w}$ is the friction velocity scale. Note that we use $^+$ symbol to denote normalisation with viscous wall units.

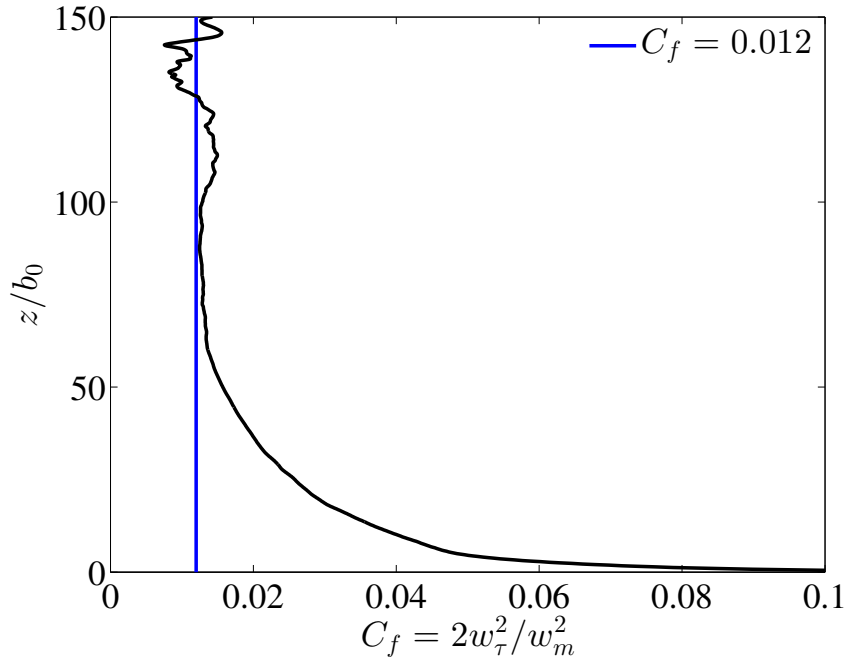

FIGURE 6.5: Variations of time-averaged value skin friction coefficient along $z-$ direction

At $z/b_0 = 8.0$, the wall plume is laminar with thin laminar boundary layers. The wall plume reached fully turbulent regime at $z/b_0 \approx 60.0$, which is observed from figure 6.5. The mean velocity profile is well developed has reached the self-similar state. Very near the wall, the mean velocity profiles are linear as expected, i.e. obey $w^+ = x^+$, but begin to deviate from this linear behaviour beyond $x^+ = 5.0$, which is similar to the standard boundary layer (cf. Pope (2001)). However, due to the limited domain height, the velocity profiles not reached the classical log-law for boundary layers. The log-law of the wall for boundary layers may be written as,

$$w^+ = \frac{1}{\kappa_v} \ln(x^+) + A, \tag{6.15}$$

which is plotted in figure 6.4 (b) as solid black line. In this case, we adopt the constants as Marusic et al. (2013), i.e. the von Kármán constant $\kappa_v = 0.39$ and $A = 4.3$.

The variations of skin friction coefficient C_f defined as

$$C_f = 2\left(\frac{w_\tau}{w_m}\right)^2, \tag{6.16}$$

along the vertical direction is shown in figure 6.5. The variation of skin friction coefficient is observed to be high near the laminar region ($z/b_0 < 60$). In the fully turbulent region of the wall plume ($z/b_0 > 60$), the value of C_f has been reduced to a constant value, which is about 0.012.

Next section onwards, we explore the dynamics of wall attached plumes in the confined environments with different aspect ratios. We need more computer resources to conduct this kind of DNS due to larger domain size. Therefore, we fixed the height of the box to be $80\,b_0$ and take the value of C_f as 0.012 for further study.

6.3.1.2 Comparison with theoretical model

In this section, we discuss the behaviour of turbulent wall plumes in a uniform environment and compare the results with the theoretical model of the wall plume.

Figures 6.6 and 6.7 show the instantaneous contour plots of temperature and vertical velocity ($w^* = w/{F_0}^{1/3}$) at two time instances (when the horizontal front reached at $x/H \approx 1.0$ and at $x/H \approx 2.0$), respectively. During this period time, the region up to $x/H = 0.25$ which includes the wall plume without any external disturbance is considered to be statistically steady plume in a uniform environment. The mean profiles are obtained by averaging spatially along the $y-$ direction as well as averaging across the time instances during which the horizontal front travels from $x/H = 1.0$ till $x/H = 2$ (approximately 200 data samples in time).

Figure 6.8 shows of the statistical mean vertical velocity and buoyancy profiles at different z/H locations in a uniform environment for $R/H = 2$ case. In figures 6.8(a) and (b), the x- axes are normalised with plume widths b_w and b_T, the widths at which the distribution has fallen to $1/e$ of its peak value. In the theoretical model, the mean vertical velocity and buoyancy profiles are assumed to be self-similar with height. It is clear from both figures 6.8 (a) and (b) that, within the region $0.375 \lesssim z/H \lesssim 0.75$, the vertical velocity and buoyancy profiles are self-similar.

Figure 6.9 (a) shows the variation of entrainment coefficient α along $z-$ direction in a uniform environment. It is obtained from the volume flux equation in (6.8) i.e.

$$\alpha = \frac{1}{\sqrt{2}} \frac{Q}{M} \frac{\mathrm{d}Q}{\mathrm{d}z} \tag{6.17}$$

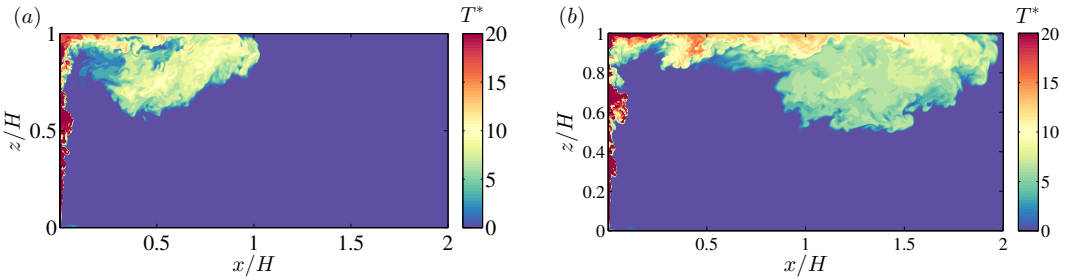

FIGURE 6.6: Instantaneous contour plots of temperature at $y/H = 0.25$ showing the horizontal propagation of wall plume for $Re_H = 14530$ and $R/H = 2.0$ time instances when the horizontal front reach at $x/H \approx 1.0$ (a) and at $x/H \approx 2.0$ (b).

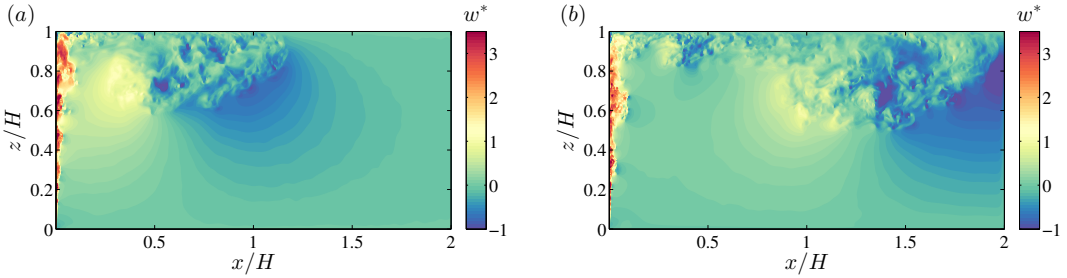

FIGURE 6.7: Instantaneous contour plots of vertical velocity at $y/H = 0.25$ showing the horizontal propagation of wall plume for $Re_H = 14530$ and $R/H = 2.0$ at time instances when the horizontal front reaches $x/H \approx 1.0$ (a) and $x/H \approx 2.0$.

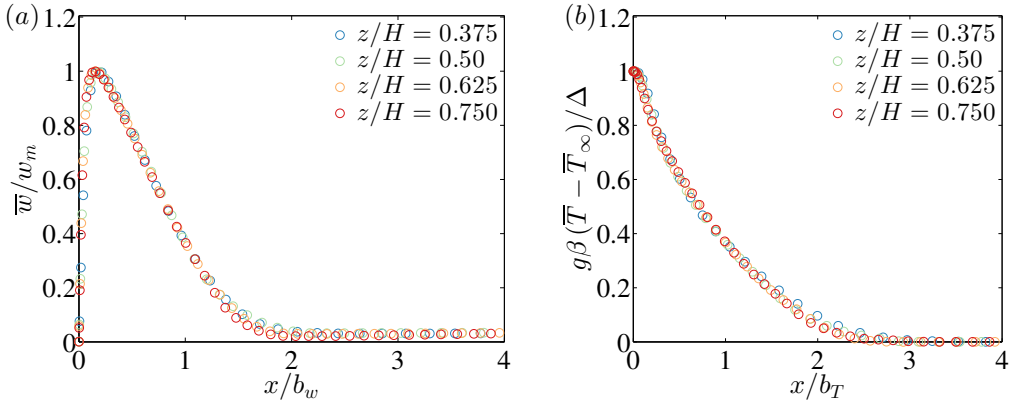

FIGURE 6.8: Mean profiles of (a) Vertical velocity and (b) buoyancy at $0.375 \leq z/H \leq 0.75$ for the $R/H = 2$ case.

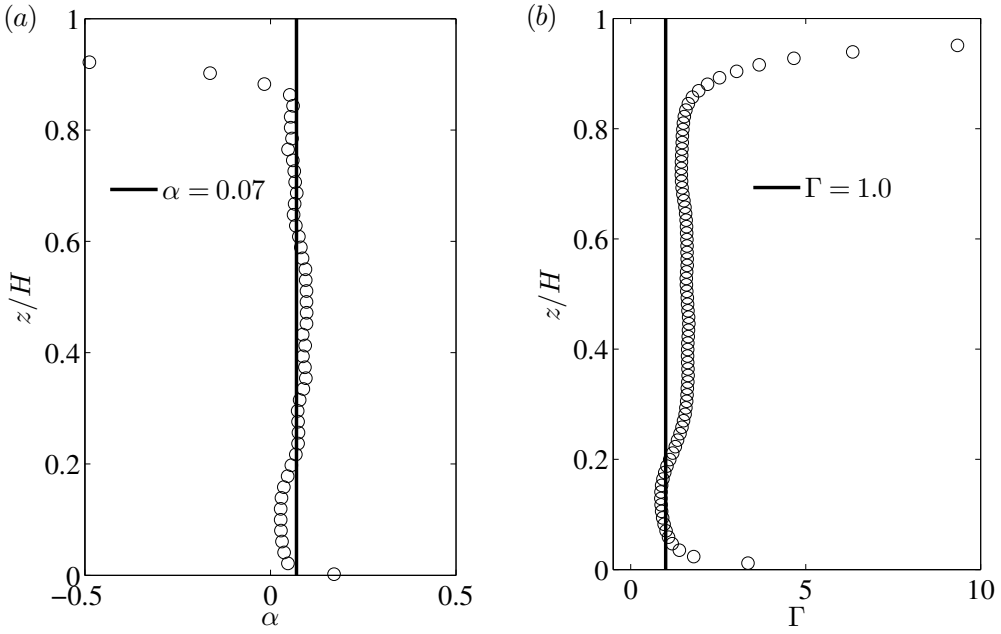

FIGURE 6.9: Variation of (a) entrainment coefficient α and plume function Γ evaluated from the mean fluxes in a uniform environment.

and used second order central-difference scheme for $\mathrm{d}Q/\mathrm{d}z$. To compute the integrals over the $x-$ directions of the plume, we fitted a half-Gaussian curve to the vertical velocity profile at each z/H locations based on the maximum vertical velocity w_m and width b_w (width at which the vertical velocity has fallen to $1/e$ of its central value) and we defined the integration limit $\pm x_\infty$ such that $\overline{w}(\pm x_\infty, z) = w_m(z)/100$ from the fitted Gaussian curve, which ensures that the vertical environmental velocity is small relative to that of the plume. The black solid line in figure 6.9 (a) is a linear fit with zero slope to the data from $z/H = 0.2$ to $z/H = 0.7$, which shows the value of entrainment coefficient $\alpha = 0.07$. In the present study, this value of α is set to a fixed value and used for all calculations in the turbulent wall plumes. It is shown that the value of entrainment coefficient obtained here is much less than in the case of free line plumes.The findings of Grella and Faeth (1975), Lai and Faeth (1987), Sangras et al. (2000) and Parker et al. (2020) have found similar value of entrainment coefficients, varying from 0.061 to 0.071 for wall attached line plumes in an open environment. These values are much less than in the case of free-plumes. But recent study of Akhter and Kaye (2020) found that the entrainment coefficient for a wall plume is the same as for an isolated plume. They used first front movement to calculate the entrainment coefficient. The value of α for wall-plumes reported here is calculated based on the volume flux equation.

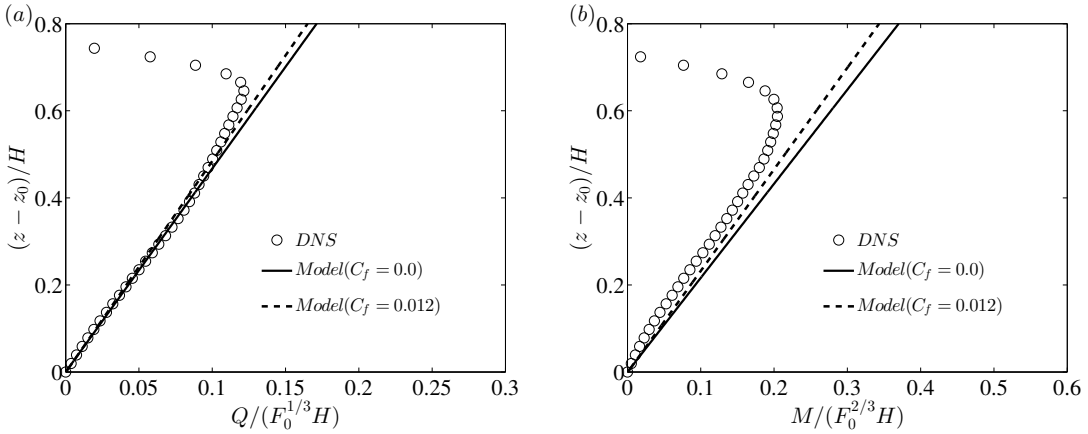

FIGURE 6.10: Comparison of mean (a) volume and (b) momentum flux with the theoretical model in a uniform environment. The black circle represents the DNS results , the black solid and dashed lines represent the theoretical model with $c_f = 0.0$ and $c_f = 0.012$, respectively.

A flux balance parameter Γ for Gaussian profiles

$$\Gamma(z) = \frac{1}{\sqrt{2}\alpha}\frac{Q^3(z)F(z)}{M^3(z)} \tag{6.18}$$

is plotted in figure 6.9 (b) with $\alpha = 0.07$. Based on the value of Γ at the source, $\Gamma_0 = \Gamma(0)$, the line plumes are characterised as forced plumes ($0 < \Gamma_0 < 1$), pure plumes ($\Gamma_0 = 1$) and lazy plumes ($\Gamma_0 > 1$). The $\Gamma_0 = \infty$ for a pure buoyancy driven thermal plumes but the value of Γ reaches pure plume behaviour immediately after the source. The solid black line in figure 6.9 (b) shows $\Gamma = 1$ (for pure plume case).

Figures 6.10 (a) and (b) show, respectively, the comparison of mean volume and momentum flux with the theoretical models. In order to find the theoretical fluxes, we solved (6.8) and (6.9) numerically with initial conditions of $Q_0 = 0.0$, $M_0 = 0.0$ and $F = F_0 = 1.0$ for $c_f = 0.0$ and $c_f = 0.012$. In the uniform environment, the buoyancy flux F is constant with respect to the height (i.e. $F(z) = F_0$). The value of skin-friction coefficient, $c_f = 0.012$ is obtained from our present DNS data.

Caudwell et al. (2016) experimentally investigated a turbulent plume generated by an isothermal wall in a closed cavity, which is similar to our present study. Caudwell et al. found that the wall plume is laminar over approximately one-third of its height. Similarly, we observed a laminar region upto $z/H \approx 0.2$ from

the bottom, where the theoretical model is not applicable. Therefore, we offset the wall plume source by $z_0/H = 0.2$ above the actual source and compared the theoretical fluxes from that point. The modified profiles of volume flux and momentum flux are shown in figures 6.10 a and b, respectively. The mean volume flux profile (figures 6.10 a) shows good agreement with the theoretical model and the skin-friction coefficient has an insignificant effect on volume flux. But the mean momentum flux (figures 6.10 b) shows moderate agreement with the model for $c_f = 0.012$. The difference between the model and the DNS data highlights the need for improved models in future.

6.3.2 Flow Visualisations

The wall-parallel planes (y-z plane at $x/b_0 = 5.0$) of instantaneous temperature ($T^* = T/(F_0^{2/3}/(g\beta H))$) and vertical velocity ($w^* = w/F_0^{1/3}$) for $Re_H = 14530$ and $R/H = 2.0$ case at two different time instances are shown in figures 6.11 and 6.12, respectively.

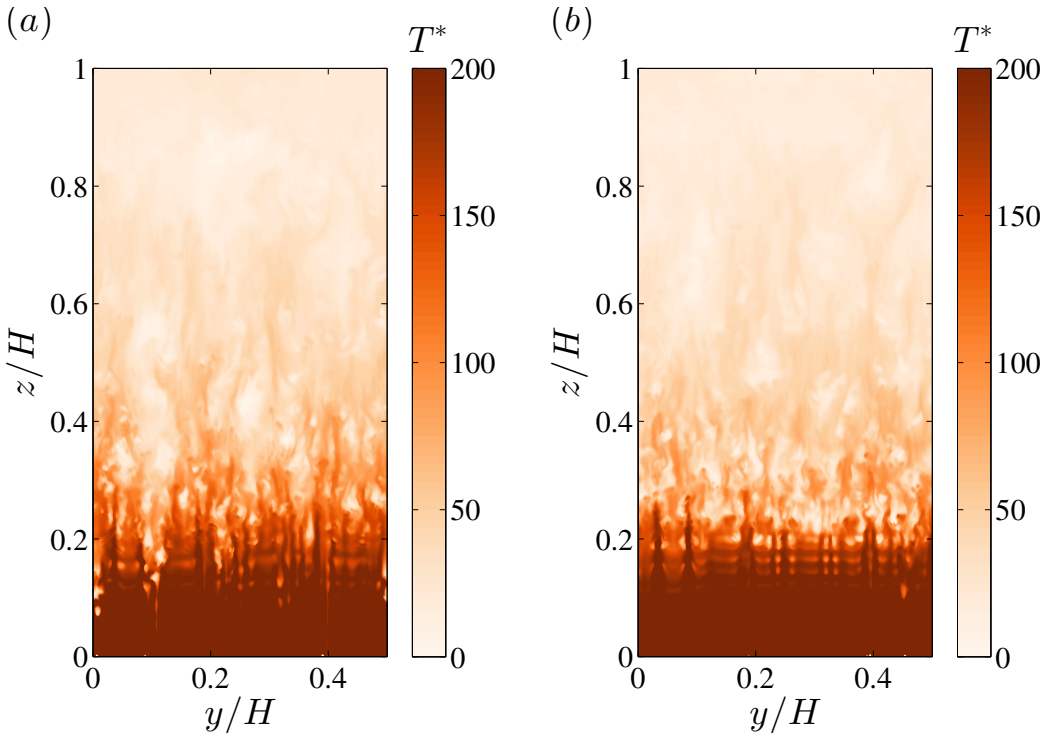

FIGURE 6.11: Instantaneous contour plots of temperature in y-z plane (at $x/b_0 = 5.0$) at time $t\,F_0^{1/3}/H = 2.6$ (a) and 3.0 (b).

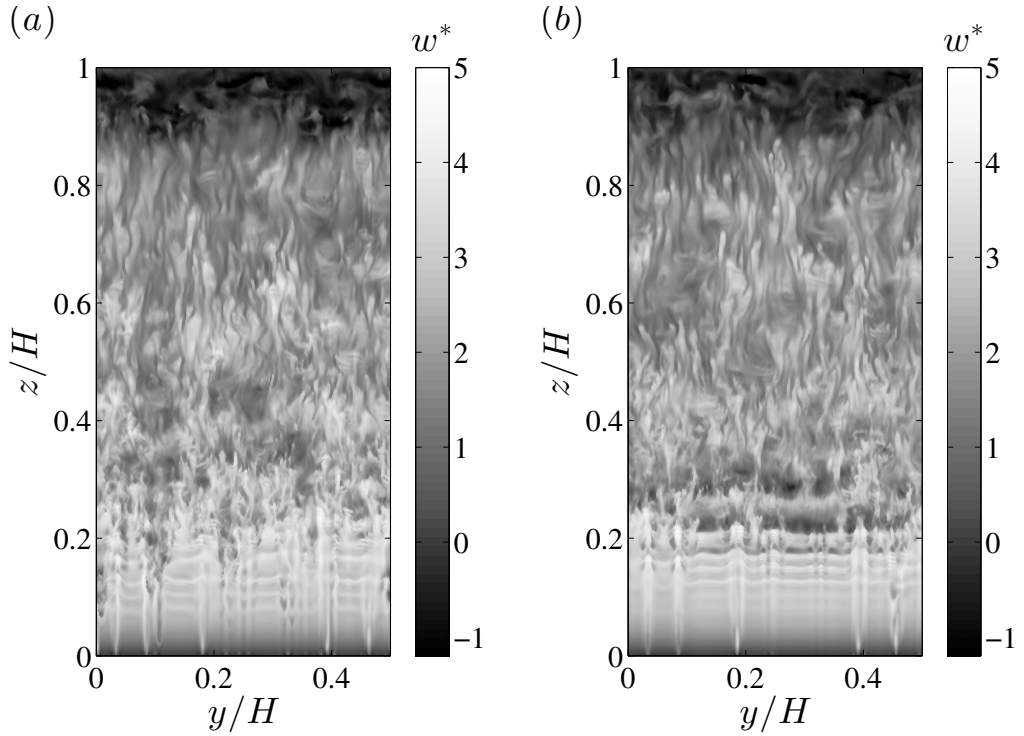

FIGURE 6.12: Instantaneous contour plots of vertical velocity in y-z plane (at $x/b_0 = 5.0$) at time $t\,F_0^{1/3}/H = 2.6$ (a) and 3.0 (b).

By looking at these contour plots (figures 6.11 and 6.12), laminar-like streamwise streaks are observed near the source region ($0 \leq z/H \lessapprox 0.2$) of the wall plume. The streamwise streak in this region exhibit minimal lateral movement, but they occasionally move slightly or interact with adjacent streaks. The region above $z/h \approx 0.2$ is considered to be turbulent. So, the lateral movement of streaks in the turbulent region is quite noticeable (figure 6.12 *a* and *b*), and streaky structures interact with each other through merging and splitting behaviours.

6.3.3 Time-dependent environmental buoyancy profile

As the plume hits the top wall, it spreads and advects downwards as a front (cf. figure 6.13). The front location and the instantaneous buoyancy profile in the environment Δ_∞ can also be estimated from our model. As such, we solved the differential equations (6.6), (6.8), (6.9) and (6.11) simultaneously to obtain the time-dependent environmental buoyancy profiles. Euler method is used to solve these equations. In the Euler method, a pure plume solution is given at the source (i.e. $Q_0 = 0.0$, $M_0 = 0.0$ and $F_0 = 1.0$) and integrating (6.11) over each time step to obtain the behaviour of Δ_∞. The non-dimensional time step

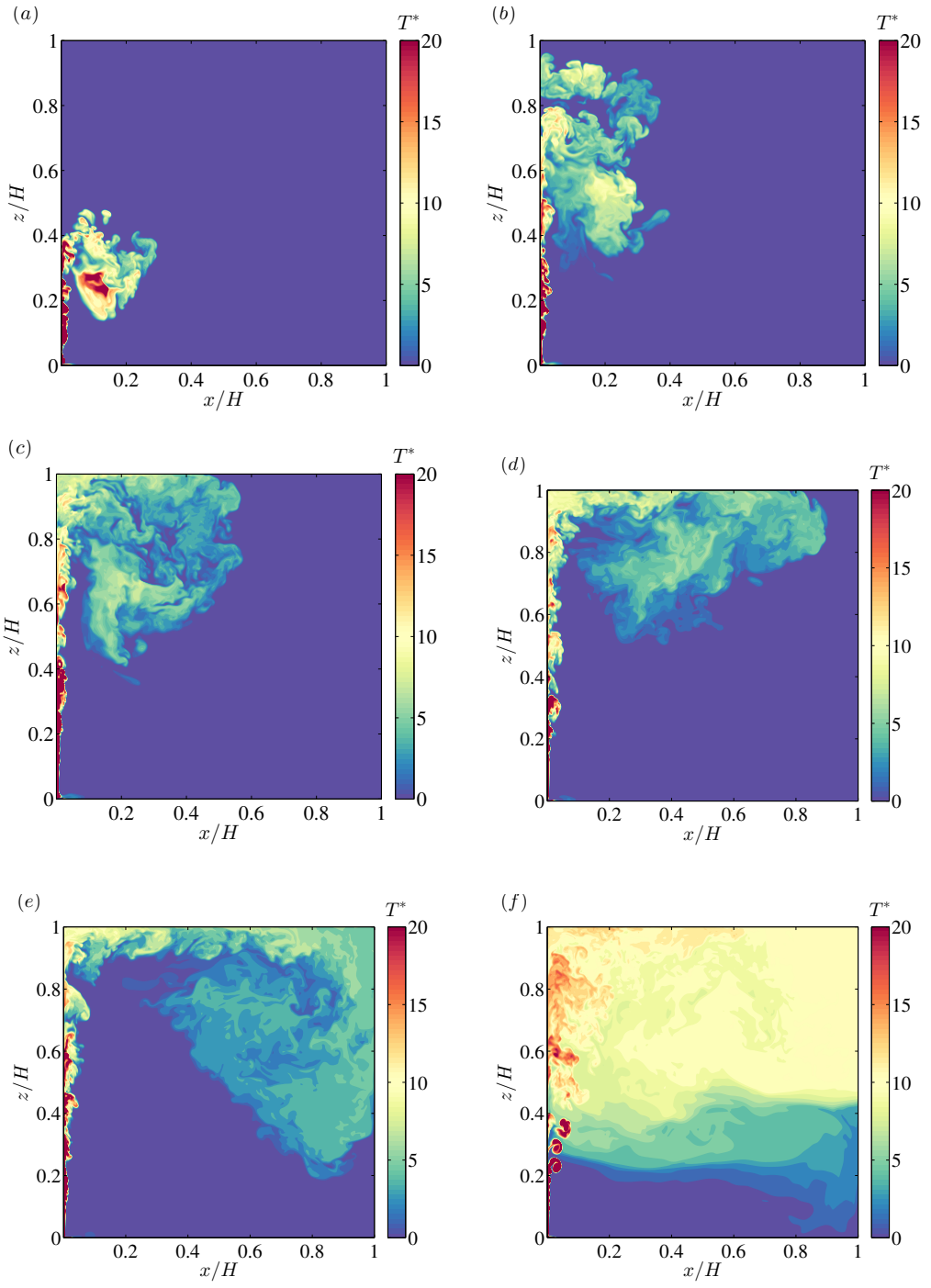

FIGURE 6.13: Contour plots of the instantaneous temperature (at $y/H = 0.5$) showing the evolution of the plume to the asymptotic state for $Re_H = 14530 (R/H = 1.0)$ at times $t\,F_0^{1/3}/H = 0.63$ (a), 1.0 (b), 1.22 (c), 1.6 (d), 2.22 (e) and 7.0 (f).

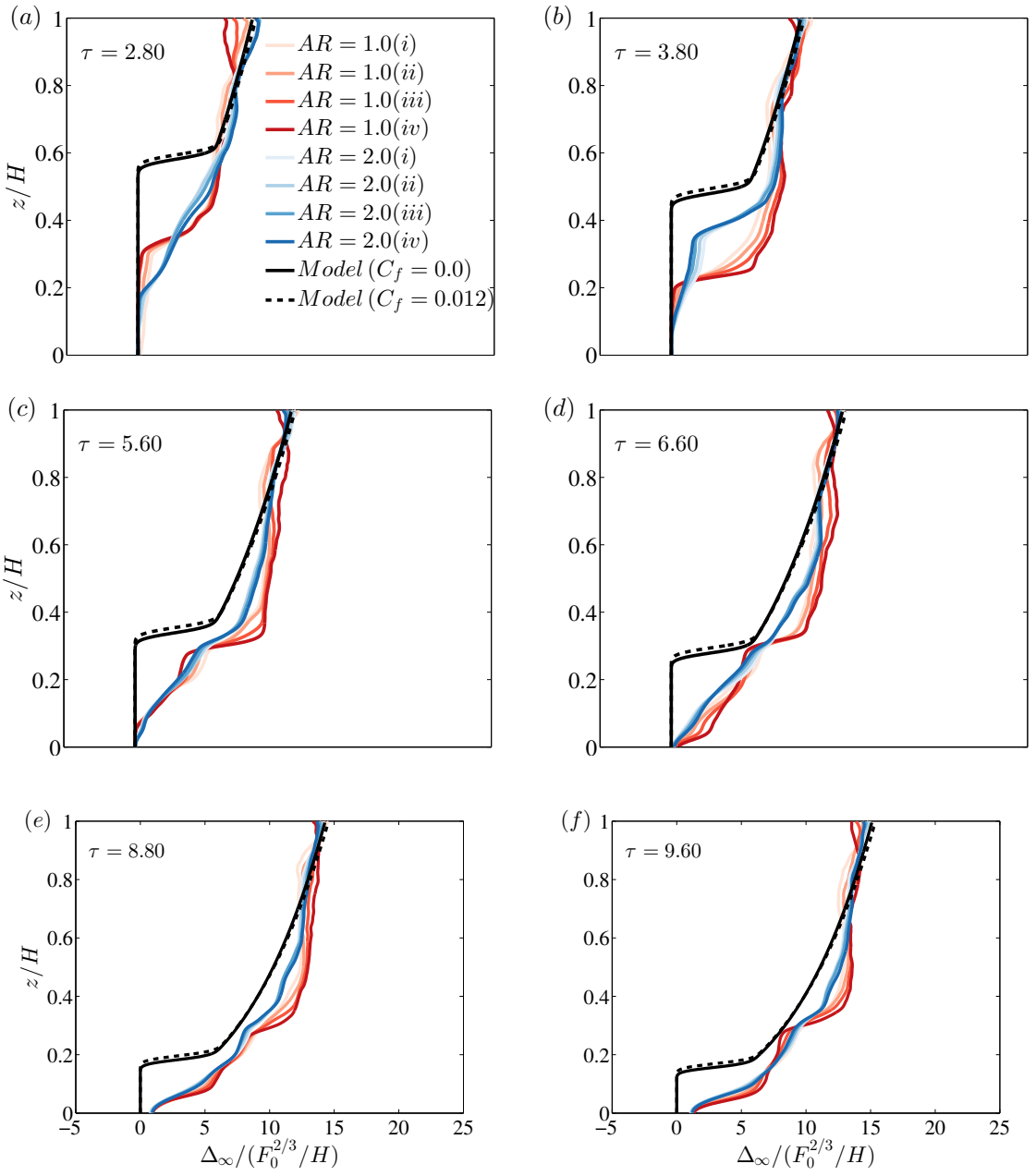

FIGURE 6.14: Comparison of the time-dependent environmental buoyancy profile with theoretical model for $AR = 1.0$ and $AR = 2.0$; (a) $\tau = 2.80$; (b) $\tau = 3.8$; (c) $\tau = 5.6$; (d) $\tau = 6.60$; (e) $\tau = 8.8$; and (f) $\tau = 9.6$. The colour gradients of red and blue indicates the starting point of horizontal average for two different aspect ratios; (i) for horizontal average from $x/H = 0.2$, (ii) for $x/H = 0.4$, (iii) for $x/H = 0.6$ and (iv) for $x/H = 0.8$.

used in the computations is 1×10^{-4}, which satisfies the stability considerations. Here we assume that the time step (δt) is much smaller than the spatial resolution (δz), i.e $\delta t \ll \delta z$ and we also assume that the plume spread quickly to form a horizontal layer at the top of the box ($z = H$), i.e. $\Delta_\infty(H, t + \delta t) = \Delta(H, t)$. The comparison of the time-dependent environmental buoyancy profile with the theoretical model for $AR = 1.0$ and $AR = 2.0$ is shown in figure 6.14. Here, τ is the non-dimensionalised time, which is defined as $\tau = t\,{F_0}^{1/3}/R$. We take the time $\tau = 0$ as the moment when the plume first touches the right wall, which is taken as the reference time. The line-averaged buoyancy near the side walls are considered to be environmental buoyancy, which is used here for comparison. In figure 6.14, the gradients red and blue lines represent the horizontally averaged buoyancy from different x/H locations to the right wall for $AR = 1.0$ and $AR = 2.0$, respectively. The solid black line shows the numerical solution of theoretical model with $c_f = 0.0$ and the dashed line shows the numerical solution with $c_f = 0.012$. The influence of skin friction coefficient on environmental buoyancy is observed to be negligible. Considering the assumptions involved, the model shows reasonable agreement for the buoyancy profile with the DNS results at all times. However, the observed interface locations are different from the model and DNS data overpredicted the analytical model below $z/H \approx 0.6$. This discrepancy appears to result from the fact that buoyant fluid outside the plume is not as uniform as is assumed in the analysis. This may be due to the overturning of the upper buoyant fluid layer during the initial transients in both aspect ratio boxes ($R/H = 1$ and 2). This would suggest that even larger values of R/H might be required to before the inertial overturning effects become negligible.

6.4 Chapter summary

The evolution of wall attached turbulent line plumes in a confined region is analysed using direct numerical simulations. The Reynolds number of the confined plume based on the box height and buoyant velocity scale is fixed at $Re_H = 14530$, and for boxes of two different aspect ratios, $R/H = 1$ and 2. The results from the DNS are compared against a modified theoretical model based on Baines and Turner (1969), where wall shear stress is incorporated to model the wall-attached plume. The distribution of mean volume and momentum fluxes in the uniform environment is observed to show good agreement with the theoretical model. The

time-dependent buoyancy profile showed moderate agreement with the model, and the effect of wall shear stress on environmental buoyancy is found to be small.

Chapter 7

Turbulence properties of line plumes

In this chapter, we conduct an investigation on the turbulent properties of various configurations of line plumes, i.e. free, wall-attached and confined line plumes.

7.1 2nd order statistics

The results have been spatially averaged in the $y-$ direction and also been temporally averaged until statistical convergence was reached. The mean statistics are computed by averaging over at least 60 non-dimensional time units at the interval of 0.42 time units.

7.1.1 Free-line plumes

In figure 7.1 (a) and (b) we plot the cross-sectional variation of the normalised root mean square (RMS) vertical, w_{rms} and horizontal, u_{rms} velocities for free line plumes. The black diamond symbols in figure 7.1 represent data from Parker et al. (2020). The measurements of Parker et al. (2020) are close to the results from DNS for all turbulent quantities. It is seen that over the range of streamwise distances considered, the profiles are universal within the uncertainties found in the numerical data. The magnitude of streamwise turbulent intensities near the

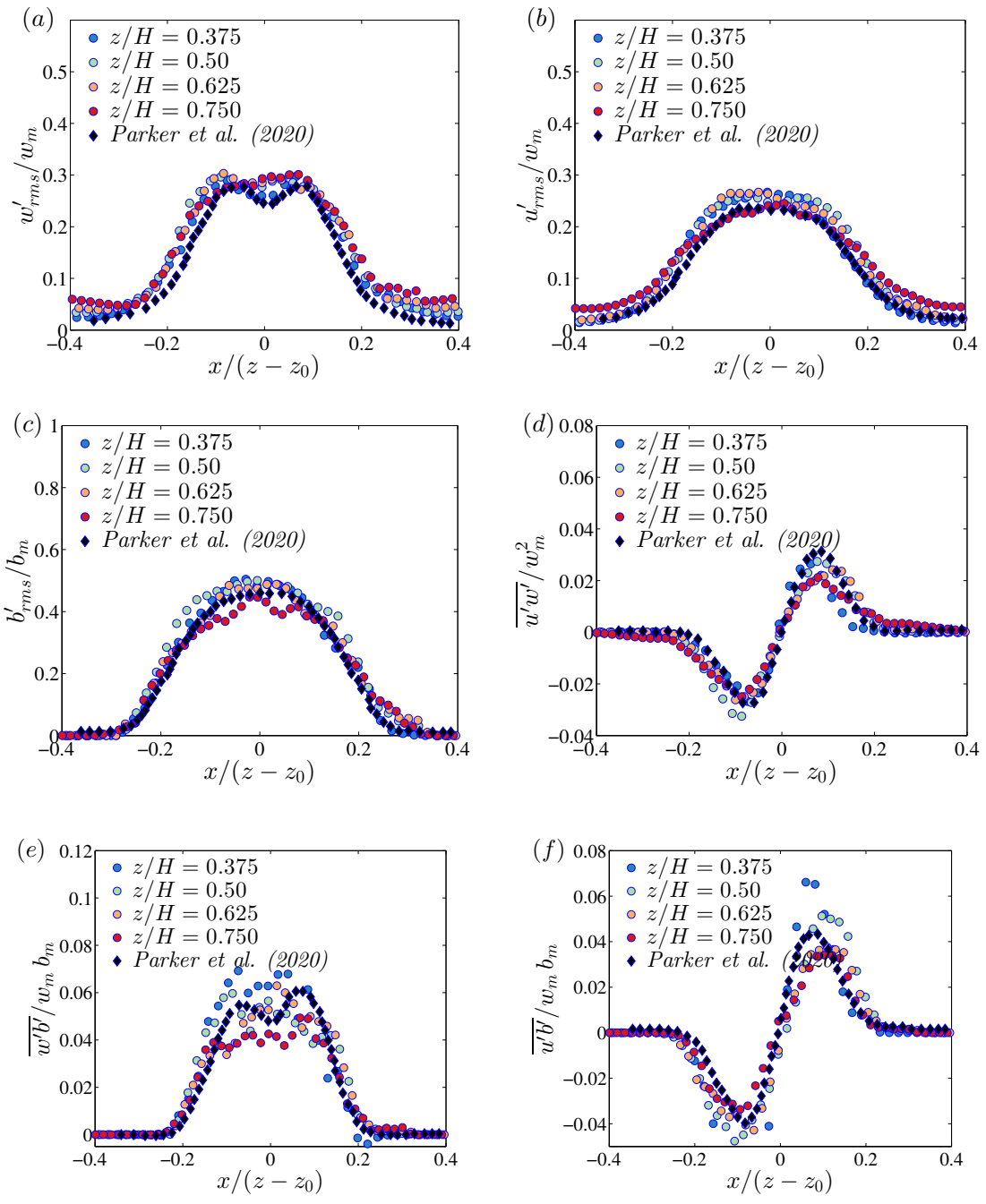

FIGURE 7.1: Time-averaged confined line plume turbulent fluctuations of (a) vertical velocity, (b) horizontal velocity, (c) buoyancy, (d) Reynolds stress, (e) vertical and (f) horizontal buoyancy flux for $Re_H = 7200$ and $L/H = 2$ case.

plume axis, however, actually increases slightly during the latter stages of development of the turbulent plumes. The presence of the dip in streamwise velocity fluctuations near the axis of the axis of the self-similar region is similar to the behaviour of the round buoyant turbulent plumes (Shabbir and George 1994), and

is expected because turbulence production is reduced near the axis due to symmetry. For the horizontal RMS velocities, in 7.1 (b), a self-similar collapse occurs near $z/H \approx 0.375$, with a peak value of approximately 0.22 at $z/H = 0.625$ and eventually collapse to a self-similar profiles, with centreline values of 0.25. Hussein et al. (1994) and Shabbir and George (1994) found very similar values, 0.2 and 0.19 respectively, while Panchapakesan and Lumley (1993) and Papanicolaou and List (1988) found slightly lower values of 0.17 and 0.15 respectively for turbulent buoyant round jets. In figure 7.1 (d), we plot the cross-sectional variation of normalised Reynolds shear stress at various downstream locations. The profiles achieve self-similarity after $z/H \approx 0.375$. The profile go to 0 at the origin and reach peak value that are 2.8% of the mean vertical velocity. Parker et al. (2020) found peak fluctuations of 0.025.

Figure 7.1 (e) and (f) show the cross-sectional variation of vertical and horizontal turbulent buoyancy flux, respectively. An off-axis peak normalised horizontal turbulent buoyancy flux is observed, $\overline{u'b'}$ that ranges between $0.035 - 0.042$. These results compare well to Parker et al. (2020), who observed a peak value of 0.041. The self - similar profiles of vertical turbulent buoyancy flux, $\overline{w'b'}$ have the centreline values of approximately 0.05.

7.1.2 Confined-line plumes in asymptotic state

Figure 7.2 show the time-averaged confined line plume turbulent fluctuations of vertical velocity, horizontal velocity, buoyancy, Reynolds stress, vertical and horizontal buoyancy flux for $Re_H = 7200$ and $L/H = 2$ case, where the subscript rms denotes the root mean square of the data. The turbulent fluctuations are normalised by plume centreline quantities. To our knowledge, turbulent quantities for a confined line plume have not been calculated in previous studies. The turbulent fluctuations of vertical velocity (figure 7.2 a) exhibit a collapse on to a single curve near the plume centreline and the maximum value of $w'_{rms}/w_m = 0.35$ occurs close to the plume boundary. It can be seen that the maximum value of w'_{rms} is much higher than that of line plumes in an open environment. The fluctuations of horizontal velocity components show little scatter for different vertical locations of the confined plume. Near the side walls, the normalised root mean square profiles of vertical velocity, horizontal velocity and buoyancy are deviated from the self-similar. In figure 7.2 (d), we plot the cross-sectional variation of

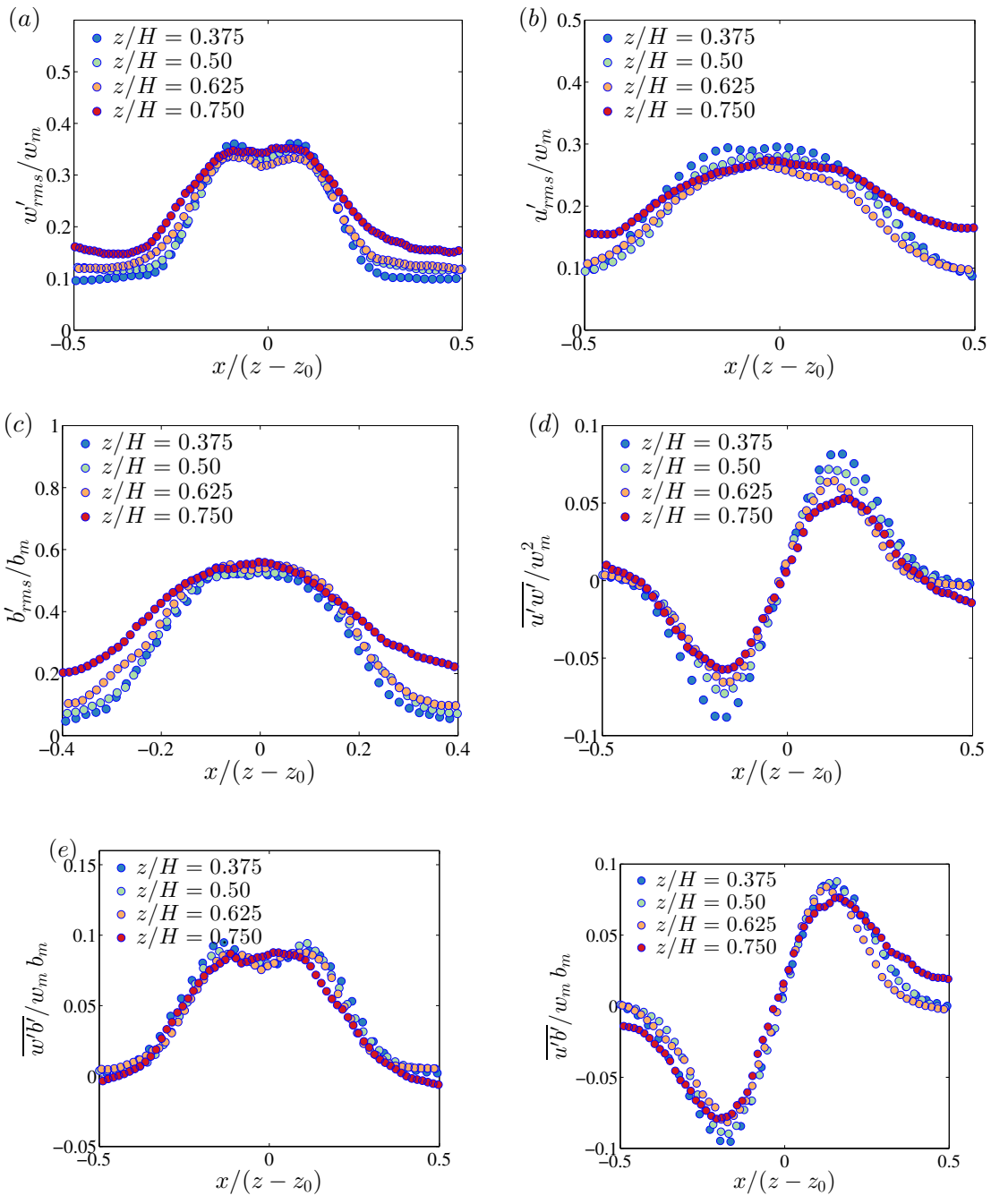

FIGURE 7.2: Time-averaged confined line plume turbulent fluctuations of (a) vertical velocity, (b) horizontal velocity, (c) buoyancy, (d) Reynolds stress, (e) vertical and (f) horizontal buoyancy flux for $Re_H = 7200$ and $L/H = 2$ case.

normalised Reynolds shear stress at various downstream locations. The peal value of Reynolds stress were found to be about 0.08, which much higher than in the case of free line plumes (0.024).

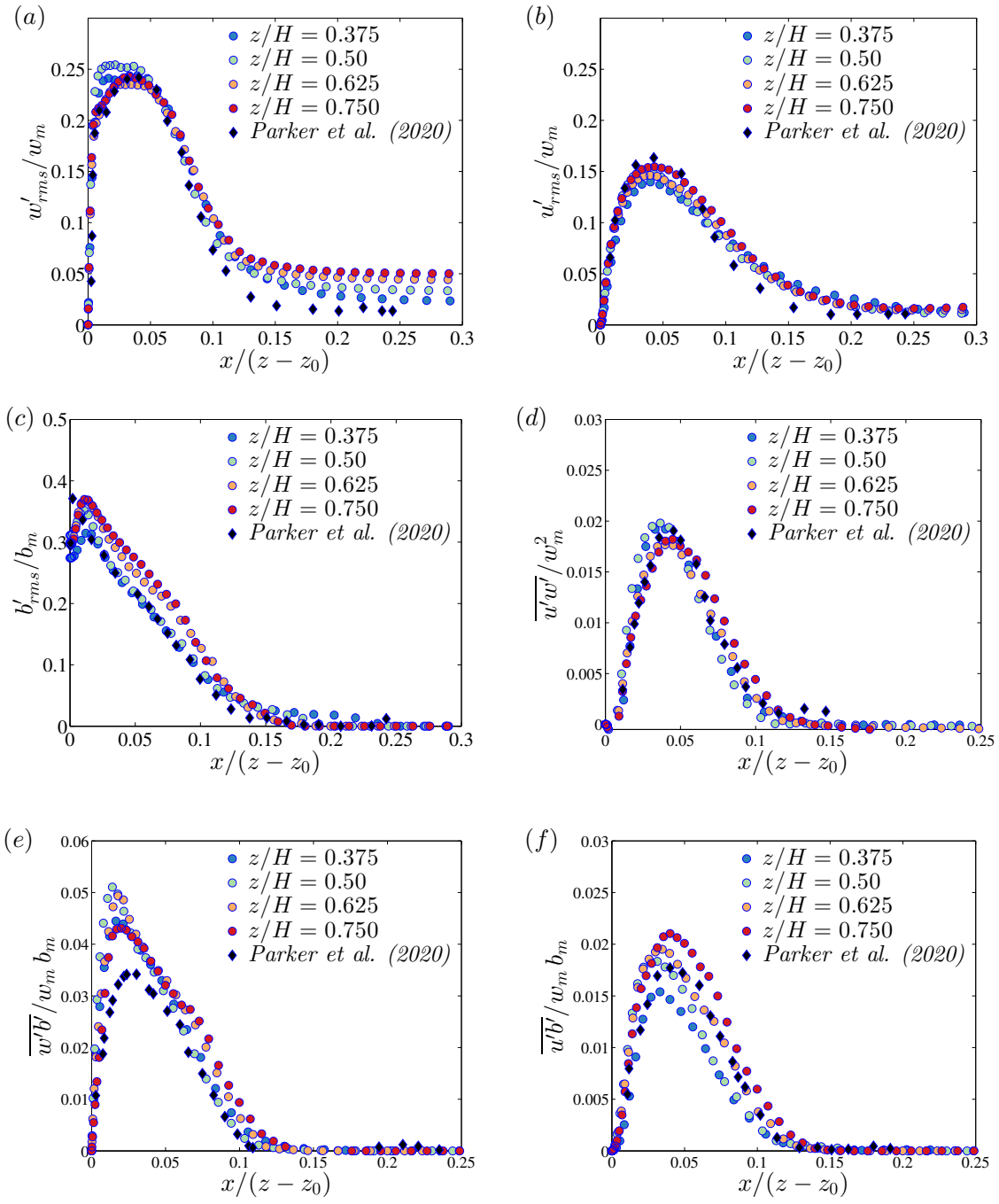

FIGURE 7.3: Time-averaged wall-attached line plume turbulent fluctuations of (a) vertical velocity, (b) horizontal velocity, (c) buoyancy, (d) Reynolds stress, (e) vertical and (f) horizontal buoyancy flux for $Re_H = 14530$ and $L/H = 2$ case. The black diamonds symbol represents data from Parker et al. (2020).

7.1.3 Wall-attached line plumes

Figure 7.3 shows time-averaged wall-attached line plume turbulent fluctuations of vertical velocity, horizontal velocity, buoyancy, Reynolds stress, vertical and

horizontal buoyancy flux for $Re_H = 14530$ and $L/H = 2$ case. The black diamond symbols in figure 7.3 represent data from Parker et al. (2020). The measurements of Parker et al. (2020) are close to the results from DNS for all turbulent quantities. The maximum value of normalised rms quantity of vertical velocity fluctuations, w_{rms}/w_m is 0.27, which is located at $x/(z - z_0) \approx 0.045$. Measurements of Parker et al. (2020) corresponds to a peak value of 0.24. The turbulent fluctuations of horizontal velocity (figure 7.3 b) exhibit a good collapse on to a single curve and the maximum value of $u'_{rms}/w_m = 0.15$ occurs close to the plume boundary. The fluctuations of buoyancy component (figure 7.3 c) , vertical (figure 7.3 e) and horizontal buoyancy flux (figure 7.3 f) show little scatter for different vertical locations of the wall plume. The far-field peak values of the turbulent intensities from the present study and from select past studies have been summarised in 7.1.

Study	$\overline{b'b'}$	$\overline{u'b'}$	$\overline{w'b'}$	$\overline{u'u'}$	$\overline{w'w'}$	$\overline{u'w'}$
Free line plume	0.4 - 0.45	0.035-0.042	0.04 -0.06	0.22 -0.24	0.25 - 0.3	0.022 - 0.024
Confined line plume	0.52 -0.53	0.05 -0.07	0.08 -0.09	0.25 -0.3	0.3 - 0.35	0.05 -0.08
Wall-attached plume	0.34 -0.38	0.018 -0.022	0.042 -0.05	0.14 - 0.16	0.24 -0.26	0.018 -0.022
Parker et al. (2020) (Free line plume)	0.43	0.041	0.05	0.21	0.3	0.025
Parker et al. (2020) (Wall-attached line plume)	0.38	0.017	0.035	0.16	0.24	0.019
Hussein et al. (1994)	-	-	-	0.2	0.25	0.02
Shabbir and George (1994)	-	-	-	0.19	0.32	0.09
Panchapakesan and Lumley (1993)	-	-	0.05	0.17	0.25	-
Wang and Law (2002)	0.4	0.035	0.05	0.153	0.236	0.021
Papanicolaou and List (1988)	-	-	-	0.15	0.25	-

TABLE 7.1: Summary of 2nd order statistics

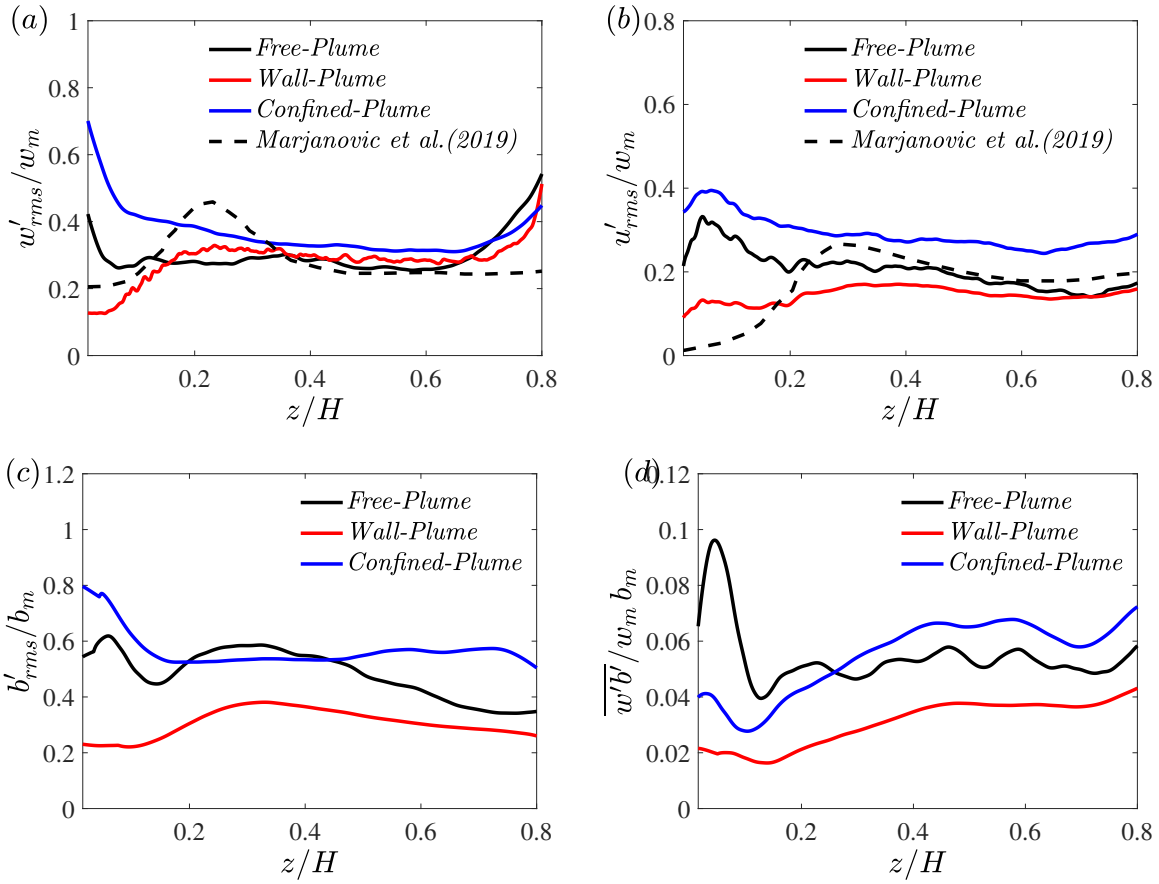

FIGURE 7.4: Streamwise variation of (a) w_{rms}, (b) u_{rms}, (c) b_{rms} and (d) $\overline{u'b'}$ normalised by the centreline buoyancy, b_m, and/or the centreline vertical velocity, w_m for free, wall-attached and confined free-line plumes in asymptotic state. Note that in the horizontal axis, z/H started at 0.0156.

Figure 7.4 compares the plume centreline turbulent intensity in streamwise direction, along the flow axis of the free, wall-attached and confined line plumes. The DNS results of Marjanovic et al. (2017) for a free turbulent round plume also considered for comparison. The centreline turbulent intensity of the free and confined turbulent line plume, evolve in a similar manner. The variation of turbulent intensity in the case of confined line plume exhibit higher magnitude compared to other cases. There are many experimental results for jets, forced plumes and pure plumes but none in the lazy regime for the turbulent line plumes. However, we still observe a good comparison to our lazy line plume results away from the walls.

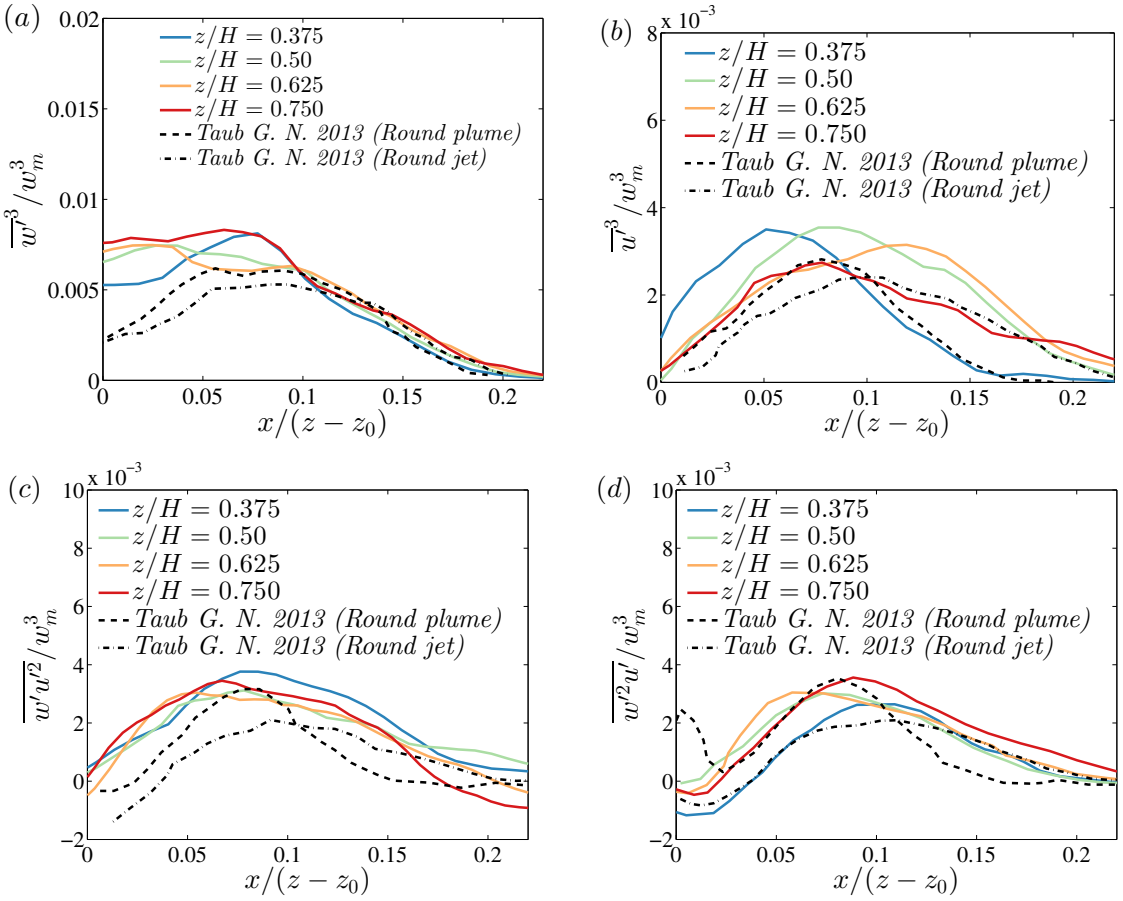

FIGURE 7.5: Cross-sectional profiles of the third order velocity statistics for the free line plume.

7.2 3rd order statistics

Third order moments are important because they provide information about turbulent diffusion in the turbulent kinetic energy balance, which is responsible for redistributing energy from the pressure and turbulent fields. In figure 7.5, we plot the cross-sectional variations of normalised third order moments for the case of free line plume. In figure 7.5(a), we plot the vertical transport of vertical component of Reynolds stress, $\overline{w'^3}$. The peak values observed from the DNS simulation of Taub (2013) round plume and jet are much lower values compared to the free line plume. The profiles are strictly positive even at the centre line with higher peaks values in general. The horizontal transport of horizontal Reynolds stress is plotted in 7.5 (b). There is no clear collapse to a self-similar profile, even after $z/H = 0.375$. The horizontal transport of the vertical Reynolds stress is plotted in figure 7.5(c). The profiles are mostly positive near centreline. The peak values

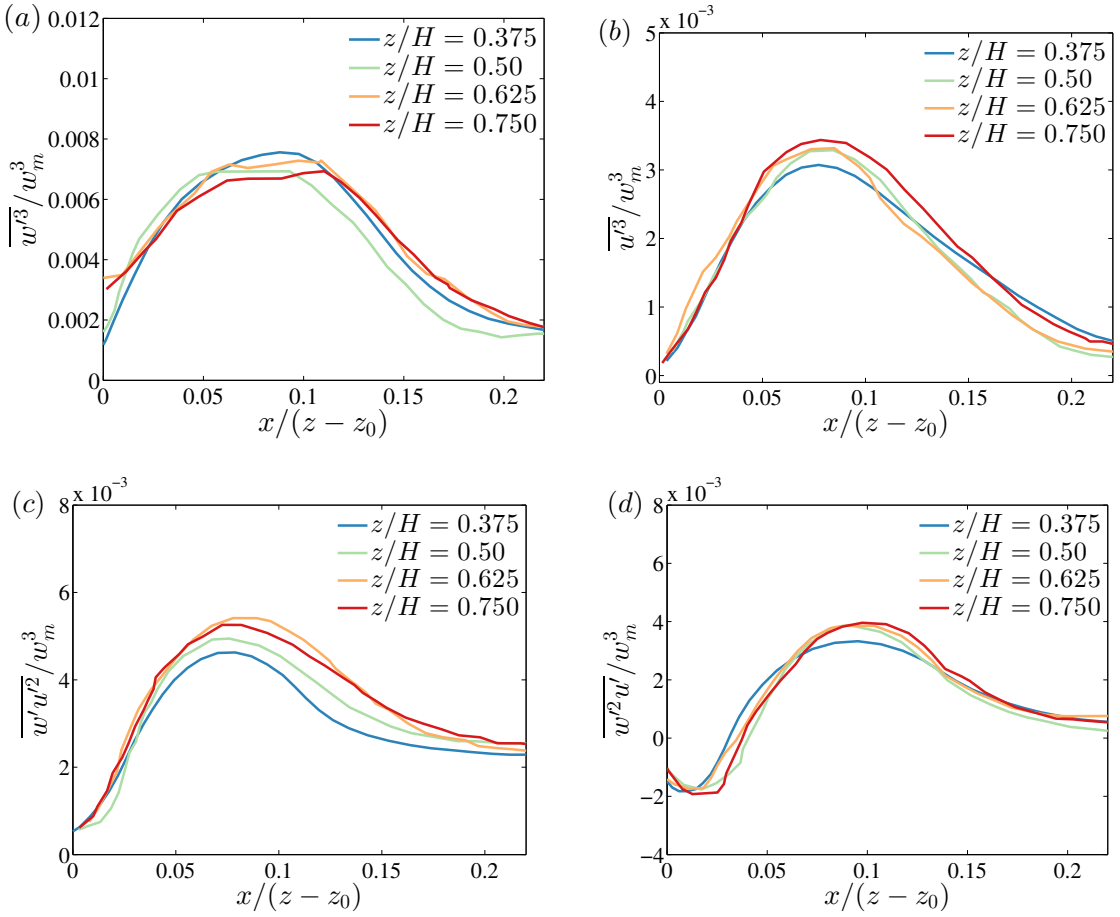

FIGURE 7.6: Cross-sectional profiles of the third order velocity statistics for the confined line plume.

ranges between 0.003 and 0.004. The cross-sectional variation of the normalised vertical transport of horizontal Reynolds stress, figure 7.5(d), exhibits some negative centreline values far downstream. In general, the profiles are positive and have peaks that vary between 0.0025 and 0.004.

In figures 7.6, we plot the cross-sectional variations of normalised third order velocity moments, respectively for confined line plumes. The vertical transport of vertical Reynolds stress is plotted in figure 7.6 (a). A slightly wider profile than the free line plume case is observed, with higher peak values between 0.0065 and 0.0078 occurring between $x/(z - z_0) \approx 0.06$ and 0.12. The profiles remain positive, even near the centreline. The horizontal transport of horizontal Reynolds stress is plotted in 7.6 (b). Here we note narrower profiles and larger peak values compared to free plumes, between 0.0029 and 0.0034.

Figure 7.7 shows the cross-sectional profiles of the third order moments of velocity

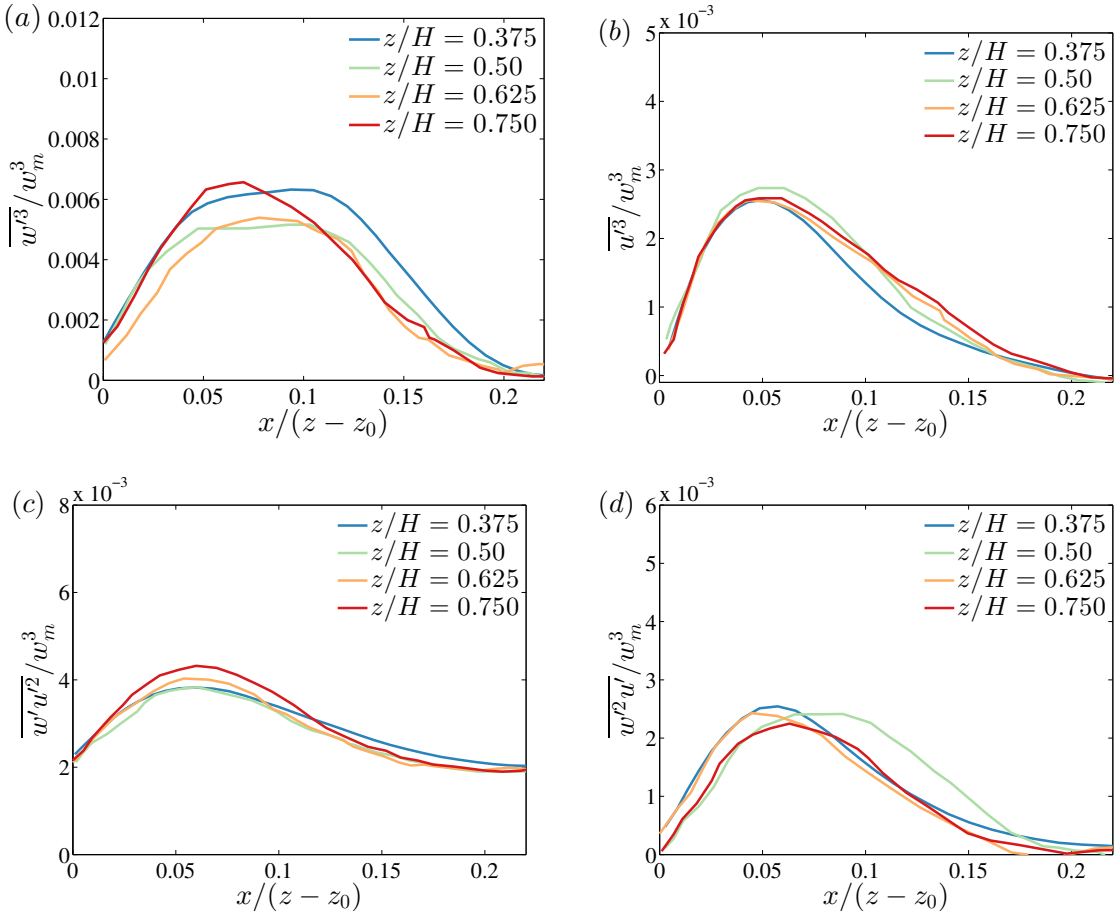

FIGURE 7.7: Cross-sectional profiles of the third order velocity statistics for the wall-attached line plume.

of the wall plumes in the current study at different z/H locations. The third order velocity profiles for the free line plumes and wall plumes have similar behaviour. The cross-sectional variation of vertical transport of horizontal Reynolds stress, figure 7.7 (d), exhibit positive values at the centreline, whereas larger negative value is observed for free and confined line plumes.

7.3 Turbulent kinetic energy balance

By performing Reynolds decomposition of the momentum equations, subtracting off the RANS equations, taking the dot products with the fluctuating velocity vector and taking the average, the transport equation for turbulent kinetic energy,

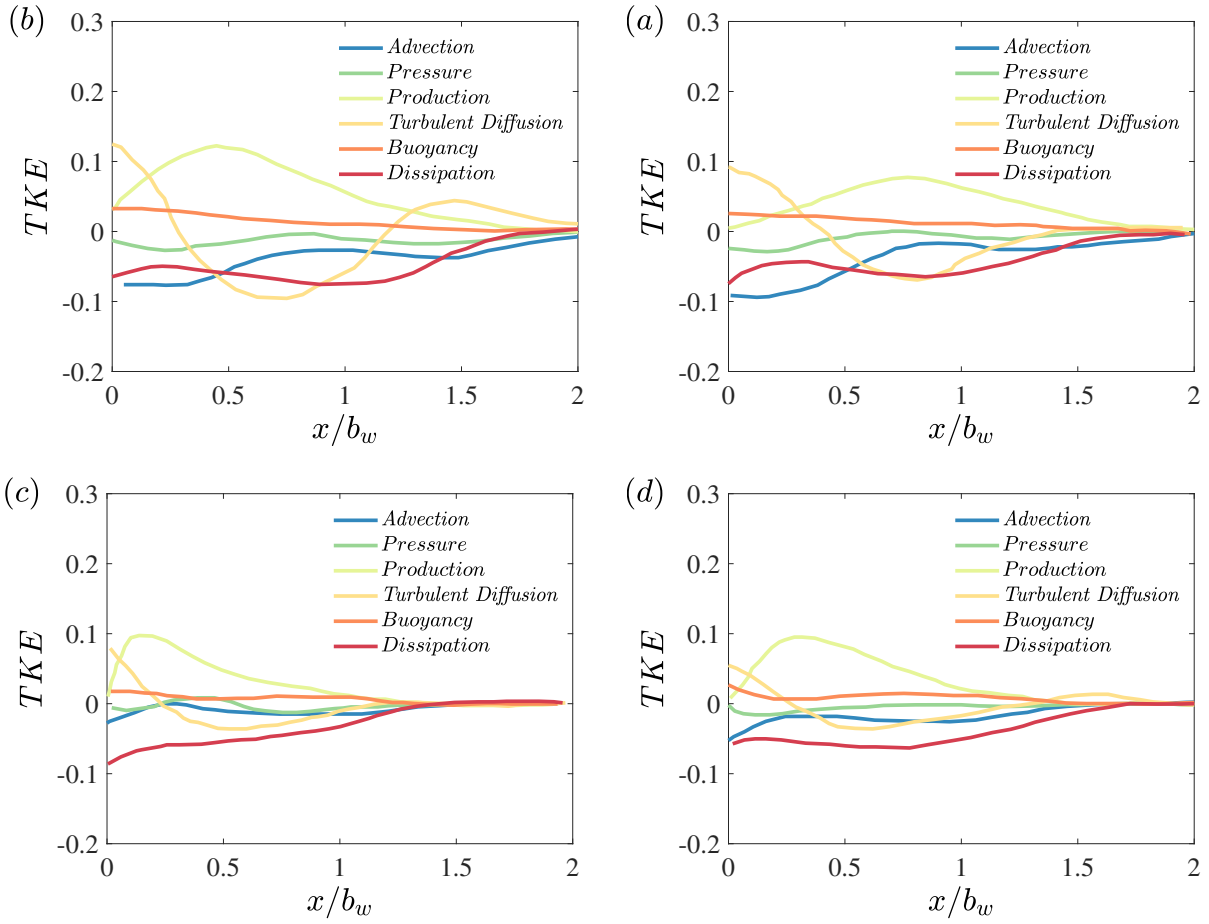

FIGURE 7.8: Turbulent kinetic energy balance of a free line plume at (a) $z/H = 0.5$ and (b) $z/H = 0.625$ for $Re_H = 7200$ and a wall-attached plume at (c) $z/H = 0.5$ and (d) $z/H = 0.625$ for $Re_H = 14530$.

k, can be derived as:

$$0 = -\underbrace{\overline{u}_j \frac{\partial k}{\partial x_j}}_{Advection} \underbrace{-\frac{1}{\rho}\frac{\partial \overline{u_i' p'}}{\partial x_i}}_{Pressure\ diffusion} - \underbrace{\frac{1}{2}\frac{\partial \overline{u_j' u_j' u_i'}}{\partial x_i}}_{Turbulent\ diffusion} - \underbrace{\overline{u_i' u_j'}\frac{\partial \overline{u_i}}{\partial x_j}}_{Production} - \underbrace{\nu \overline{\frac{\partial u_i'}{\partial x_j}\frac{\partial u_i'}{\partial x_j}}}_{Pseudo\text{-}dissipation} - \underbrace{g\beta \overline{u_i'}\delta_{i3}}_{Buoyancy\ flux}. \tag{7.1}$$

Equation (7.1) is also referred to as the turbulent kinetic energy balance (cf. Pope 2001). Here

$$k = \frac{1}{2}(\overline{u'^2} + \overline{v'^2} + \overline{w'^2}), \tag{7.2}$$

is the turbulent kinetic energy. Figure 7.8 shows the turbulent kinetic energy balance of the free line plume for $Re_H = 7200$ (a and b) and wall-attached plume

for $Re_H = 14530$ (c and d) at $z/H = 0.5$ and $z/H = 0.625$. All the terms of turbulence energy balance are non-dimensionalised using the maximum vertical velocity of the plume, w_m and vertical distance, z, and the horizontal axis is non-dimensionalised using plume half-width, b_w.

Turbulent kinetic energy balance of the free line plumes appears fairly similar at both vertical distances with the exception of production and diffusion terms very near the plume centreline. For the free and wall-attached line plumes, in figure 7.8, dissipation and advection act as sinks and are balanced by buoyancy, turbulent diffusion and pressure diffusion. Away from the centreline production is balanced by advection, dissipation and turbulent diffusion. A slightly narrower horizontal profiles were observed for wall-attached plume case. Also, all the terms in turbulent kinetic energy balance decay to approximately 0 at $x/b_w \approx 1.5$, whereas the profile continue well until $x/b_w \approx 2.0$ for free line plumes.

The advection profile of the free line plume is strictly negative for all x/b_w, the term becomes close to 0 at $x/b_w \approx 0.4$ for wall-attached plumes. In the free plume case, the production term near the plume axis is greater than that of a wall-attached plume. The other terms in the turbulent kinetic energy balance all have roughly same shape and magnitudes for both free and wall-attached plumes.

The buoyancy plays a significant role in plumes, but the buoyancy term in the kinetic energy balance is smaller the production term for both plume cases. This suggests that the turbulence is maintained by the gradient production not by buoyancy (Shabbir and George 1994).

7.4 Chapter summary

Turbulent statistics of free, wall-attached and confined line plumes are analysed using direct numerical simulations. The data is collected over enough time steps for second and third order statistics to converge after each simulation became statistically steady. Second order statistics from the DNS of free and wall-attached are compared with the experimental data from Parker et al. (2020). The measurements of Parker et al. (2020) are close to the results from DNS for all turbulent quantities. The turbulent quantities for a confined line plume have not been calculated in previous studies. It is observed that the maximum value of w'_{rms} is much higher than that of line plumes in an open environment. The fluctuations of

horizontal velocity components show little scatter for different vertical locations of the confined plume. Near the side walls, the normalised root mean square profiles of vertical velocity, horizontal velocity and buoyancy deviate slightly from the self-similar.

Third order velocity profiles are calculated and examined at different vertical distances from the source for free, wall-attached and confined line plumes. The third order statistics of the free line plume are compared with the round plume and jet data of Taub (2013). The peak values observed from the DNS simulation of Taub (2013) round plume and jet are much lower values compared to the free line plume.

Chapter 8

The entrainment in the wall and free plumes

The value of the entrainment coefficient, α, for the wall attached plumes is observed to be much less as compared with free line plumes. In this chapter, a thorough investigation is conducted on the deficit in α for wall plumes using an entrainment model that is developed following the works of van Reeuwijk and Craske (2015), for axisymmetric plumes, and Krug et al. (2017), for planar buoyant wakes .

8.1 Theoretical model for entrainment coefficient

van Reeuwijk and Craske decomposes the entrainment coefficient into contributions from the production of turbulent kinetic energy, the plume Richardson number Ri and the profile coefficients associated with the shape of buoyancy and velocity profiles. Here, we extend the model, which was developed for axisymmetric free turbulent jets and plume, to line plumes and wall plumes.

The continuity, Reynolds-averaged streamwise momentum and buoyancy equations are reconsidered as

$$\frac{\partial \overline{u}}{\partial x}+\frac{\partial \overline{w}}{\partial z}=0, \tag{8.1}$$

$$\frac{\partial}{\partial x}(\overline{uw}+\overline{u'w'})+\frac{\partial}{\partial z}(\overline{w}^2+\overline{w'^2})=-\frac{\partial \overline{p}}{\partial z}+\overline{\theta}+\nu\frac{\partial^2 \overline{w}}{\partial x^2}, \tag{8.2}$$

$$\frac{\partial}{\partial x}(\overline{u}\overline{\theta}+\overline{u'\theta'})+\frac{\partial}{\partial z}(\overline{w}\overline{\theta}+\overline{w'\theta'})=-N^2\overline{w}. \tag{8.3}$$

Here $\overline{\theta}=g\,\beta(\overline{T}-\overline{T}_\infty)$ is the mean buoyancy, where g is the gravitational acceleration, β is the coefficient of thermal expansion, $\overline{T}$ is the mean temperature and $\overline{T}_\infty$ is the mean environmental temperature. Also, u', w' and θ' are the fluctuating components of u, w and θ, respectively. The buoyancy frequency is defined as $N^2(z)=g\beta(\partial\overline{T}_\infty/\partial z)$.

The mean kinetic energy is obtained by multiplying (8.2) with $2\overline{w}$, after simplification, the final equation is

$$\begin{aligned}&\frac{\partial}{\partial x}(\overline{u}\,\overline{w}^2+2\overline{w}\,\overline{u'w'})+\frac{\partial}{\partial z}(\overline{w}^3+2\overline{w}\,\overline{w'^2}+2\overline{w}\,\overline{p})\\&=2\overline{u'w'}\frac{\partial \overline{w}}{\partial x}+2\overline{w'^2}\frac{\partial \overline{w}}{\partial z}+2\overline{p}\frac{\partial \overline{w}}{\partial z}+2\,\overline{w}\,\overline{\theta}+2\nu\overline{w}\,\frac{\partial^2 \overline{w}}{\partial x^2}.\end{aligned} \tag{8.4}$$

The first two terms of the above equation represent the horizontal and vertical transport terms. The term $2\overline{u'w'}(\partial\overline{w}/\partial x)+2\overline{w'^2}(\partial\overline{w}/\partial z)$ is associated with the production of turbulence kinetic energy. The term $2\overline{p}(\partial\overline{w}/\partial z)$ is a pressure redistribution term and $2\,\overline{w}\,\overline{\theta}$ represents the production of mean kinetic energy due to buoyancy.

8.1.1 Entrainment relations for wall plumes

The volume flux Q, momentum flux M, integral buoyancy B and buoyancy flux F for wall plumes are defined as

$$Q=\int_0^\infty \overline{w}\,\mathrm{d}x,\quad M=\int_0^\infty \overline{w}^2\,\mathrm{d}x,\quad B=\int_0^\infty \overline{\theta}\,\mathrm{d}x,\quad F=\int_0^\infty \overline{\theta}\,\overline{w}\,\mathrm{d}x. \tag{8.5}$$

Using Gaussian assumptions for the mean vertical velocity $\overline{w}$ and mean buoyancy $\overline{\theta}$, the fluxes can be express in terms of a maximum vertical velocity, $w_m(z)$ and

buoyancy, $\theta_m(z)$ along with a plume width, $b(z)$ as

$$Q = \frac{\sqrt{\pi}\, b\, w_m}{2}, \quad M = \frac{\sqrt{\pi/2}\, b\, w_m^2}{2}, \quad F = \frac{\sqrt{\pi/2}\, b\, w_m\, \theta_m}{2}. \tag{8.6}$$

Integration of (8.1)-(8.4) along the $x-$ direction gives

$$\frac{\mathrm{d}Q}{\mathrm{d}z} = \sqrt{2}\,\alpha\,\frac{M}{Q} \tag{8.7}$$

$$\frac{\mathrm{d}}{\mathrm{d}z}(\beta_g\, M) = \frac{F\, Q}{\eta_m\, M} - C_f \frac{M^2}{Q^2} \tag{8.8}$$

$$\frac{\mathrm{d}}{\mathrm{d}z}\left(\frac{\eta_g}{\eta_m}\, F\right) = -\, N^2\, Q \tag{8.9}$$

$$\frac{\mathrm{d}}{\mathrm{d}z}\left(\gamma_g\, \frac{M^2}{Q}\right) = \delta_g\, \frac{M^3}{Q^3} + 2F + 2\nu \int_0^\infty \overline{w}\, \frac{\partial^2 \overline{w}}{\partial x^2} \mathrm{d}x. \tag{8.10}$$

The parameters β, γ, η, and δ in (8.8)-(8.10) are profile coefficients associated with the dimensionless momentum flux, energy flux, buoyancy flux and turbulence production, respectively. The gross value of a profile coefficient, e.g. γ_g, is composed of contributions from the mean flow, turbulence and pressure, i.e. $\gamma_g = \gamma_m + \gamma_f + \gamma_p$. So, the profile coefficients are defined as

$$\begin{aligned}
\beta_m = \frac{M}{\sqrt{\pi/2}\, w_m^2\, b/2} = 1, \quad \beta_f &= \frac{1}{\sqrt{\pi/2}\, w_m^2\, b/2} \int_0^\infty \overline{w'^2}\, \mathrm{d}x, \\
\beta_p &= \frac{1}{\sqrt{\pi/2}\, w_m^2\, b/2} \int_0^\infty \overline{p}\, \mathrm{d}x, \\
\gamma_m = \frac{1}{\sqrt{\pi}\, w_m^3\, b/4} \int_0^\infty \overline{w}^3\, \mathrm{d}x, \quad \gamma_f &= \frac{2}{\sqrt{\pi}\, w_m^3\, b/4} \int_0^\infty \overline{w}\, \overline{w'^2}\, \mathrm{d}x, \\
\gamma_p &= \frac{2}{\sqrt{\pi}\, w_m^3\, b/4} \int_0^\infty \overline{w}\, \overline{p}\, \mathrm{d}x, \\
\delta_m = \frac{2}{w_m^3/(2\sqrt{2})} \int_0^\infty \overline{u'w'}\, \frac{\mathrm{d}\overline{w}}{\mathrm{d}x} \mathrm{d}x, \quad \delta_f &= \frac{2}{w_m^3/(2\sqrt{2})} \int_0^\infty \overline{w'^2} \frac{\mathrm{d}\overline{w}}{\mathrm{d}z}\, \mathrm{d}x, \\
\delta_p &= \frac{2}{w_m^3/(2\sqrt{2})} \int_0^\infty \overline{p}\, \frac{\mathrm{d}\overline{w}}{\mathrm{d}z} \mathrm{d}x, \\
\eta_m = \frac{F}{\sqrt{\pi/2}\, b\, w_m\, \theta_m/2}, \quad \eta_f &= \frac{1}{\sqrt{\pi/2}\, b\, w_m\, \theta_m/2} \int_0^\infty \overline{w'\theta'}\, \mathrm{d}x,
\end{aligned} \tag{8.11}$$

where,

$$b = \sqrt{\frac{2}{\pi}}\,\frac{Q^2}{M} \text{ and } w_m = \sqrt{2}\,\frac{M}{Q}.$$

Now, the relation for the entrainment constant α can be derived from (8.7), after simplification using (8.8) and (8.10),

$$\alpha = \frac{1}{\sqrt{2}}\frac{Q}{M}\frac{\mathrm{d}Q}{\mathrm{d}z} \tag{8.12}$$

$$= \underbrace{-\frac{1}{\sqrt{2}}\frac{\delta_g}{\gamma_g}}_{\alpha_{prod}} + \underbrace{\sqrt{2}Ri\left(\frac{1}{\beta_g} - \frac{\eta_m}{\gamma_g}\right)}_{\alpha_{Ri}} + \underbrace{\frac{1}{\sqrt{2}}\frac{Q^2}{M}\frac{\mathrm{d}}{\mathrm{d}z}\left(\ln\frac{\gamma_g}{\beta_g^2}\right)}_{\alpha_{shape}} \tag{8.13}$$

$$- \left(\underbrace{\frac{16}{\pi^{5/2}\gamma_g}\frac{\nu}{Q}\widetilde{\Gamma}(5/4) + \sqrt{2}\,C_f}_{\alpha_{viscous}}\right),$$

where $\widetilde{\Gamma}$ is the usual Gamma function: $\widetilde{\Gamma}(z) = \int_0^\infty t^{z-1}\mathrm{e}^{-t}\,\mathrm{d}t$, and Ri is the Richardson number, which is defined as

$$Ri = \frac{F\,Q^3}{M^3}. \tag{8.14}$$

The entrainment relation (8.13) consist of four parts, contribution from turbulent production α_{prod}, mean buoyancy α_{Ri}, changes in profile shape α_{shape} and related to the inner boundary layer process, denoted by $\alpha_{viscous}$.

8.1.2 Entrainment relations for free plumes

Similarly, the volume flux Q, momentum flux M, integral buoyancy B and buoyancy flux F for free line plumes are defined as

$$Q = \int_{-\infty}^{+\infty} \overline{w}\,\mathrm{d}x, \quad M = \int_{-\infty}^{+\infty} \overline{w}^2\,\mathrm{d}x, \quad B = \int_{-\infty}^{+\infty} \overline{\theta}\,\mathrm{d}x, \quad F = \int_{-\infty}^{+\infty} \overline{\theta}\,\overline{w}\,\mathrm{d}x. \tag{8.15}$$

Using Gaussian assumptions for the mean vertical velocity $\overline{w}$ and mean buoyancy $\overline{\theta}$, the fluxes can be express in terms of a maximum vertical velocity, $w_m(z)$ and

buoyancy, $\theta_m(z)$ along with a plume width, $b(z)$ as

$$Q = \sqrt{\pi}\, b\, w_m, \quad M = \sqrt{\pi/2}\, b\, w_m^2, \quad F = \sqrt{\pi/2}\, b\, w_m\, \theta_m. \tag{8.16}$$

Integration of (8.1)-(8.3) along the $x-$ direction gives

$$\frac{\mathrm{d}Q}{\mathrm{d}z} = 2\sqrt{2}\,\tilde{\alpha}\,\frac{M}{Q} \tag{8.17}$$

$$\frac{\mathrm{d}}{\mathrm{d}z}(\beta_g\, M) = \frac{F\, Q}{\eta_m\, M} \tag{8.18}$$

$$\frac{\mathrm{d}}{\mathrm{d}z}\left(\frac{\eta_g}{\eta_m}\, F\right) = -\, N^2\, Q \tag{8.19}$$

$$\frac{\mathrm{d}}{\mathrm{d}z}\left(\gamma_g\, \frac{M^2}{Q}\right) = \delta_g\, \frac{M^3}{Q^3} + 2F. \tag{8.20}$$

The profile coefficients $\beta, \gamma, \eta \text{and} \delta$ for free line plumes can be defined as

$$\begin{aligned}
\beta_m = \frac{M}{\sqrt{\pi/2}\, w_m^2\, b} = 1, \quad \beta_f &= \frac{1}{\sqrt{\pi/2}\, w_m^2\, b} \int_{-\infty}^{+\infty} \overline{w'^2}\, \mathrm{d}x, \\
\beta_p &= \frac{1}{\sqrt{\pi/2}\, w_m^2\, b} \int_{-\infty}^{+\infty} \overline{p}\, \mathrm{d}x, \\
\gamma_m = \frac{1}{\sqrt{\pi}\, w_m^3\, b/2} \int_{-\infty}^{+\infty} \overline{w}^3\, \mathrm{d}x, \quad \gamma_f &= \frac{2}{\sqrt{\pi}\, w_m^3\, b/2} \int_{-\infty}^{+\infty} \overline{w}\, \overline{w'^2}\, \mathrm{d}x, \\
\gamma_p &= \frac{2}{\sqrt{\pi}\, w_m^3\, b/2} \int_{-\infty}^{+\infty} \overline{w}\, \overline{p}\, \mathrm{d}x, \\
\delta_m = \frac{2}{w_m^3/(2\sqrt{2})} \int_{-\infty}^{+\infty} \overline{u'w'}\, \frac{\mathrm{d}\overline{w}}{\mathrm{d}x}\mathrm{d}x, \quad \delta_f &= \frac{2}{w_m^3/(2\sqrt{2})} \int_{-\infty}^{+\infty} \overline{w'^2}\, \frac{\mathrm{d}\overline{w}}{\mathrm{d}z}\, \mathrm{d}x, \\
\delta_p &= \frac{2}{w_m^3/(2\sqrt{2})} \int_{-\infty}^{+\infty} \overline{p}\, \frac{\mathrm{d}\overline{w}}{\mathrm{d}z}\mathrm{d}x, \\
\eta_m = \frac{F}{\sqrt{\pi/2}\, b\, w_m\, \theta_m}, \quad \eta_f &= \frac{1}{\sqrt{\pi/2}\, b\, w_m\, \theta_m} \int_{-\infty}^{+\infty} \overline{w'\theta'}\, \mathrm{d}x,
\end{aligned} \tag{8.21}$$

where,

$$b = \frac{1}{\sqrt{2\pi}}\, \frac{Q^2}{M} \,\text{and}\, w_m = \sqrt{2}\, \frac{M}{Q}.$$

Now, the entrainment relation for the free line plume can be defined as

$$\widetilde{\alpha} = \frac{1}{2\sqrt{2}} \frac{Q}{M} \frac{\mathrm{d}Q}{\mathrm{d}z} \tag{8.22}$$

$$= \underbrace{-\frac{1}{2\sqrt{2}} \frac{\delta_g}{\gamma_g}}_{\widetilde{\alpha}_{prod}} + \underbrace{\frac{Ri}{\sqrt{2}} \left(\frac{1}{\beta_g} - \frac{\eta_m}{\gamma_g} \right)}_{\widetilde{\alpha}_{Ri}} + \underbrace{\frac{1}{2\sqrt{2}} \frac{Q^2}{M} \frac{\mathrm{d}}{\mathrm{d}z} \left(\ln \frac{\gamma_g}{\beta_g^2} \right)}_{\widetilde{\alpha}_{shape}}. \tag{8.23}$$

8.2 Comparison of the entrainment coefficient with the help of DNS results

The detailed description for the decomposition of entrainment relations for wall and free line plumes are given in the previous sections. The comparison of entrainment coefficients for these types of plumes with the help of DNS results is explained in this section. Figure 8.1 (a) and (b) show the vertical variations of the individual components in the entrainment relation for the wall and free plumes, respectively. The mean values of each term in (8.13) and (8.23) in the uniform environment for wall and free plumes are obtained using the procedures explained in sections 6.3.1.2 and appendix A. The entrainment relation for the wall (8.13) and free (8.23) plumes consists of three parts; the first part is the ratio of dimensionless turbulence production term δ_g and the dimensionless energy flux γ_g and which is denoted by α_{prod} (dashed black lines in figure 8.1). The second part is the net effect of buoyancy on the entrainment coefficient, denoted by α_{Ri} (dashed red lines in figure 8.1). The third part is related to the changes in profile shape along the vertical direction, which is indicated by α_{shape} (dashed blue lines in figure 8.1). Here, the symbol $\widetilde{(\cdot)}$ denotes parameters for free line plumes. The solid black lines in figure 8.1 indicate the summation of all three individual terms in the entrainment relation, i.e. $\sum \alpha = \alpha_{prod} + \alpha_{Ri} + \alpha_{shape}$. The black open circles indicate the entrainment coefficient calculated from the volume flux relations, (8.12) for wall plumes and (8.22) for free plumes. The decomposition of the production terms in the entrainment equation for the free and wall plumes and shown in figure 8.2. The term δ_m/γ_g in the free plume is approximately four times larger than the wall plume case, while the γ_g for both cases are approximately equal. In figure 7.8, the area under the curve in the productions terms are approximately equal to the δ_m. The area under the curve for free plumes in figure 7.8 (a) is larger

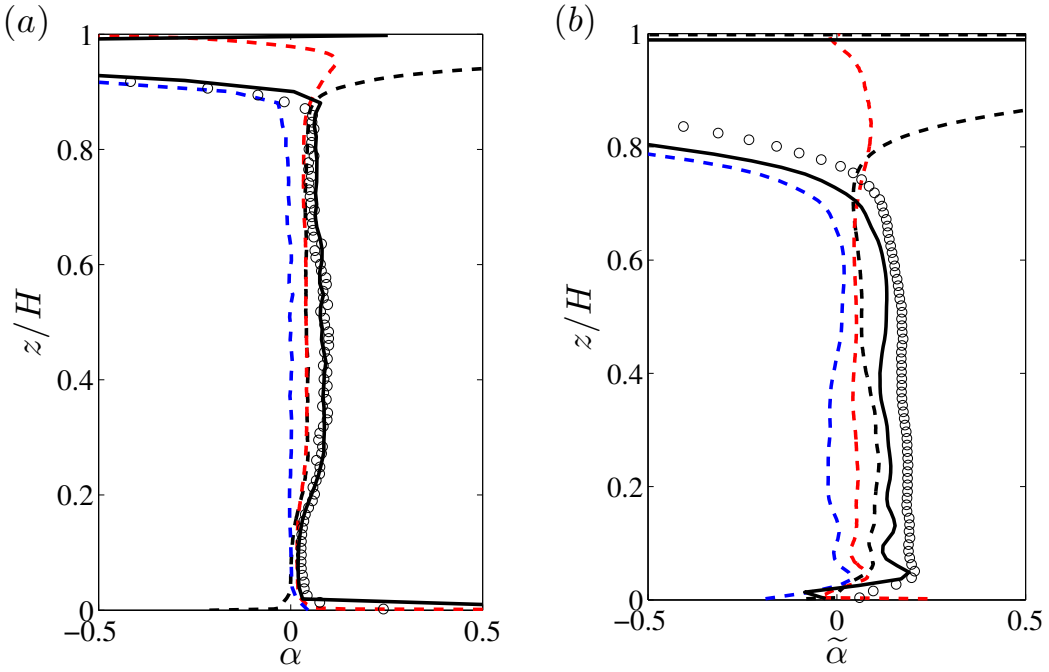

FIGURE 8.1: Vertical variations of the contribution to entrainment due to turbulent kinetic energy production α_{prod} (dashed black lines), buoyancy α_{Ri} (dashed red lines) and changes in profile shape α_{shape} (dashed blue lines) for wall plumes (a) and free line plumes (b). Here, $\widetilde{(\cdot)}$ denotes parameters for free line plumes. Solid black lines indicate the summation of all the individual contributions for the entrainment coefficient α and black open circles indicate the entrainment coefficient calculated from the volume flux relations, (8.12) for wall plumes and (8.22) for free plumes.

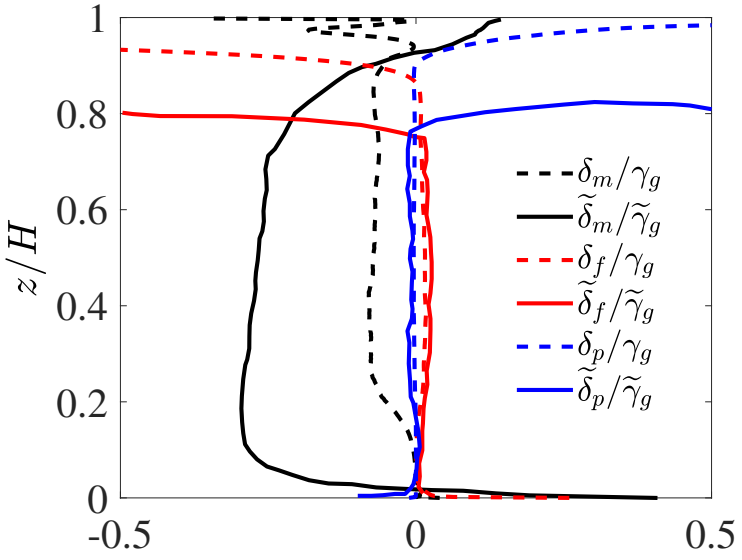

FIGURE 8.2: Decomposition of production terms in the entrainment equation for the free and wall plumes. $\widetilde{(\cdot)}$ terms denote free plume components.

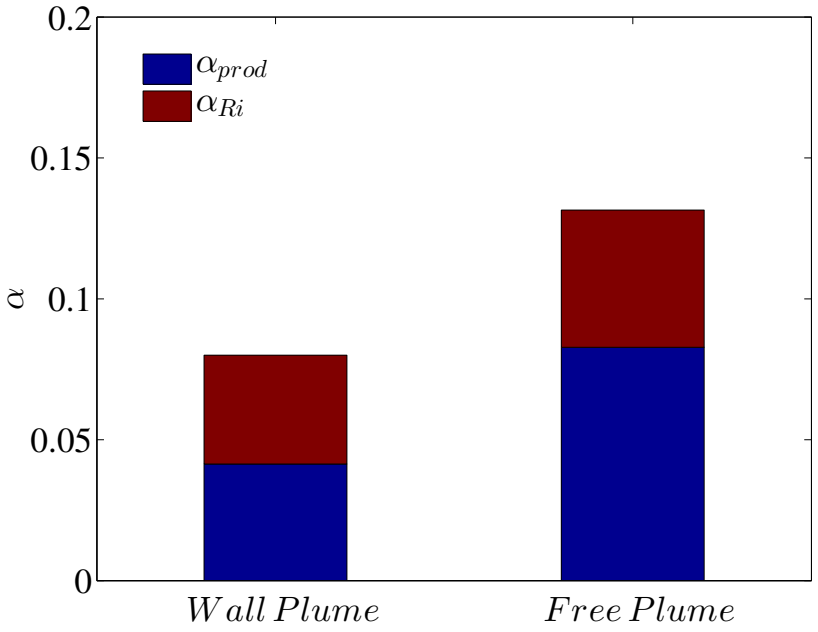

FIGURE 8.3: Comparison of individual terms in the entrainment relations (8.13) and (8.23) for wall and free line plumes, respectively. The terms α_{prod} and α_{Ri} are found by averaging in the region $0.2 \leq z/H \leq 0.7$ from figure 8.1.

compared to figure 7.8 (c) for wall plumes. This indicates that wall suppresses the production of turbulent kinetic energy in the case of wall plumes..

The graphical representation of individual terms in the entrainment relations (8.13) and (8.23) for wall and free line plumes is shown in figure 8.3. The terms α_{prod} and α_{Ri} in figure 8.3 are obtained by averaging in the region $0.2 \leq z/H \leq 0.7$ from figure 8.1. From figure 8.3, it is observed that the contribution to entrainment due to turbulent kinetic energy production α_{prod} and the net buoyancy contribution α_{Ri} are almost equal in magnitude for wall plumes in the uniform environment. However, in the case of free line plumes, α_{prod} is almost two times larger than α_{Ri}. Another interesting fact is that the term α_{Ri} is nearly equal in magnitude for both plumes, but the term α_{prod} appears to be approximately two times larger in free plumes compared to wall plumes. This may be because the wall suppresses the production of turbulent kinetic energy for wall plumes. Therefore, the total entrainment coefficient for the wall plumes became less compared to free plumes.

8.3 Chapter summary

In this chapter, a mathematical model for the entrainment coefficient α has developed for free and wall plumes in an open environment based on the works of van Reeuwijk and Craske (2015) and Krug et al. (2017). The entrainment relation consists of three different parts, i.e. contribution from the turbulent kinetic energy, net buoyancy and changes in profile shape. The individual components in the entrainment relations are obtained with the help of DNS data and it was found that the contribution from the turbulent kinetic energy on the entrainment for wall plumes is small compared with the free plumes due to the effect of the wall.

Chapter 9

Conclusions

In this final chapter, the key conclusions of the work presented in this thesis are considered. The significant and novel findings from the previous chapters are highlighted.

The research work presented in this thesis contains numerical investigations of thermal line plumes in confined environments. In the first stage of thesis, a thermal line plume originating from a line heat source, located at the centre of the bottom wall was investigated using direct numerical simulation. The filling-box mechanism of confined plumes is divided into two states. First, the evolution of the buoyant fluid toward the asymptotic state. Transient behaviours are observed in this state. The second state is when the plume reaches the large-time asymptotic state. In the transient state, the downward propagation of buoyant fluid was compared with the filling-box model of Baines and Turner (1969) and it was found that there is good agreement with DNS data. The flapping and meandering phenomena were observed in the asymptotic state. These behaviours precluded a direct comparison with the analytical models of Baines and Turner (1969) and Barnett (1991). Therefore, a centreline alignment method was used to reduce the flapping and meandering behaviours of the thermal line plumes in the asymptotic state. All the analytical models were compared with the DNS data, both in transient and asymptotic state. An entrainment constant α equal to 0.2 was obtained from the DNS results and all the comparisons made with this value. In the asymptotic state, the Baines and Turner (1969)'s model showed good agreement with the centreline aligned DNS results of plume volume, momentum and buoyancy fluxes.

In the second stage of the project, the horizontal outflow from a thermal line plume after impinging onto the top wall was investigated. Different aspect ratio boxes were used to study the phenomenon of horizontal propagation of buoyant fluids in both uniform quiescent and stratified environments. A theoretical model has been developed for the horizontal outflow from a line plume by adapting the work of Kaye and Hunt (2007) for the round plumes. Two regimes were observed for the horizontal outflow in the uniform environment, namely, the jet-like regime and gravity current-like regime. The DNS results followed the scaling-laws for the front propagation from the theoretical model, and we obtained the constants of proportionality for the horizontal front movement by fitting curves to the DNS results. The relationship between horizontal front position and time obtained as $\phi = 1.2\, t_n^{2/3}$ in the jet like region and $\phi = 0.8\, t_n$ in the gravity current-like region, where $\phi = x/H$ and t_n is the non-dimensionalised time.

The evolution of wall attached turbulent line plumes was investigated in the third stage of the thesis. A theoretical model was developed for this configuration of confined plumes based on the filling-box model of Baines and Turner (1969). The effect of wall shear stress was incorporated in the model. The new theoretical model for the confined wall plumes were compared against the DNS results. An entrainment constant $\alpha = 0.07$ was obtained from the DNS results. Good agreement was observed with distribution of mean volume and momentum fluxes in the uniform environment. The time-dependent buoyancy profiles for two different aspect ration boxes showed moderate agreement with the model.

Finally, a detailed comparison of the entrainment in the wall and free plumes was made in the final part of the thesis. The value of the entrainment coefficient for the wall attached plumes was observed to be much less as compared with the free line plumes. A mathematical model for the entrainment coefficient was developed for both types of plumes based on the work of van Reeuwijk and Craske (2015), who studied the round plumes. The individual components in the entrainment relations were obtained with the help of DNS results. Due to the effect of wall, the turbulent kinetic energy production in the confined wall plumes was observed to be small compared to the free plume cases, resulting in a lower α in wall plumes compared to free plumes.

Appendix A

Turbulent line plume in a uniform environment

In this section, we compare the steady-state line plume data in a uniform environment with classical plume theory to validate present DNS. We begin by considering the integrals Q, M and F, which can be derived from the continuity equation, the Reynolds averaged momentum equation ($z-$ direction) and the energy equations within the Boussinesq approximation (equations A.1, A.2 and A.3, respectively). The governing equations are

$$\frac{\partial \overline{u}}{\partial x}+\frac{\partial \overline{w}}{\partial z}=0, \tag{A.1}$$

$$\frac{\partial \overline{u}\,\overline{w}}{\partial x}+\frac{\partial \overline{w}\,\overline{w}}{\partial z}+\frac{\partial \overline{u'w'}}{\partial x}+\frac{\partial(\overline{w'^2}-\overline{u'^2})}{\partial z}=g\beta(\overline{T}-\overline{T}_\infty), \tag{A.2}$$

$$\frac{\partial \overline{u}\,(\overline{T}-\overline{T}_\infty)}{\partial x}+\frac{\partial \overline{w}\,(\overline{T}-\overline{T}_\infty)}{\partial z}+\frac{\partial \overline{T'u'}}{\partial x}+\frac{\partial \overline{T'w'}}{\partial z}=-\overline{w}\frac{\partial \overline{T}_\infty}{\partial z}, \tag{A.3}$$

where u', w' and T' are the fluctuating components of u, w and T, respectively.

In equation (A.2), the $z-$ direction pressure gradient term is approximated as $\partial\overline{u'^2}/\partial z$ (see e.g. Tennekes and Lumley 1972).

After integrating equations (A.1), (A.2) and (A.3) across the line plumes with assumptions of Gaussian profiles for vertical velocity and buoyancy give

$$\frac{\mathrm{d}Q}{\mathrm{d}z} = 2\sqrt{2}\,\alpha\frac{M}{Q}, \tag{A.4}$$

$$\frac{\mathrm{d}M}{\mathrm{d}z} = \frac{FQ}{M}, \tag{A.5}$$

$$\frac{\mathrm{d}F}{\mathrm{d}z} = 0. \tag{A.6}$$

In the uniform environment, it is clear from (A.6) that $F = F_0 =$ constant, so the set of ordinary differential equations (A.4-A.6) can be solved in terms of F_0 and z, i.e.

$$F = F_0\,, Q = 2\alpha^{2/3}F_0^{1/3}z \,\text{and}\, M = \sqrt{2}\alpha^{1/3}F_0^{2/3}z. \tag{A.7}$$

In order to compare the theoretical predictions of (A.7) with present simulation, we used DNS results from $Re_H = 3600$ ($L/H = 1.0\,\text{and}\,R/H = 8.0$) case. The mean vertical velocity and buoyancy are obtained by averaging spatially along the $y-$ direction as well as averaging across the time instances during which the horizontal front travels from $x/H = \pm 0.5$ till $x/H = \pm 8$ (approximately 500 data samples in time). To compute the integrals over the $x-$ directions of the plume, we fitted a Gaussian curve to the vertical velocity profile at each z/H locations based on the maximum vertical velocity w_m and width b_w (width at which the vertical velocity has fallen to 1/e of its central value) and we defined the integration limit $\pm x_\infty$ such that $\overline{w}(\pm x_\infty, z) = w_m(z)/100$ from the fitted Gaussian curve, which ensures that the vertical environmental velocity is small relative to that of the plume.

Figure A.1 (a) shows the variation of entrainment coefficient α with regard to $z-$ direction in a uniform environment. It is calculated from the volume flux equation (A.4) i.e.

$$\alpha = \frac{1}{2\sqrt{2}}\frac{Q}{M}\frac{\mathrm{d}Q}{\mathrm{d}z} \tag{A.8}$$

and used central-difference scheme for $\mathrm{d}Q/\mathrm{d}z$. The black solid line in figure A.1 (a) is a linear fit with zero slope to the data from $z/H = 0.2$ to $z/H = 0.7$, which shows the value of entrainment coefficient $\alpha = 0.2$. This value of α is set to a fixed value and used for all calculations in the uniform and asymptotic case of line plumes. It is shown that the value of entrainment constant obtained here is

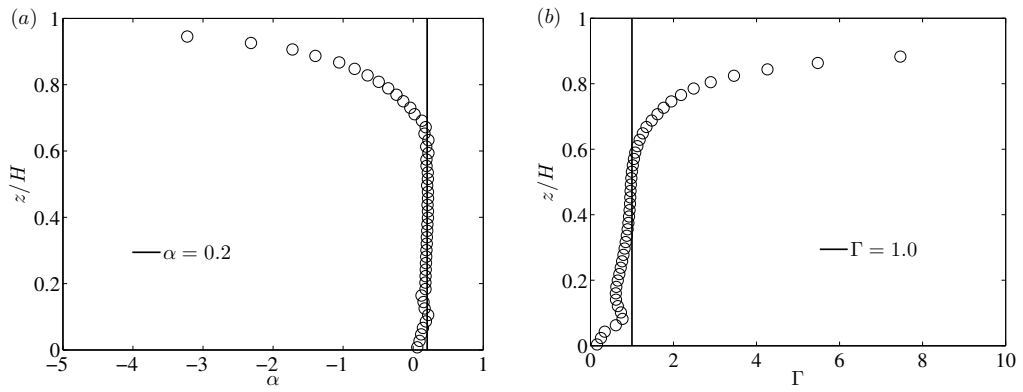

FIGURE A.1: Variation of average (a) entrainment coefficient α and (b) plume function Γ evaluated from the mean fluxes in a uniform environment.

much higher than in the case of axisymmetric plumes. The values of α reported in literatures for line plumes in a uniform environment are varying from 0.12 to 0.2, for example, $\alpha = 0.162$ for Rouse et al. (1952), $\alpha = 0.16$ for Lee and Emmons (1961) and $\alpha = 0.2$ for Kotsovinos (1975). The non-dimensional flux balance parameter for Gaussian profiles

$$\Gamma(z) = \frac{1}{2\sqrt{2}\,\alpha} \frac{Q^3(z)F(z)}{M^3(z)} \tag{A.9}$$

is plotted in figure A.1(b) with $\alpha = 0.2$. Based on the value of Γ at the source, $\Gamma_0 = \Gamma(0)$, the line plumes are characterised as forced plumes ($0 < \Gamma_0 < 1$), pure plumes ($\Gamma_0 = 1$) and lazy plumes ($\Gamma_0 > 1$). In the case of pure buoyancy driven thermal plumes, $\Gamma_0 = \infty$ but the value of Γ reaches pure plume behaviour immediately after the source. The solid black line in figure A.1(b) shows $\Gamma = 1$ (for pure plume case).

Figure A.2 (a), (b) and (c) show respectively the comparison of mean volume, momentum and buoyancy flux with theoretical models (A.7) in a uniform environment with $\alpha = 0.2$, respectively. The mean volume and momentum flux profiles show good agreement with the theoretical predictions. But the mean buoyancy flux profile represented by black circles in figure A.2 (c) show some deviation from the assumption of constant flux $F = F_0$ (black solid line). This discrepancy is due to the assumption of neglecting the fluctuating buoyancy flux in the energy equation (A.3). Therefore, we have added the fluctuating buoyancy flux into the

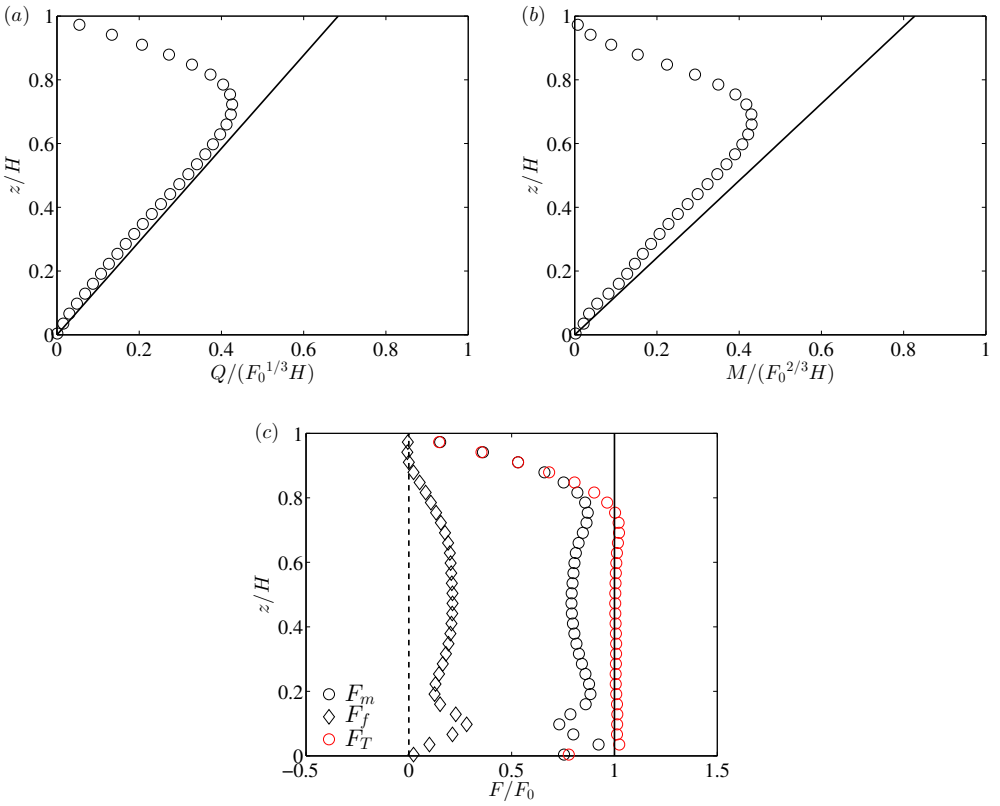

FIGURE A.2: Comparison of mean (a) volume, (b) momentum and (c) buoyancy flux with theoretical model in a uniform environment. The black circles represent the mean DNS results and black solid lines represent the theoretical model with $\alpha = 0.2$. The black diamond and red circle in (c) represent the fluctuating (F_f) and total buoyancy flux ($F_T = F_m + F_f$), respectively.

mean buoyancy flux as

$$F_T = \underbrace{\int_{-x_\infty}^{+x_\infty} g\beta\,(\overline{T} - \overline{T}_\infty)\,\overline{w}\,\mathrm{d}x}_{F_m} + \underbrace{\int_{-x_\infty}^{+x_\infty} g\beta\,\overline{T'w'}\,\mathrm{d}x}_{F_f}. \tag{A.10}$$

The total buoyancy flux F_T and fluctuating buoyancy flux F_f are shown in figure A.2 (c) with black diamonds and red circles, respectively. The total buoyancy flux F_T is now matched with constant source buoyancy flux F_0 upto $z/H \approx 0.8$, which is represented by solid black line in figure A.2 (c). The region $z/H > 0.8$ are influenced by the top confinement of the box. Therefore, the DNS results are valid only upto $z/H \approx 0.8$ for a line plume in a uniform environment case.

Appendix B

Numerical method for the theoretical models

This appendix provides details of the numerical solutions of the governing equations for different analytical models described in §4.3. Baines and Turner found a power series solution for the asymptotically large times when the plume volume, momentum and buoyancy fluxes no longer vary with time at a given height, but the plume and environmental temperature increases linearly in time at all heights. The accuracy of the power series solution was examined by comparing the numerical solution obtained using the routine ODE45 of MATLAB. Comparison of power series solution for the plume fluxes with ODE45 solution is shown in figure B.1. The figure B.1(a) shows the environmental buoyancy profiles with respect to time. The solid and dashed black lines in figures B.1 (b), (c) and (d) show the asymptotic solutions from ODE45 of MATLAB and power series, respectively. The power series solution for the plume buoyancy (figure B.1a) and volume flux (figure B.1c) are matched well with the ODE45 solution. However, some discrepancy is observed in the calculation of momentum flux (figure B.1d) near the top wall. This discrepancy may be due to the inaccuracy from the use of first three terms of the power series expansions of plume fluxes. Therefore, routine ODE45 of MATLAB is used for solving the governing equations in the Baines and Turner's analytical model described in §4.3.1.

For the Barnett's model, we considered Euler method for solving the governing equations because it is more convenient to solve complicated and tedious differential equations obtained from the theoretical models. We note that a very fine time

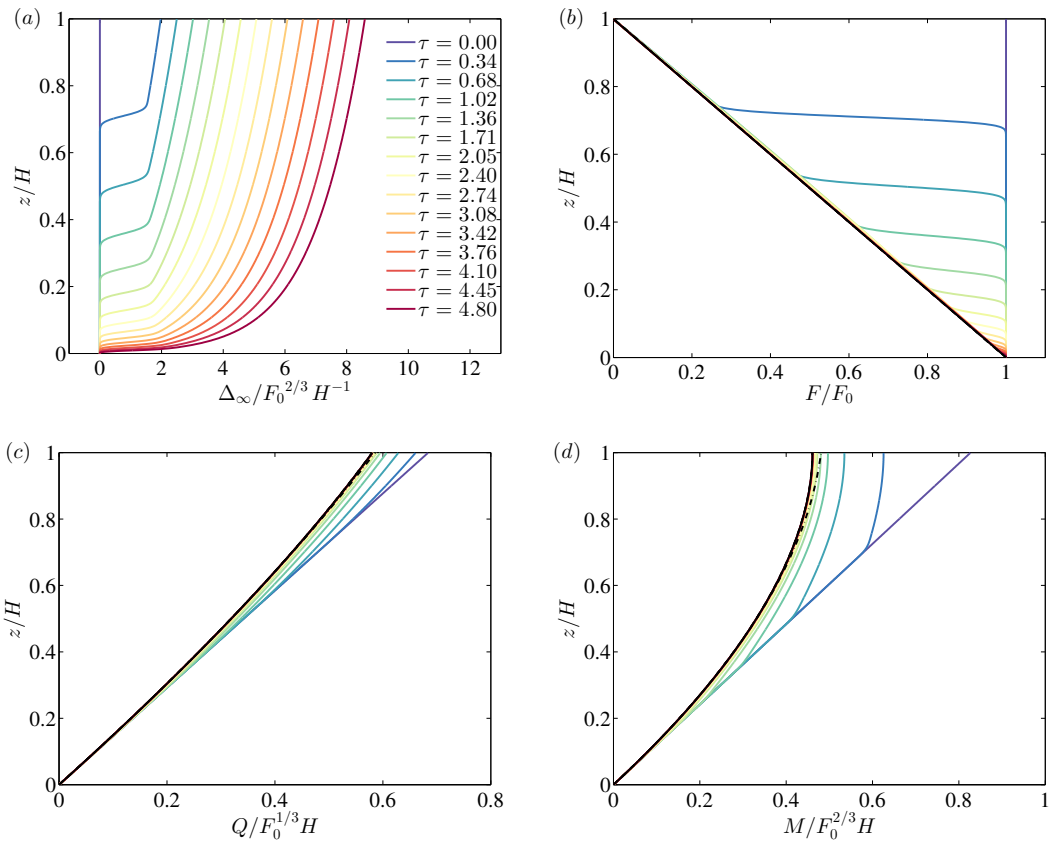

FIGURE B.1: Solutions obtained from the Euler's method and comparison with different numerical method used for Baines and Turner's analytical model, (a) Time-dependent environmental buoyancy profile, (b) plume buoyancy flux, (c) volume flux and (d) momentum flux. The solid and dashed black lines show the asymptotic solutions from ODE45 and power series, respectively.

step will be required to obtain the results to an acceptable degree of accuracy, however; this is not a particularly onerous computational requirement.

B.1 Code for evolution of a wall-attached buoyant plume in confined boxes

The code below written in MATLAB and calculates the evolution of a wall-attached buoyant plume in confined boxes.

```
clear all;
close all;
clc;

% Problem parameters
```

```
alpha = 0.07;
Cf = 0.012;

z_min  = 0;
z_max  =  1;
t_min  =  0.00;
t_max  = 15;

% Simulation parameters

Delta_z          = 0.001;
Delta_t          = 0.0001;
z                = z_min:Delta_z:z_max;
N_z              = length(z)-1;
t                = t_min:Delta_t:t_max;
N_t              = length(t);
R                = 1.0;

% Allocate arrays

Q = 0.0*ones(N_z+1,N_t);  % Volume Flux
M = 0.0*ones(N_z+1,N_t);  % Momentum Flux
F = 0.0*ones(N_z+1,N_t);  % Buoyancy flux
T_P =0.0*ones(N_z+1,N_t); % Plume Temperature
Tinf =0.0*ones(N_z+1,N_t);% Environmental Temperature


Q(1,1:end) = 0.0001;      % initial condition
M(1,1:end) = 0.0001;      % initial condition
F(1,1:end) = 1.0;         % initial condition
T_P(1,1:end) = 1.0;       % initial condition
Tinf(1,1:end) =0.0001;    % initial condition

%%  FDM FW_Explicit Euler Gaussian profile

for n=1:N_t

for i=1:N_z

T_P(i,n) =  (((sqrt(2))*F(i,n))/Q(i,n)) + Tinf(i,n); % Equation (12)

Tinf(i,n+1) = Tinf(i,n) + (Delta_t/Delta_z)*((Q(i,n))/(R))*(Tinf(i+1,n) -Tinf(i,n
    ));  % Equation (16)

F(i+1,n) = F(i,n)- Q(i,n)*((Tinf(i+1,n) -Tinf(i,n)));  % Equation (11)

Q(i+1,n) = Q(i,n) + Delta_z*(sqrt(2)*alpha*M(i,n)/Q(i,n));  % Equation (13)

M(i+1,n) = M(i,n) + Delta_z*(((F(i,n)*Q(i,n))/(M(i,n)))-Cf*((M(i,n)^2)/(Q(i,n)^2)
    ));  % Equation (14)

end

Tinf(N_z,n+1) =  T_P(N_z,n); % Boundary condition at the top wall
```

```
end
```

Bibliography

R. Akhter and N. B. Kaye. Experimental investigation of a line plume in a filling box. *Environmental Fluid Mechanics*, 20(6):1579–1601, 2020.

W. D. Baines and J. S. Turner. Turbulent buoyant convection from a source in a confined region. *J. Fluid Mech.*, 37:51–80, 1969.

S. J. Barnett. *The dynamics of buoyant releases in confined spaces*. PhD thesis, University of Cambridge, 1991.

R. Bonnebaigt, C. Caulfield, and P. Linden. Detrainment of plumes from vertically distributed sources. *Environmental Fluid Mechanics*, 18(1):3–25, 2018.

T. Caudwell, J.-B. Flór, and M.-E. Negretti. Convection at an isothermal wall in an enclosure and establishment of stratification. *J. Fluid Mech.*, 799:448–475, 2016.

B. M. Cetegen, Y. Dong, and M. C. Soteriou. Experiments on stability and oscillatory behavior of planar buoyant plumes. *Phy. Fluids*, 10(7):1658–1665, 1998.

J.-C. Chen. *Studies on gravitational spreading currents*. PhD thesis, California Institute of Technology, 1980.

V. H. Chu. Lagrangian scaling of turbulent jets and plumes with dominant eddies. In *Recent research advances in the fluid mechanics of turbulent jets and plumes*, pages 45–72. Springer, 1994.

B. J. Devenish, G. G. Rooney, and D. J. Thomson. Large-eddy simulation of a buoyant plume in uniform and stably stratified environments. *J. Fluid Mech.*, 652:75–103, 2010.

J. Elicer-Cortés. Measurements of the temperature field in an axisymmetric thermal pure plume. *Exp. Heat Transfer*, 11(3):207–219, 1998.

J. J. Grella and G. M. Faeth. Measurements in a two-dimensional thermal plume along a vertical adiabatic wall. *J. Fluid Mech.*, 71(4):701–710, 1975.

J. Hübner. *Buoyant plumes in a turbulent environment.* PhD thesis, University of Cambridge, 2004.

G. R. Hunt and N. G. Kaye. Virtual origin correction for lazy turbulent plumes. *J. Fluid Mech.*, 435:377–396, 2001.

G. R. Hunt and T. S. Van den Bremer. Classical plume theory: 1937–2010 and beyond. *IMA J. App. Math.*, 76(3):424–448, 2011.

G. R. Hunt, P. Cooper, and P. F. Linden. Thermal stratification produced by plumes and jets in enclosed spaces. *Building and Environ.*, 36:871–882, 2001.

H. J. Hussein, S. P. Capp, and W. K. George. Velocity measurements in a high-reynolds-number, momentum-conserving, axisymmetric, turbulent jet. *Journal of Fluid Mechanics*, 258:31–75, 1994.

Y. Jaluria. Mixed convection in a wall plume. *Computers & Fluids*, 10(2):95–104, 1982.

N. B. Kaye and G. R. Hunt. Overturning in filling box. *J. Fluid Mech.*, 576: 297–323, 2007.

P. D. Killworth and P. C. Manins. A model of confined thermal convection driven by non-uniform heating from below. *Journal of Fluid Mechanics*, 98(3):587–607, 1980.

P. D. Killworth and J. S. Turner. Plumes with time varying buoyancy in a confined region. *Geophys. Astrophys. Fluid Dyn.*, 20:268–291, 1982.

N. E. Kotsovinos. *A study of the entrainment and turbulence in a plane buoyant jet.* PhD thesis, California Institute of Technology, 1975.

N. E. Kotsovinos and E. J. List. Plane turbulent buoyant jets. part 1. integral properties. *Journal of Fluid Mechanics*, 81(1):25–44, 1977.

D. Krug, D. Chung, J. Philip, and I. Marusic. Global and local aspects of entrainment in temporal plumes. *J. Fluid Mech.*, 812:222–250, 2017.

M.-C. Lai and G. Faeth. Turbulence structure of vertical adiabatic wall plumes. 1987.

M.-C. Lai, S.-M. Jeng, and G. Faeth. Structure of turbulent adiabatic wall plumes. *J. Heat transfer*, 1986.

J. H. Lee and V. H. Chu. Turbulent jets. In *Turbulent Jets and Plumes*, pages 21–54. Springer, 2003.

S. L. Lee and H. S. Emmons. A study of natural convection above a line fire. *J. Fluid Mech.*, 11:353–368, 1961.

B. P. Leonard. A stable and accurate convective modelling procedure based on quadratic upstream interpolation. *Comput. Methods Appl. Mech. Eng.*, 19(1): 59–98, 1979.

J. Liburdy and G. Faeth. Heat transfer and mean structure of a turbulent thermal plume along a vertical isothermal wall. *J. Heat Transfer*, 100(2):177–183, 1978.

P. F. Linden, G. F. Lane-Serff, and D. A. Smeed. Emptying filling boxes: the fluid mechanics of natural ventilation. *J. Fluid Mech.*, 212:309–335, 1990.

P. C. Manins. Turbulent buoyant convection from a source in a confined region. *J. Fluid Mech.*, 91:765–781, 1979.

G. Marjanovic, G. Taub, and S. Balachandar. On the evolution of the plume function and entrainment in the near-source region of lazy plumes. *J. Fluid Mech.*, 830:736–759, 2017.

I. Marusic, J. P. Monty, M. Hultmark, and A. J. Smits. On the logarithmic region in wall turbulence. *J. Fluid Mech.*, 716, 2013.

G. Matheou and D. Chung. Direct numerical simulation of stratified turbulence. *Phys. Fluids*, 24(9):091106, 2012.

Y. Morinishi, T. S. Lund, O. V. Vasilyev, and P. Moin. Fully conservative higher order finite difference schemes for incompressible flow. *J. Comp. Phys.*, 143(1): 90–124, 1998.

B. R. Morton. Forced plumes. *J. Fluid Mech.*, 5(1):151–163, 1959.

B. R. Morton and J. Middleton. Scale diagrams for forced plumes. *J. Fluid Mech.*, 58(1):165–176, 1973.

B. R. Morton, G. I. Taylor, and J. S. Turner. Turbulent gravitational convection from maintained and instantaneous sources. *Proc. R. Soc*, A 234:1–23, 1956.

C. S. Ng, A. Ooi, D. Lohse, and D. Chung. Vertical natural convection: application of the unifying theory of thermal convection. *J. Fluid Mech.*, 764:349–361, 2015.

S. Paillat and E. Kaminski. Entrainment in plane turbulent plumes. *J. Fluid Mech.*, 755:R2, 2014a.

S. Paillat and E. Kaminski. Entrainment in plane turbulent pure plumes. *Journal of Fluid Mechanics*, 755, 2014b.

N. R. Panchapakesan and J. L. Lumley. Turbulence measurements in axisymmetric jets of air and helium. part 1. air jet. *Journal of Fluid Mechanics*, 246:197–223, 1993.

P. N. Papanicolaou and E. J. List. Investigations of round vertical turbulent buoyant jets. *Journal of Fluid Mechanics*, 195:341–391, 1988.

D. Parker, H. C. Burridge, J. Partridge, and P. Linden. A comparison of entrainment in turbulent line plumes adjacent to and distant from a vertical wall. *Journal of Fluid Mechanics*, 882, 2020.

M. V. Pham, F. Plourde, and K. Doan. Direct and large-eddy simulations of a pure thermal plume. *Phy. Fluids*, 19(12):125103, 2007.

F. Plourde, M. V. Pham, S. D. Kim, and S. Balachandar. Direct numerical simulations of a rapidly expanding thermal plume: structure and entrainment interaction. *J. Fluid Mech.*, 604:99–123, 2008.

S. B. Pope. Turbulent flows, 2001.

B. Ramaprian and M. Chandrasekhara. Measurements in vertical plane turbulent plumes. *J. Fluids Eng, Trans. ASME*, (111):69–77, 1989.

H. Rouse, C. S. Yih, and H. W. Humphreys. Gravitational convection from a boundary source. *Tellus*, 4(3):201–210, 1952.

B. Sanderse, R. Verstappen, and B. Koren. Boundary treatment for fourth-order staggered mesh discretizations of the incompressible navier–stokes equations. *Journal of Computational Physics*, 257:1472–1505, 2014.

R. Sangras, Z. Dai, and G. Faeth. Velocity statistics of plane self-preserving buoyant turbulent adiabatic wall plumes. *J. Heat Transfer*, 122(4):693–700, 2000.

W. Schmidt. Turbulente ausbreitung eines stromes erhitzter luft. *Z. angew. Math. Mech.*, 21(5):265–278, 1941.

A. Shabbir and W. K. George. Experiments on a round turbulent buoyant plume. *Journal of Fluid Mechanics*, 275:1–32, 1994.

P. R. Spalart. On the cross-flow instability near a rotating disk. *Proc. Boundary Layer Transition & Control*, pages 22.1–13, 1991.

R. J. A. M. Stevens, R. Verzicco, and D. Lohse. Radial boundary layer structure and Nusselt number in Rayleigh–Bénard convection. *J. Fluid Mech.*, 643:495–507, 2010.

G. N. Taub. *A numerical and experimental study of turbulent single and multiphase forced plumes and jets at moderate Reynolds numbers*. University of Florida, 2013.

H. Tennekes and J. L. Lumley. *A first course in turbulence*. MIT press, 1972.

M. van Reeuwijk and J. Craske. Energy-consistent entrainment relations for jets and plumes. *J. Fluid Mech.*, 782:333–355, 2015.

R. Verstappen and A. Veldman. Symmetry-preserving discretization of turbulent flow. *Journal of Computational Physics*, 187(1):343–368, 2003.

H. Wang and A. W.-k. Law. Second-order integral model for a round turbulent buoyant jet. *Journal of Fluid Mechanics*, 459:397, 2002.

M. Worster and H. Huppert. Time-dependent density profiles in a filling box. *J. Fluid Mech.*, 132:457–466, 1983.

E. E. Zukoski. Development of a stratified ceiling layer in the early stages of a closed-room fire. *Fire Matter.*, 2(2):54–62, 1978.

E. E. Zukoski. Fluid dynamic aspects of room fires. In *Proceedings of the First International Symposium on Fire Safety Science*, 1986.